National Library
of Canada

Bibliothèque nationale
du Canada

Canadian Theses Service

Service des thèses canadiennes

Ottawa, Canada
K1A 0N4

NOTICE

The quality of this microform is heavily dependent upon the quality of the original thesis submitted for microfilming. Every effort has been made to ensure the highest quality of reproduction possible.

If pages are missing, contact the university which granted the degree.

Some pages may have indistinct print especially if the original pages were typed with a poor typewriter ribbon or if the university sent us an inferior photocopy.

Reproduction in full or in part of this microform is governed by the Canadian Copyright Act, R.S.C. 1970, c. C-30, and subsequent amendments.

AVIS

La qualité de cette microforme dépend grandement de la qualité de la thèse soumise au microfilmage. Nous avons tout fait pour assurer une qualité supérieure de reproduction.

S'il manque des pages, veuillez communiquer avec l'université qui a conféré le grade.

La qualité d'impression de certaines pages peut laisser à désirer, surtout si les pages originales ont été dactylographiées à l'aide d'un ruban usé ou si l'université nous a fait parvenir une photocopie de qualité inférieure.

La reproduction, même partielle, de cette microforme est soumise à la Loi canadienne sur le droit d'auteur, SRC 1970, c. C-30, et ses amendements subséquents.

NL-339 (r. 88/04) c

Canadä

A ^{13}C-NMR STUDY OF THF DECOMPOSITION ON Li_xMoS_2

by

Marc Walter Juzkow
B.Sc. (Chemistry), Simon Fraser University, 1985

A THESIS SUBMITTED IN PARTIAL FULFILLMENT OF
THE REQUIREMENTS FOR THE DEGREE OF
MASTER OF SCIENCE (CHEMISTRY)
in the Department
of
Chemistry

Simon Fraser University
April 1989

National Library of Canada
Bibliothèque nationale du Canada

Canadian Theses Service
Service des thèses canadiennes

Ottawa, Canada
K1A 0N4

ISBN 0-315-59354-7

I hereby grant Marc Juzkow permission to reproduce Figure 2 from my Ph.D. thesis (1979) for his Master's thesis (1989) and for microfilming by the National Library of Canada.

Dr. W.R. McKinnon

28 Apr 89

Date

I hereby grant Marc Juzkow permission to reproduce Figure 4 from my Master's thesis (1988) for his Master's thesis (1989) and for microfilming by the National Library of Canada.

Rosamaria Fong

Date

I hereby grant Marc Juzkow permission to reproduce Figure 1 from my paper in the Canadian Journal of Physics, Vol. 60, p.307 (1982) for his Master's thesis (1989) and for microfilming by the National Library of Canada.

Dr. Jeff Dahn

Apr 18/89

Date

APPROVAL

NAME:	Marc Walter Juzkow
DEGREE:	Master of Science (Chemistry)
TITLE OF THESIS:	A ^{13}C-NMR Study of THF Decomposition on Li_xMoS_2

EXAMINING COMMITTEE:

Chairman: Dr. P. Percival

Dr. I.D. Gay
Professor
Senior Supervisor

Dr. C.H.W. Jones
Professor/Dean of Science

Dr. E.J. Wells
Associate Professor

Dr. D.P. Wilkinson
Moli Energy Ltd.

Dr. R.F. Frindt
Internal Examiner
Professor, Physics, SFU

DATE APPROVED: April 18, 1989

PARTIAL COPYRIGHT LICENSE

Title of Thesis/Project/Extended Essay

A ^{13}C-NMR STUDY OF THF

DECOMPOSITION ON Li_xMoS_2

Author:

(signature)

MARC JUZKOW

(name)

April 18/89.

(date)

ABSTRACT

A ^{13}C-NMR Study of the Decomposition of Tetrahydrofuran on Li_xMoS_2

Rechargeable lithium battery systems using nonaqueous electrolytes are prone to solvent decomposition resulting in decreased capacity and cycle life. Magic Angle Spinning Solid-State ^{13}C-NMR was used to study the decomposition of tetrahydrofuran, a common battery solvent, on the surface of molybdenum disulfide cathode material before and after lithiation. High surface area Li_xMoS_2 samples, where $x = 0,1$ or 3, were prepared to maximize THF adsorption for this NMR study. The materials were characterized by X-ray powder diffractometry, thermal gravimetric analysis, density, Dionex ion chromatography and B.E.T. surface area measurements. The syntheses of high surface area MoS_2 by thermal decompositions of $(NH_4)_2MoS_4$ and MoS_3 were studied using residual gas analysis. Electrochemical cells were prepared to compare the performance of high and low surface area MoS_2 as a lithium battery cathode material. Various FT-NMR experiments were used to identify the THF breakdown products due to thermal surface reactions.

No decomposition products were found for any sample at room temperature, therefore the variation of x in Li_xMoS_2 samples could not be used to determine a solvent reduction potential for THF. At elevated temperatures, MoS_2 was found to be more reactive with regard to decomposition of THF than Li_1MoS_2 or Li_3MoS_2, due possibly to structural differences induced by lithiation. A trend of greater catalytic activity with increasing lithiation values was not observed. The nature of the decomposition products however, depended on x in Li_xMoS_2.

TO MY WIFE, CHICKIE

ACKNOWLEDGEMENTS

It is a great pleasure to thank my supervisor, Dr. Ian Gay, for his advice and encouragement throughout this project. His physical and experimental insight proved indispensible in this work. I also wish to express my appreciation to Dr. David Wilkinson for his discussions and comments during the completion of this work.

Special thanks to Dr. Jeff Dahn for his encouragement, positive discussions and thesis review, and Dr. Bryan Taylor for reviewing my thesis. I have also benefitted from discussions with Dr. Ulrich von Sacken, Dr. Bob Frindt and members of his group in the SFU Physics department.

I gratefully acknowledge financial support from Moli Energy Ltd.

I would like to thank my wife for her assistance in the preparation of this thesis and for her support during this exciting but hectic first 18 months of marriage.

Finally, I would like to thank my father for being a source of inspiration and support throughout my academic career.

TABLE OF CONTENTS

LIST OF TABLES

LIST OF FIGURES

LIST OF FIGURES (cont'd)

LIST OF FIGURES (cont'd)

1.0 INTRODUCTION

1.1 Objectives of this Thesis

The aim of this work is to evaluate a new technique to study *in-situ* lithium battery solvent cathodic decomposition. The technique utilizes Magic Angle Spinning Solid-State ^{13}C-NMR to study catalytic solvent decomposition reactions on the surface of cathode material. The lithium battery system used in this study has an electrolyte of 1M $LiAsF_6$ in tetrahydrofuran (THF) and molybdenum disulfide (MoS_2) as the cathode.

The Introduction has been divided into four sections. A review of lithium electrochemical cells concentrating on Li/MoS_2 is given in the second section. Intercalation is included and the importance of the solvent is discussed. Previous work, structure, other uses of and catalytic properties of MoS_2 are discussed in the third section. The fourth section concentrates on the NMR technique and its application in this study in terms of the solvent and cathode components. The use of high surface area Li_xMoS_2 in place of standard low surface area material is explained. Also discussed is the novel study of the catalytic properties of Li_xMoS_2 on THF decomposition as a function of x or potential with respect to lithium using this *in-situ* ^{13}C-NMR technique.

The Experimental Procedures section is divided into seven parts. Section a) outlines the syntheses involved in preparing high surface area Li_xMoS_2. Section b) describes the Magic Angle Spinning (MAS) Solid-State ^{13}C-NMR apparatus, MAS Solid-State NMR theory is briefly discussed and the preparation of samples and pulse NMR experiments used are explained. Electrochemical cell components and assembly, gas evolution cell preparation and apparatus and electrochemical measurements are discussed in section c). In the latter sections d) through g), X-ray powder diffraction technique and procedure, Brunauer-Emmett-Teller surface area determination, thermal gravimetric analysis and residual gas analysis are discussed, respectively. Techniques c) through g) were utilized to characterize the high surface area MoS_2 synthesized for this study and for comparison to standard low surface area MoS_2.

The results are presented in the Results and Discussion section. Li_xMoS_2 syntheses are discussed and characterized using residual gas analysis, X-ray powder diffraction and thermal gravimetric analysis. The performance of high and low surface area MoS_2 cathode materials in lithium electrochemical cells is discussed. The results from ^{13}C-NMR studies of thermal decomposition series of THF adsorbed materials are discussed as well as a series of miscellaneous experiments.

Finally, in the last section, the thesis is summarized and conclusions are presented.

1.2 The Electrochemical Cell

Rechargeable lithium/molybdenum disulfide batteries are based on intercalation. The three active components of a Li/MoS_2 electrochemical cell are the lithium anode, a liquid electrolyte containing a dissolved lithium salt and the molybdenum disulfide cathode. The former two components will be discussed briefly in this section while the latter, MoS_2 will be discussed separately and in greater detail in the following section due to its importance in this study. The process of intercalation will also be discussed as the interactions of the components are put into perspective.

Intercalation is the reversible insertion of guest atoms into host materials with minimal physical alteration of the host structure. The two major classes of host materials have either a layered crystal structure or a non-layered or framework structure. The MoS_2 cathode is an example of a layered intercalation host.

Lithium, the guest atom, has a very low electronegativity for a metal, allowing cells with the highest possible voltages to be constructed. This combined with its low density make lithium an ideal choice for a battery anode material with high specific energy. Due to its small atomic size, lithium is very mobile as the intercalated species thus permitting high rate electrochemical cells.

Separating the lithium metal anode and the MoS_2 intercalation compound is a liquid electrolyte as shown in Fig. 1. This liquid electrolyte is comprised of a lithium salt dissolved in a non-aqueous solvent.

Intercalation or cell discharge takes place when the two electrodes are connected by an external electrical load. Lithium atoms on the surface of the anode dissociate into ions and electrons; the ions migrate through the liquid electrolyte in the direction of the cathode as the electrons travel through the external circuit, also towards the cathode. Recombination of the ions and electrons occurs on the surface of the MoS_2 cathode particles and the reformed lithium atoms intercalate between the MoS_2 crystal layers.

Intercalation is reversed during the process of recharge. Intercalated lithium atoms upon reaching the surface of the MoS_2 particles dissociate into ions and electrons travelling via the electrolyte and external circuit respectively. At the surface of the anode they recombine and are electroplated as lithium metal.

Figure 1 Schematic diagram of a Li/MoS_2 intercalation cell.

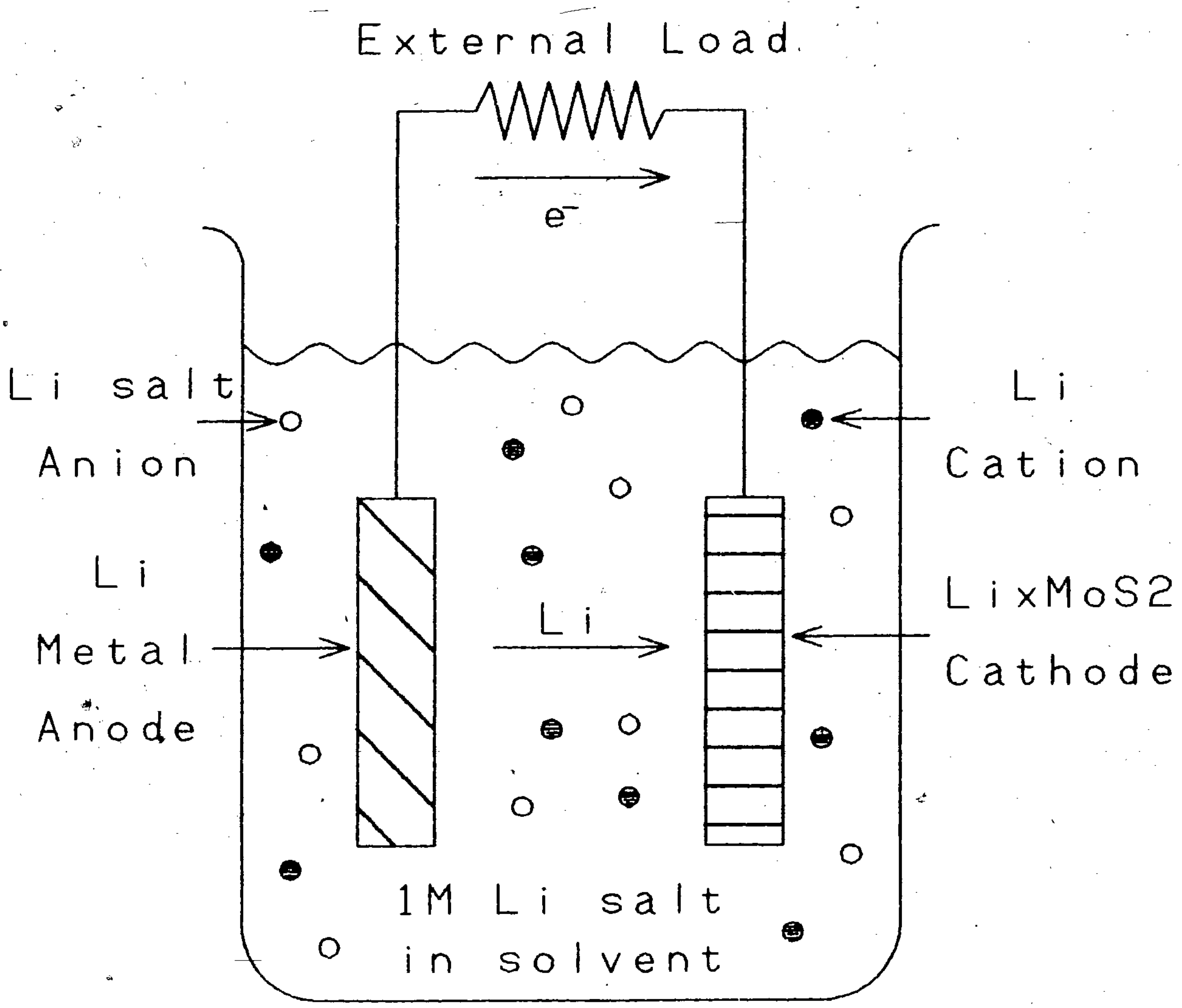
External Load
e⁻
Li salt
Anion
Li
Metal
Anode
Li
Li
Cation
LixMoS2
Cathode
1M Li salt
in solvent

Electrical work is accomplished by electrons travelling in the external circuit during intercalation. This is due to the difference in free energy of the lithium atoms in lithium metal and those intercalated in the MoS_2 host. The latter is preferred by the lithium atoms therefore energy is released during intercalation. The free energy difference also reflects the potential of this electrochemical cell; for Li_xMoS_2 cathode, smaller x values correspond to higher voltages and vice versa.

The electrolyte is an important component of the electrochemical cell. Desired properties include chemical and electrochemical stability over wide temperature and potential ranges and high ionic conductance. Solvent properties affecting solution conductivity are dielectric constant and viscosity.

Ester-based solvent systems utilizing propylene carbonate are widely used and have excellent performance but suffer from poor rate capabilites at low temperatures. One solution to this problem is a mixed solvent incorporating a low viscosity and low melting point solvent to raise the low temperature electrical conductivity of the electrolyte. Tetrahydrofuran is a good candidate as it meets the low temperature requirements but it has been found to be prone to decomposition in the Li/MoS_2 system.(1)

1.3 Molybdenum Disulfide

Molybdenum disulfide is mined as an ore, molybdenite, which occurs as fine crystals imbedded in quartz deposits. A flotation process is used for extraction of MoS_2 from the ore, which is possible due to the natural hydrophobic surface of the mined molybdenite.

Molybdenum disulfide was developed as a lithium battery cathode material by Haering et al.(2) Factors which make MoS_2 ideal include its abundance in nature, low cost and low toxicity.

A great deal of work has been done on MoS_2 including publications by McKinnon(3), Py and Haering(4), Brandt and Stiles(5), Mulhern(6), Johnson and Laman(7) and Chiannelli *et al.*(8).

In its natural state MoS_2 is a two dimensional layered structure. Molybdenum disulfide has the trigonal prismatic structure, space group $P6_3/mmc$ with stacking S-Mo-S S-Mo-S. There are 2 S-Mo-S sandwiches in each unit cell of MoS_2(2H crystallographic polytype). Weak sulfur-sulfur van der Waals forces hold the layers together while strong covalent bonds exist within the layers. The molybdenum atom can also exist in an octahedral coordination or 1T polytype.(4) Molybdenum disulfide is a p-type semiconductor. Fig. 2 illustrates the various structures of MoS_2.

Figure 2 Structural representations of MoS_2.*

a) General form of an MX_2 layer compound sandwich. For MoS_2, M=Mo and X=S.

b) Co-ordination units.

c) MoS_2 (2H polytype).

* Drawings taken from W.R. McKinnon. Ph.D. thesis. University of British Columbia, Vancouver, B.C. 1980.

(a)

General form

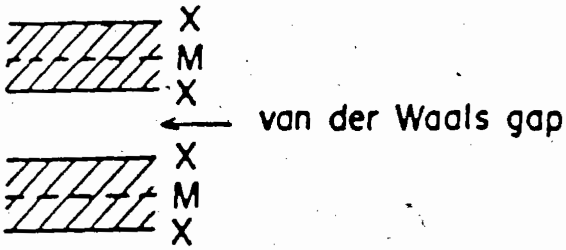

(b) Coordination units for MX_2 layer structures

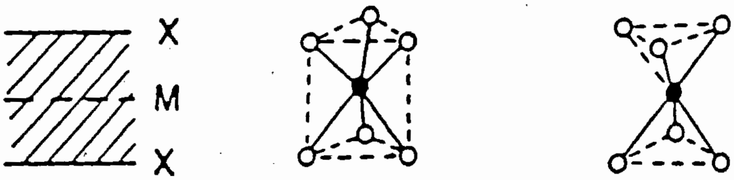

AbA trigonal prism

AbC octahedron

(c)

2H-MoS_2

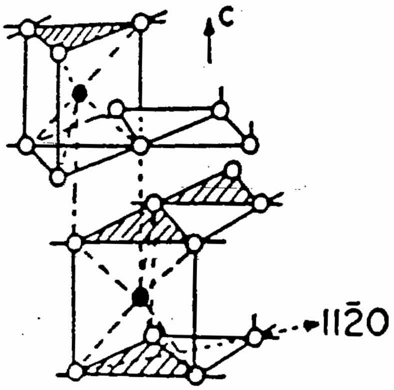

AbA BaB

In addition to use in lithium batteries, MoS_2 is used as a solid lubricant. Attached to a metal substrate, MoS_2 reduces the friction between moving surfaces. MoS_2 is far superior to graphite in its performance at extreme low or high pressures and in its lubricating properties in varying environmental conditions. MoS_2 is also used as an additive in plastics to reduce wear rate by decreasing friction and to improve the mechanical and physical properties of thermoplastics.

Molybdenum disulfide has important catalytic properties and acts primarily as a desulphurization catalyst. Catalytic MoS_2 may be in the form of poorly crystalline material(9), a cobalt promoted graphitized system(10) or inclusion compounds which are formed from exfoliated MoS_2 (single layer) and divalent cations(11). Industrial uses includes oil refining and gasification of coal.(12) The activity of MoS_2 as a catalyst is dependent on its total surface area, distribution of surface area between the basal and edge planes, and the pretreatment of the surface with various gases.

1.4 Magic Angle Spinning Solid-State ^{13}C-NMR

To obtain a better understanding of the chemistry involved in cathodic decomposition, Magic Angle Spinning, MAS-Solid-State ^{13}C-NMR was used to examine the reactivity of tetrahydrofuran adsorbed onto the surface of Li_xMoS_2 where $0 \leq x \leq 3$.

Tetrahydrofuran (THF) was an ideal molecule for use in a ^{13}C-NMR study as it contains two pairs of magnetically equivalent carbon atoms which result in stronger ^{13}C signal-to-noise ratios. Its high vapor pressure allows gas phase transfer from the liquid to yield single adsorption layers on the surface of the Li_xMoS_2 powders.

Molybdenum disulfide however was not as ideal for this study as its surface area was typically <10 m^2/g, which is too low for reasonable amounts of adsorption to occur. High surface area MoS_2 was prepared to maximize THF adsorption for enhanced ^{13}C signal-to-noise ratios. This high surface area MoS_2 was characterized physically and electrochemically to compare it with typical low surface area MoS_2.

By varying the proportion of lithium in the host material its potential with respect to lithium could be changed. In this manner it was possible to study the catalytic properties of Li_xMoS_2 on THF decomposition as a function of x or potential with respect to lithium.

Previous experiments analyzing the decomposition products of chemisorbed solvents and gases on various catalytic surface by high resolution solid-state ^{13}C-NMR have been done by Gay *et al.*(13-16) This is the first study in which this technique has been used for analyzing lithium battery solvent decomposition *in situ* on the surface of a cathode material.

2.0 EXPERIMENTAL PROCEDURES

2.1 Material Synthesis and Preparation

2.1.1 $(NH_4)_2MoS_4$

Ammonium tetrathiomolybdate (ATTM), $(NH_4)_2MoS_4$ was used to obtain high surface area Li_xMoS_2 samples. ATTM was prepared by bubbling hydrogen sulfide(Matheson,Tech. Grade) through an aqueous solution of ammonium molybdate, $(NH_4)_2MoO_4$(Equity Mine) and ammonium hydroxide(Fisher,Reagent ACS),using a variation of a method described by Brauer(17).

$$(NH_4)_2MoO_4 + 4H_2S \xrightarrow{NH_4OH} (NH_4)_2MoS_4 + 4H_2O \qquad \text{Eq.1}$$

The red $(NH_4)_2MoS_4$ crystals were filtered, washed with methanol(Fisher,99.8%), dried under vacuum and kept under a helium atmosphere prior to use. X-ray powder diffractometry and thermal gravimetric analysis were used to test the purity of $(NH_4)_2MoS_4$.

2.1.2 MoS_3

Amorphous molybdenum trisulfide, MoS_3, was prepared by thermal decomposition of $(NH_4)_2MoS_4$ and by chemical decomposition at ambient temperature from an aqueous solution of the same salt.

Thermal decompositions of 1-5g $(NH_4)_2MoS_4$ were done at 300-450°C under a flowing argon(Liquid Carbonic,99.998%) atmosphere for one hour periods. Large grey particles were formed using this method.

Chemical decompositions of $(NH_4)_2MoS_4$ were accomplished using a procedure similar to Auburn *et al.*(18) Five grams of $(NH_4)_2MoS_4$ was dissolved in a 5% NH_4OH/aqueous solution and the solution saturated with bubbling H_2S for a minimum of one hour. A 5% formic acid(BDH,88%) aqueous solution was slowly added to the solution at which time MoS_3 precipitated out of solution.

$$(NH_4)_2MoS_4 + 2HCOOH \xrightarrow[H_2S]{NH_4OH} MoS_3 + 2NH_4^+ + 2HCOO^- + H_2S \qquad \text{Eq.2}$$

The precipitate was allowed to settle overnight, the clear solution was decanted and the remainder filtered through a fine glass frit filter. The black precipitate was washed with 2X100ml methanol. Following washing, the precipitate was dried under vacuum using a freeze dryer for a minimum of 24 hours. Small black particles were obtained after drying and were ground to a fine powder with a mortar and pestle.

2.1.3 MoS_2

Molybdenum disulfide was prepared from both types of MoS_3 using thermal decomposition under various reducing atmospheres. Ammonia gas(99.99%) was used as a reducing atmosphere but the best results, i.e.

S/Mo ratio close or equal to 2.00, were obtained with either a 5, 15 or 100% hydrogen/inert gas atmosphere. All of these gases were from Liquid Carbonic.

Temperatures and times used for thermal decomposition of MoS_3 to MoS_2 were found to be critical as high temperatures were necessary for complete decomposition but resulted in more crystalline, lower surface area MoS_2. The resulting powders were characterized using X-ray powder diffraction, a thermal gravimetric analysis method to determine the S/Mo ratio and B.E.T. surface area determination. Overall, using MoS_3 from the chemical decomposition of $(NH_4)_2MoS_4$, decomposing at 250°C for two hours in a flowing 15% H_2/He atmosphere resulted in the highest surface areas and densities with low S/Mo ratios and poor crystallinity.

2.1.4 Li_xMoS_2

Lithiated MoS_2 samples were prepared using chemical reactions which mimic the discharge or intercalation of cathode material in lithium batteries. The two techniques used were described in principle by Murphy and Christian.(19)

In the first method, small amounts of MoS_2 (typically <1g) were stirred overnight in stoichiometric amounts of 0.25 or 0.5M n-butyllithium in n-hexane(Alfa).

$$MoS_2 + xCH_3CH_2CH_2CH_2Li \xrightarrow{\text{n-hexane}} Li_xMoS_2 + x/2[CH_3(CH_2)_6CH_3] \qquad \text{Eq.3}$$

The solutions were filtered, rinsed with copious volumes of n-hexane (Burdick and Jackson,UV Grade) and dried under vacuum. The entire procedure was carried out in a helium filled glove box.

Alternatively, lithium foil(Foote) was dissolved in liquid ammonia to which MoS_2 was added forming $Li_xMoS_2(NH_3)_y$.

$$MoS_2 + xLi + yNH_3 \xrightarrow{NH_3} Li_xMoS_2(NH_3)_y \qquad \text{Eq.4}$$

The apparatus used is shown in Fig.3. After purging the closed system with argon, gaseous ammonia was passed through and allowed to condense using an acetone-dry ice low temperature bath and condensing finger. Typically 30-50mls of liquid ammonia were used to dissolve the stoichiometric amount of lithium foil, forming a deep blue solution. Quantities of MoS_2 ranging from 0.8 to 3.9g were then added with stirring to the Li/NH_3 solution. Within minutes the liquid solution would become colorless denoting complete lithium intercalation into the MoS_2 powder.

To recover the lithiated powder, the solution was simply brought to room temperature and the remaining ammonia allowed to evaporate

Figure 3 Liquid ammonia solvent apparatus for lithium intercalation of molybdenum disulfide.

a) Apparatus for condensing gaseous ammonia including reaction flask for intercalation of dissolved lithium into molybdenum disulfide.

b) Apparatus for evaporating ammonia after completion of intercalation.

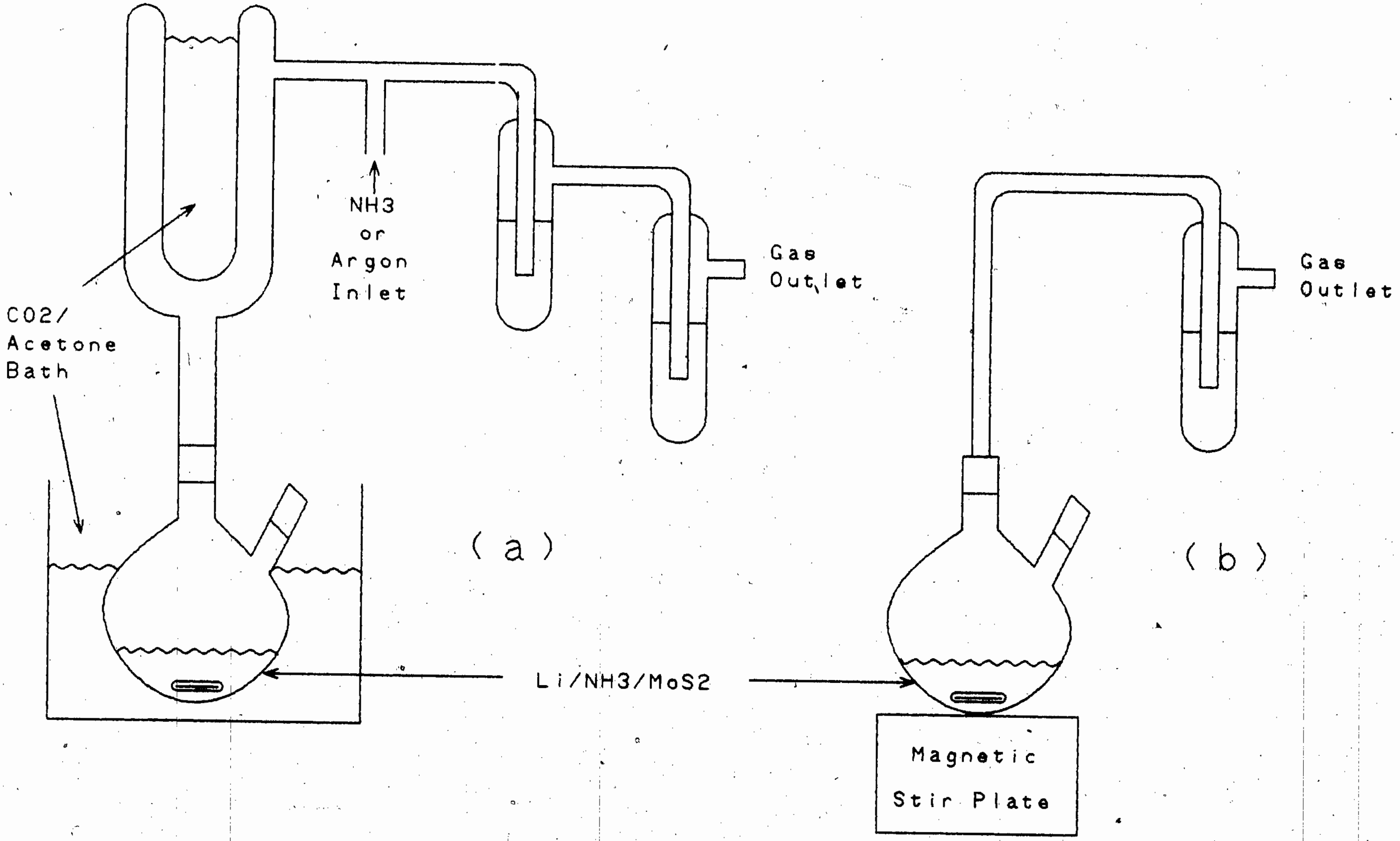
CO2/
Acetone
Bath
NH3
or
Argon
Inlet
Gas
Outlet
Gas
Outlet
(a)
(b)
Li/NH3/MoS2
Magnetic
Stir Plate

through an oil bubbler. Upon completion the sample flask was placed inside an antechamber under vacuum overnight for transfer into a helium filled glove box. These final steps were carried out with minimal exposure to the atmosphere.

Due to co-intercalation of the NH_3 solvent, removal was carried out under vacuum at 200-250°C for a minimum 12 hour period. Ammonia (as ammonium ion) and lithium ion samples were prepared by adding ≈0.2g of $Li_xMoS_2(NH_3)_y$ to 500ml or 1000ml of 0.005M HCl(Merck,Suprapur) in deionized H_2O (Millipore,18MΩ) and the concentrations were determined using a Dionex 2010i Ion Chromatograph. The acidic solution (pH=4) was used to convert NH_3 to NH_4^+ and to ensure the complete dissolution of Li^+ ions.

Special air-sensitive handling techniques were used to ensure these lithiated samples were not exposed to the atmosphere during characterization. Prior to B.E.T. surface area determination the samples were sealed inside Pyrex® sample holders using silicone o-ring fittings and a teflon stopcock also fitted with silicone o-rings. Under the helium atmosphere from the glove box, the sample could be transported, then connected to the B.E.T. apparatus without exposure to the atmosphere. X-ray powder diffraction patterns were obtained using a sealed X-ray sample holder assembled inside the glovebox. This X-ray sample case is described in greater detail in a later section.

2.1.5 Tetrahydrofuran

Tetrahydrofuran(Fisher,Reagent ACS) was predried over 4A molecular sieve(Fisher,Grade 514), repurified over a lithium benzophenone ketyl solution in a nitrogen atmosphere and stored in a helium atmosphere glovebox. Purity was determined using gas chromatography/ mass spectrometry and Karl Fischer moisture analysis.

2.1.6 Summary of Material Synthesis

Ultimately large surface area/volume samples were required for this ^{13}C-NMR study. High density and surface area were therefore both important.

To obtain MoS_2 with the highest surface area/volume, freshly synthesized $(NH_4)_2MoS_4$ had to be used. Ammonium tetrathiomolybdate purchased from Aldrich resulted in low density decomposition products. Chemical decomposition of $(NH_4)_2MoS_4$ gave the highest surface area values for MoS_3 and reasonable densities. Thermal decomposition of MoS_3 to MoS_2 at relatively low temperatures resulted in increased density but lowered surface area. The surface area obtained was however higher than those obtained by other preparation schemes.

Chemical lithiation of MoS_2 using the Li/NH_3 technique yield high surface area powders. Although the initial densities of $Li_xMoS_2(NH_3)_y$ were low, they increased upon removal of NH_3.

2.2 Magic Angle Spinning Solid-State ^{13}C-NMR

2.2.1 Apparatus

The apparatus used in this study is a modified commercial high-resolution NMR spectrometer enabling ^{1}H-^{13}C solid-state cross-polarization experiments to be performed. The spectrometer consists of various components including a Varian HA-60 magnet, a modified Bruker WP-60 console and a Nicolet 1080 computer. A TT-14 spectrometer from Transform Technology Inc. interfaces all of the above components.

In a simplistic NMR spectrometer as shown in Fig.4, a Programmed Test Sources(PTS) synthesizer generates a 10MHz signal. The lock, observed and decoupler frequencies all originate from this central oscillator. The lock frequency, 9.2MHz was used without amplification. An external deuterium lock inside the probe consisting of a D_2O sample doped with $CuSO_4$ was used. A General Radio synthesizer coupled with a tranceiver generates observed signals from 5 to 150MHz; 15.0923MHz was used for ^{13}C in this study. A broadband decoupler capable of producing frequencies from 5 to 150MHz was used. When using this decoupler for ^{1}H it was set at 60.016MHz. Two series of amplifiers were used to increase the power of the observed and decoupler frequencies from 10mW to 100W.

A magic angle spinning assembly for vacuum-sealed samples constructed by Gay(20) was used. Samples were spun up to 3±0.1kHz reliably for long periods of time.

Figure 4 Block diagram of the modified NMR spectrometer.

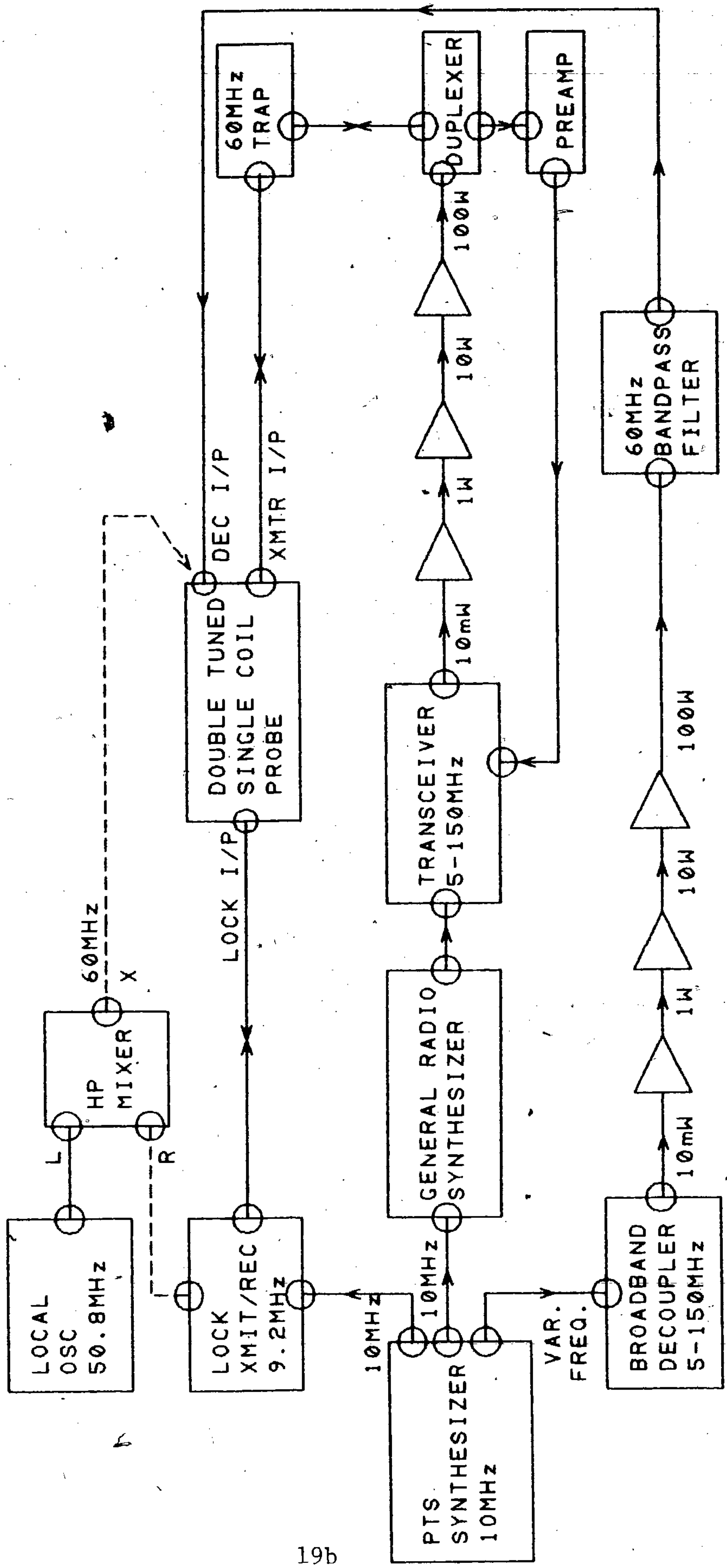
60MHz TRAP
DUPLEXER
PREAMP
100W
10W
1W
10mW
DEC I/P
XMTR I/P
DOUBLE TUNED SINGLE COIL PROBE
LOCK I/P
60MHz BANDPASS FILTER
100W
10W
1W
10mW
TRANSCEIVER 5-150MHz
60MHz
X
HP MIXER
L
R
GENERAL RADIO SYNTHESIZER
LOCAL OSC 50.8MHz
LOCK XMIT/REC 9.2MHz
10MHz
10MHz
PTS SYNTHESIZER 10MHz
VAR. FREQ.
BROADBAND DECOUPLER 5-150MHz

2.2.2 Solid-State NMR

It is not within the scope of this dissertation to explain the phenomena of magnetic resonance. Its theory is well known and can be found in books by Abragam(21) and Slichter(22) among many others. Application of NMR to solid-state studies will be reviewed and compared to liquid or solution NMR, the difficulties and limitations will be outlined and solutions will be discussed.

Five interactions involving a nucleus with a magnetic moment which may occur are:

1. The Zeeman interaction of the nucleus with the magnetic field (10^6-10^9Hz).
2. Dipole-dipole interactions between nuclei (0-10^5Hz).
3. Chemical shift interaction due to shielding effect on the nucleus by surrounding electrons (0-10^5Hz).
4. Scalar or spin-spin coupling to other nuclei (0-10^4Hz).
5. Quadrupolar interaction present only for nuclei with spin > ½ (0-10^9Hz).

The relative importance of each interaction is determined by the nuclei present.

In solid-state NMR, as opposed to solution NMR it is the dipole-dipole interactions which are critical. In the latter, the fast (on the NMR time scale) nearly isotropic (ie. translational and rotational) motion of the molecules yields an average value of zero for dipolar interactions. This is not the case for solids.

If the dipolar term of the general Hamiltonian incorporating all interactions is removed by averaging to zero, the observation of other important interactions, namely chemical shift and spin-spin coupling is made possible. The dipolar term is made up of the product of a spatial and a spin term. An important factor in the spatial term is $\frac{1}{2}(3\cos^2\theta - 1)$ which may be reduced to zero using the correct value of $\theta = 54.73°$. As a result, if a solid sample is spun at several kHz the dipolar, chemical shift and spin-spin coupling interactions are each reduced to an isotropic average, which in the dipolar case is equal to zero.

The purpose of spinning is to remove chemical shift anisotropy. Assuming the maximum anisotropy of 200ppm for aromatic carbons, a spinning rate of 3kHz is necessary to completely remove the shift anisotropy at a proton resonance frequency of 60MHz. Increasing the strength of the magnet requires greater spinning speeds and therefore is undesirable.

Broadening of lines due to heteronuclear (C-H) dipolar interactions is another problem in ^{13}C-NMR of solids because it is impossible to spin the samples fast enough. Decoupling the protons with a high power amplifier eliminates these effects from the spectra.

2.2.3 Preparation of NMR Samples

Table I lists the NMR samples prepared for this study including static and magic angle spinning samples. All samples were prepared on a glass vacuum rack as shown in Fig.5. This dual purpose rack was also used for B.E.T. surface area measurements.

Before and after each quantitative pretreatment with H_2 (Linde, Extra Dry) at 200-300°C and O_2 (Linde, Extra Dry) at room temperature, the NMR samples were evacuated to $<1X10^{-5}$ torr. Tetrahydrofuran or other solvents were then quantitatively adsorbed onto the surface of the powder sample used. The amounts were measured by conventional gas-volumetric techniques.

Static NMR samples were prepared in Pyrex® tubes of 12mm O.D. which sat in a NMR probe coil measuring 20mm in length. These samples were sealed under vacuum prior to use.

Magic angle spinning samples were prepared in Wilmad grade 507-PP NMR tubes of 5mm O.D. These tubes were carefully sealed under pressures of <40 torr to allow spinning in the MAS probe up to 2-3kHz. The coil in the probe is approx. 17mm in length and the NMR tubes are generally 45-60mm in length.

Table I - ^{13}C-NMR Samples

Sample No.	Powder	Static/ MAS	H_2 Treatment	O_2 Chemisorption	Solvent Adsorption
1	MoS_2	Static	NO	NO	THF
2	MoS_2	Static	YES	NO	NONE
3	MoS_2	Static	YES	YES	THF
4	MoS_2	Static	YES	NO	THF
5	MoS_2	MAS	YES	NO	THF
6	MoS_2	MAS	YES	YES	THF
7	MoS_2	MAS	YES	NO	THF (½ dose)
9	Li_1MoS_2	MAS	NO	NO	THF
10	MoS_2	MAS	YES	YES	THF
13	Li_1MoS_2	MAS	NO	NO	THF
15	Li_1MoS_2	MAS	NO	NO	THF
16	MoS_2	MAS	YES	YES	THF
17	MoS_2	MAS	YES	NO	^{13}CO
18	Li_3MoS_2	MAS	NO	NO	THF
19	MoS_2	MAS	YES	NO	THF
20	Li_3MoS_2	MAS	NO	NO	THF
21	Li_xMoS_2 (cells)	MAS	NO	NO	THF
22	Li_1MoS_2	Static	NO	NO	THF
23	Li_3MoS_2	Static	NO	NO	THF

Figure 5 Apparatus for BET surface area analysis and preparation of NMR samples.

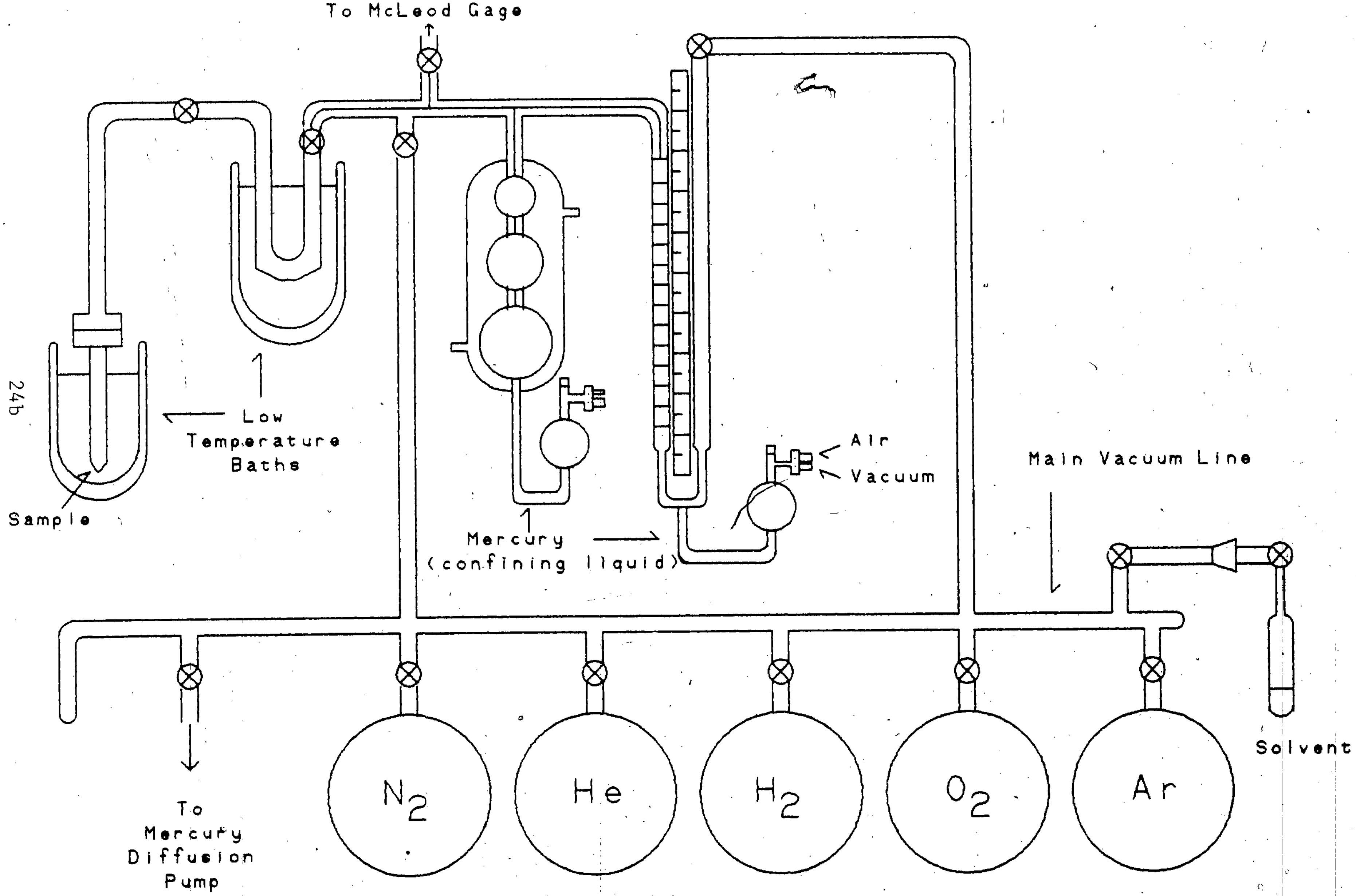

To McLeod Gage
Air
Vacuum
Main Vacuum Line
Low
Temperature
Baths
Sample
Mercury
(confining liquid)
Solvent
To
Mercury
Diffusion
Pump
N$_2$
He
H$_2$
O$_2$
Ar

2.2.4 Selective Pulse NMR Experiments

Experiments in 1973 by Pines, Gibby and Waugh(23) to obtain high resolution spectra of rare spins on solids known as "Proton Enhanced NMR of Dilute Spins in Solids" were a breakthrough in solid-state NMR. Coupled with magic angle spinning, a revolution in solid-state NMR began.

Various techniques were used in this ^{13}C-NMR study. Proton-Enhanced Nuclear Induction Spectroscopy, a cross-polarization technique was primarily used along with a variation utilizing delayed decoupling.(24) In addition to cross-polarization techniques, spectra were collected by excitation of ^{13}C with 90° pulses with and without continuous decoupling of protons using the pulse sequence of Duncan *et al.*(25)

In solid-state NMR two problems are encountered. The dipolar interactions are not equal to zero and spin-lattice relaxation times (T_1) for some species including ^{13}C approach infinity. It has already been seen how the dipolar interaction problem is solved by magic angle spinning. The following will now focus on the latter problem, long T_1's which lead to very long acquisition times in multiple pulse experiments.

The cross-polarization technique is based on the transfer of polarization from an abundant I spin species to a rare S spin species utilizing the Hartmann-Hahn condition (26):

$$\gamma_I B_{1I} = \gamma_S B_{1S} \qquad \text{Eq.5}$$

where γ is the gyromagnetic ratio and B_1 is the applied r.f. magnetic field. In our case the abundant species with large magnetization are ^1H and the rare species with less magnetization are ^{13}C.

In the single-contact cross-polarization (CP) experiment, shown schematically in Fig.6(a), the protons are spin-locked at resonance B_{1H} with a 90° pulse about the x axis. An additional π phase shift on alternate polarizations is used to perform "spin-temperature reversal."(27) The phase of the $\pi/2$ pulse is changed by 180° on alternate scans. The true CP signals invert with each pulse as opposed to the unwanted signals which do not. Thus, addition and subtraction of alternate pulses allows the acquisition of true CP signals and cancels any spurious artifacts.

The ^{13}C species are brought into contact with the protons using a resonant B_{1C} frequency satisfying the Hartmann-Hahn condition (Eq.5). The magnetization of the protons M_H is partially transferred to M_C of the carbons which grow rapidly into a spin lock as indicated by the curves within the B_1 irradiation blocks. The B_{1C} r.f. field is then removed and the ^{13}C free induction decay (f.i.d.) observed while spin decoupling of the protons continues.

Figure 6 Pulse Sequence

a) Pulse diagram of the single-contact cross-polarization experiment.

b) Pulse diagram of the single-contact delayed decoupling cross-polarization experiment.

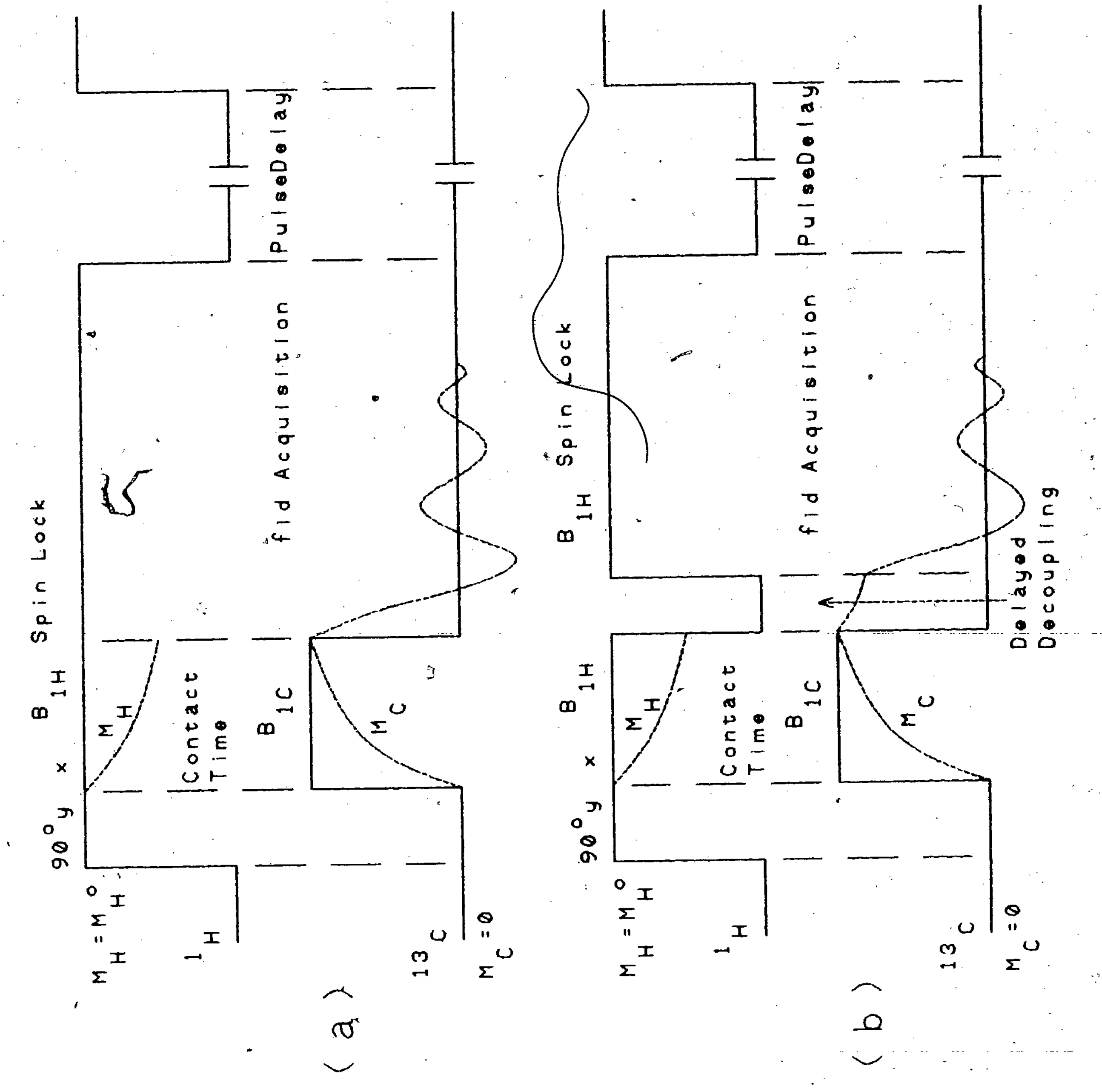
(a)
(b)
$M_H = M_H^o$
^1H
^{13}C
$M_C = 0$
90^o_y
$\times$
B_{1H} Spin Lock
M_H
Contact Time
B_{1C}
M_C
fid Acquisition
PulseDelay
Delayed Decoupling

This experiment is repeated, successive ^{13}C spin f.i.d.'s are accumulated using a computer and stored for later retrieval. Prior to Fourier transform of the f.i.d., a baseline correction is done to eliminate spikes produced near zero frequency which have no physical meaning. These spikes occur when the f.i.d. contains a small DC bias which prevents the average value of the data points from being zero.

At the cost of additional line broadening, a smoothing function is used in the time domain to increase apparent signal-to-noise in the frequency domain. The f.i.d. is multiplied by exp(nTC/N) where N is the number of data points, n is the index of the current point varying from 0 to N-1 and TC is a time constant with a negative value. Intuitively one can see that multiplying with a decaying exponential should improve the signal-to-noise as most of the noise appears in the tail of the f.i.d. where the signal is weak or approaches zero.

Fourier transform of the data is then calculated yielding a frequency domain spectrum consisting of N/2 real points and N/2 imaginary points corresponding to the cosine and sine transforms of the time domain data. Given a signal or f.i.d. in the time domain, S(t) the formal definition of the Fourier transform of the signal to the frequency domain $S(\omega)$ is:

$$S(\omega) = \int_{-\infty}^{\infty} S(t)e^{-i\omega t}dt \qquad \text{Eq.6}$$

$$S(\omega) = \int_{-\infty}^{\infty} S(t)[\cos\omega t + i\sin\omega t]dt \qquad \text{Eq.7}$$

where ω is the angular frequency and t is time. Finally phase correction is necessary due to "mixing" between the real and imaginary parts of the spectra.

A delayed decoupling variation of the single-contact cross-polarization experiment is shown schematically in Fig.6(b). The previous pulsing technique utilizes the rapid transfer of the large ^1H magnetization to the ^{13}C spins therefore spectra obtained discriminate in favor of static carbons which are bonded to protons. Using a delay prior to proton decoupling all carbons which are bonded to protons have their M_C's effectively reduced to zero and therefore do not appear in the final Fourier transformed spectra. This is a useful test to distinguish between organic groups such as aldehydes and ketones which have similar chemical shifts.

Rapidly moving physisorbed species such as rotating methyl groups and gaseous species where the dipolar interaction is averaged to zero by motion will produce very small signals using cross-polarization experiments. Thus experiments using 90° pulses of ^{13}C with and without continuous proton decoupling were performed.

Differentiation between ethylene and carbon dioxide with similar chemical shifts was possible by running this experiment with and without continuous decoupling. Although the patterns are expected to be similar with proton decoupling they will vary dramatically without decoupling.

2.3 Electrochemical Cells

2.3.1 Cell Components

Electrochemical cells consisting of lithium anodes, electrically non-conducting separators and high and low surface area MoS_2 cathodes were prepared in an argon glove box.

Cathodes were prepared by coating an aluminum or nickel foil current collector with a slurry of MoS_2 and 1,2-propanediol(Fisher). The solvent was evaporated in an argon flow at 200°C for ½h. Cathodes of dimension 1.2X1.2cm contained 50-80mg of high surface area or 80-100mg of low surface area MoS_2 powder(Endako).

Lithium foil, 0.013cm in thickness was used yielding a minimum Li/MoS_2 molar ratio of 20, calculated for Li_1MoS_2. This ensures that MoS_2 will be the capacity-limiting species in the cell.

The electrodes were separated by a microporous polypropylene film(Celanese). Cells with 1M $LiAsF_6$ (Lithco) in propylene carbonate(Texaco) (vacuum distilled) were assembled with pre-soaked (pressure wet at 1135 kPa)(150 psig) separators and cathodes to which $\approx 100\mu l$ of electrolyte had been added.

Due to the volatility of tetrahydrofuran, cells utilizing 1M $LiAsF_6$/THF as the electrolyte were assembled with dry separators and cathode. These cells had a small hole in the bottom through which pressure wetting (1135 kPa) (150 psig) of the separator and cathode could be done. These special cells were later sealed by welding a small mild steel ball into the hole or they were used as is for gas evolution studies.

2.3.2 Cell Assembly

A diagram of the experimental test cell is shown in Fig.7. The anode-separator-cathode sandwich is placed between two metal contact plates. One metal contact plate is in direct contact with the can and the other is connected to a centre pin using a nickel foil tab. The electrodes are electrically isolated using a glass-to-metal seal between the centre pin and the cell lid and polypropylene insulators between the spring and the cell can and lid. This spring is used to generate an electrode stack pressure of 1379±138 kPa (200±20 psi).

The cell is hermetically sealed using a TIG welder to join the cell can to the rim of the cell lid. The entire cell assembly process is performed in an argon filled glove box, with the exception of wetting the THF solvent cells which is done inside a dry-room with <1% relative humidity.

Figure 7 An experimental test cell.*

* Drawing from Moli Energy Ltd.

Figure 7b An exploded view of the cathode-separator-anode components of the experimental cell.**

** Drawing taken from R. Fong. M.Sc. thesis. Simon Fraser University, Burnaby, B.C. 1987.

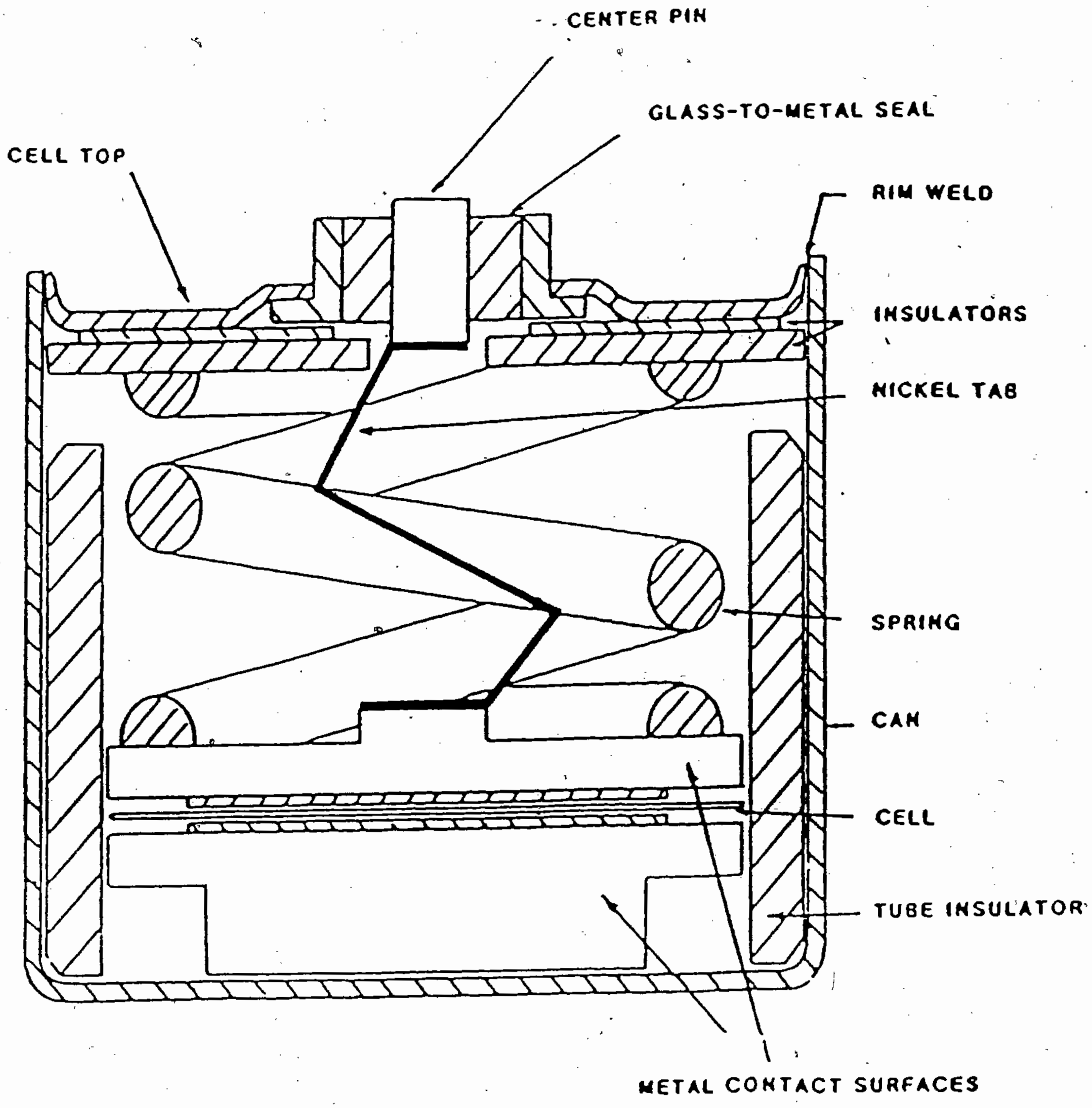
CENTER PIN
GLASS-TO-METAL SEAL
CELL TOP
RIM WELD
INSULATORS
NICKEL TAB
SPRING
CAN
CELL
TUBE INSULATOR
METAL CONTACT SURFACES

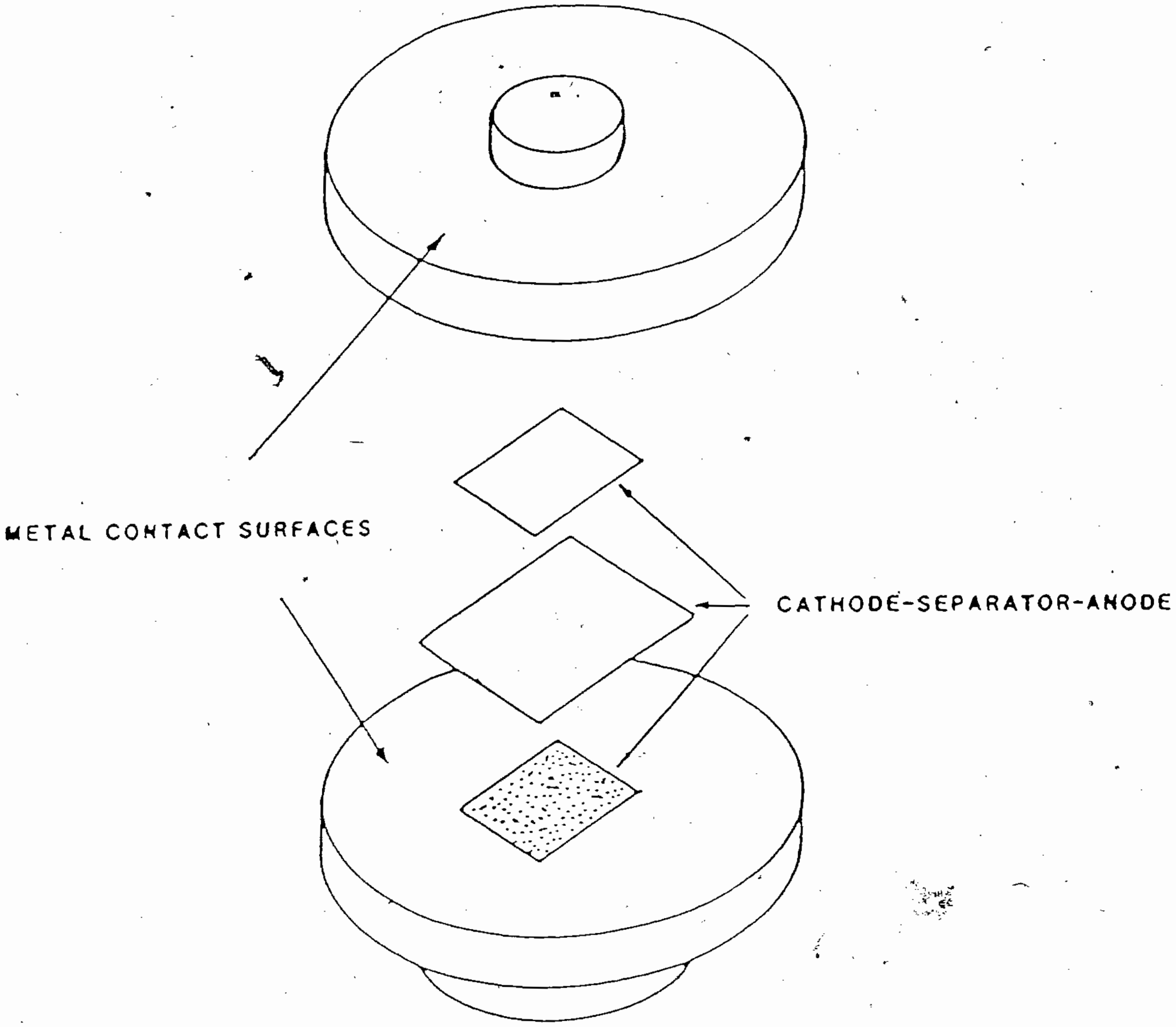
METAL CONTACT SURFACES
CATHODE-SEPARATOR-ANODE

2.3.3 Gas Evolution Cells and Apparatus

Cells for gas evolution studies were assembled with small holes in the bottom of the cans. Special cell holders were used to allow temperature regulation via an aluminum block heat sink. These holders were connected to the gas evolution apparatus using a narrow teflon tube (0.032cm I.D., ≈30cm in length).

The gas evolution apparatus is described in detail by Fong *et al*(28). A schematic diagram of the constant-pressure gas evolution apparatus is shown in Fig.8. As gas is evolved from the cell during a discharge or recharge the pressure inside the closed system increases over atmospheric pressure. A differential pressure transducer senses the increase, relays this information to the microprocessor control unit which then attempts to reduce the differential pressure to zero.

A stepping motor is used to move a gas-tight syringe plunger, increasing the volume in the closed system and thereby reducing the inside pressure to equal the atmospheric pressure. Each step of the motor changes the dead volume 1.12μl; every ten steps or 11.2μl is equivalent to a lmV signal. An analog signal corresponding to the syringe movement is stored by a datalogger in tandem with the voltage of the cell as a function of time.

Figure 8 Schematic diagram of the gas evolution apparatus.

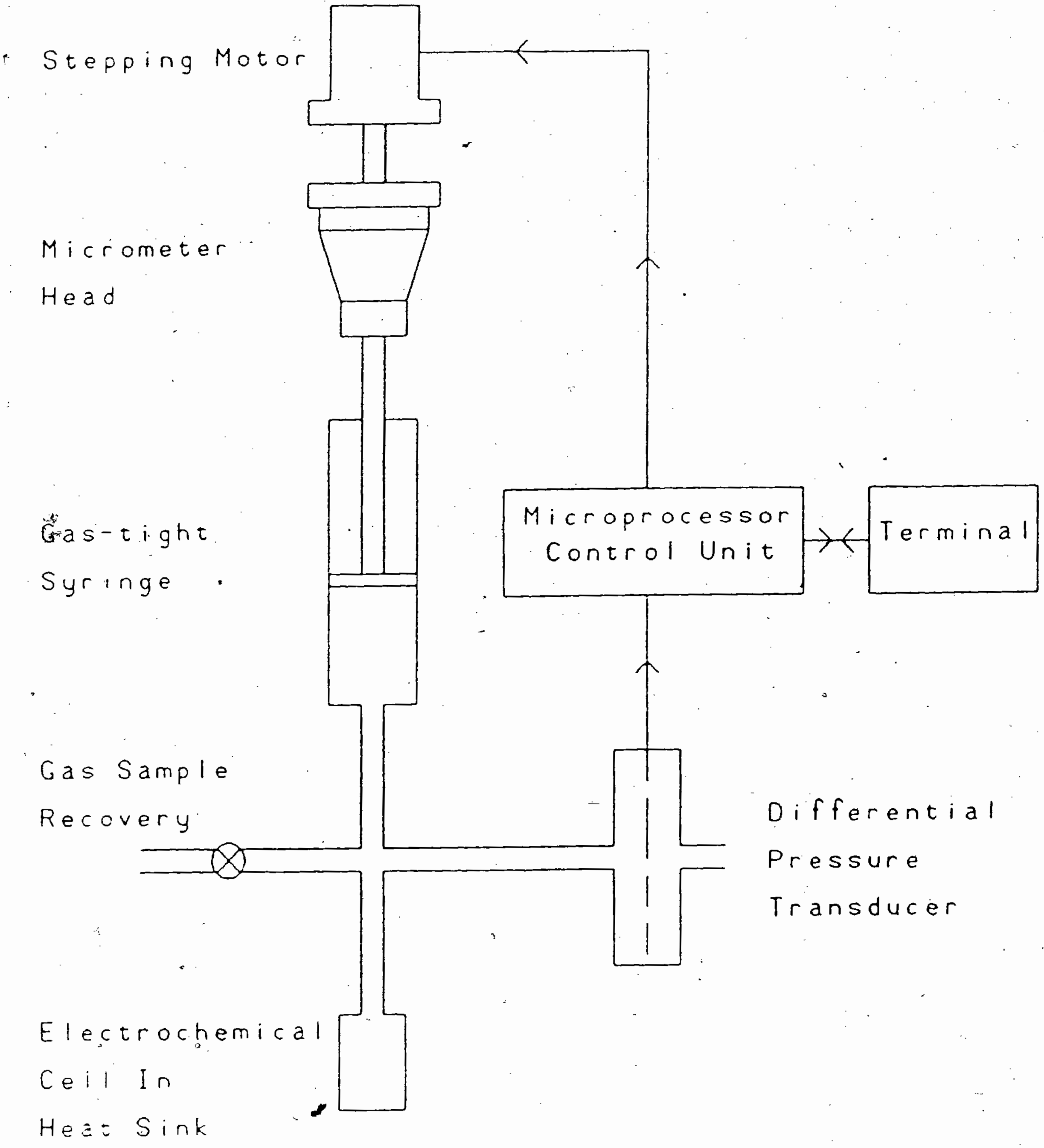
Stepping Motor
Micrometer Head
Gas-tight Syringe
Gas Sample Recovery
Electrochemical Cell In Heat Sink
Microprocessor Control Unit
Terminal
Differential Pressure Transducer

2.3.4 Electrochemical Measurements

All electrochemical cells prepared in this study were discharged and recharged at constant current at 21.0 ± 0.5°C and their voltages monitored as a function of time. The currents generated by the cyclers were stable to within 2%. Cycling switch points were controlled by time or fixed voltage limits.

To calculate x in Li_xMoS_2 one uses:

$$x = \frac{I\ t\ M}{m\ F} \qquad \text{Eq.8}$$

where I is the current (A), t is the discharge or recharge time (sec), M is the molecular weight of the cathode, m is the cathode mass (g) and F is Faraday's constant. Constant current setting calculated for each cell correspond to a transfer of $x = 1$ lithium per MoS_2 in either 10 or 20 hours. (C/10 or C/20 rate where C rate $\equiv \Delta x{=}1$ in 1h) Difficulties in accurate quantitative determination of lithium transfer are encountered due to cathode particles which are electronically isolated from one another and the current collector and also side reactions of lithium with the electrolyte. As a result the errors in x may be as large as 20%.

Typically the first discharge was timed to a specific value of x with subsequent cycling between fixed voltage limits allowing maximum x

values. Due to its stability within the voltage ranges used, 1M $LiAsF_6$/PC was chosen as the standard electrolyte.

Using plots of cell voltage V versus lithium content x in Li_xMoS_2 and plots of the derivative $|(\partial t/\partial V)|_T$ plotted versus V, it was possible to compare high and low surface area MoS_2 cathode material. The derivative plots were especially useful as plateaus in the V(x) curves are sometimes difficult to see but as peaks in the derivative plots, they are easily observable.

2.4 X-ray Powder Diffraction

Powder diffraction is a technique used to identify unknown crystalline materials, analyze mixtures, detect phase changes and determine precise lattice constants. In X-ray powder diffraction 3-dimensional information and symmetry is projected in 1-dimension. X-ray diffraction principles and theory are well established (29) and therefore will only be mentioned briefly.

Diffraction of a monochromatic beam of X-rays by a crystal is due to sets of parallel equidistant lattice planes according to Bragg's law:

$$d = n\lambda / 2\sin\theta \qquad \text{Eq.9}$$

where d is the distance between the lattice planes (hkl) in the crystal, n is an integer, λ is the wavelength of incident radiation and θ is the Bragg angle (2θ is the actual angle between the incident and diffracted beams).

Intuitively, from Bragg's law one discovers that crystallinity is necessary to obtain sharp diffractions, commonly called reflections. Greater numbers of lattice planes with equivalent parallel spacing in crystalline materials yield stronger, sharper reflections as opposed to amorphous and poorly crystalline materials which typically have fewer parallel lattice planes. X-ray powder diffraction patterns for poorly crystalline materials tend to have very broad peaks or none at all.

Nickel-filtered copper K_α radiation and a Phillips powder diffractometer equipped with a modified vertical goniometer were used to obtain the diffraction data. The motor control of the goniometer was accurate to $2\theta = 0.01°$, however variations in sample thickness may lead to a systematic shift in 2θ, typically 0.1° or less.

Samples were prepared on the flat surface of a glass slide or an air-tight X-ray diffraction cell. Powder was sprinkled onto a film of silicone grease(Dow Corning) and a uniform layer was achieved after excess powder was tapped off. The sealed X-ray case shown in Fig.9, was used for air-sensitive materials. Diffraction of X-rays by electrons in the window is minimized by using a low atomic weight metal, beryllium. Figure 9 also shows that this case may be used as an *in-situ* X-ray diffraction electrochemical cell holder. This cell holder is previously discussed in greater detail by Dahn *et al*(30). The cell holder has been used to study the phase changes which occur as lithium is intercalated into various cathode materials.(6,31) This was not possible in this study due to the poor crystallinity of the high surface area MoS_2 prepared for these NMR experiments.

X-ray powder diffraction patterns were useful for determining crystallinity of prepared molybdenum sulfide before and after lithiation. This was a good indication of the surface area of a sample as higher surface area was consistent with decreasing crystallinity.

Figure 9 An *in-situ* X-ray powder diffraction cell holder.* This sealed case was used for air-sensitive materials in this study and not for Li/MoS_2 cells as shown in the diagram.

* Drawing taken from J.R. Dahn *et al*. Can. J. Phys. **60**, 307 (1982).

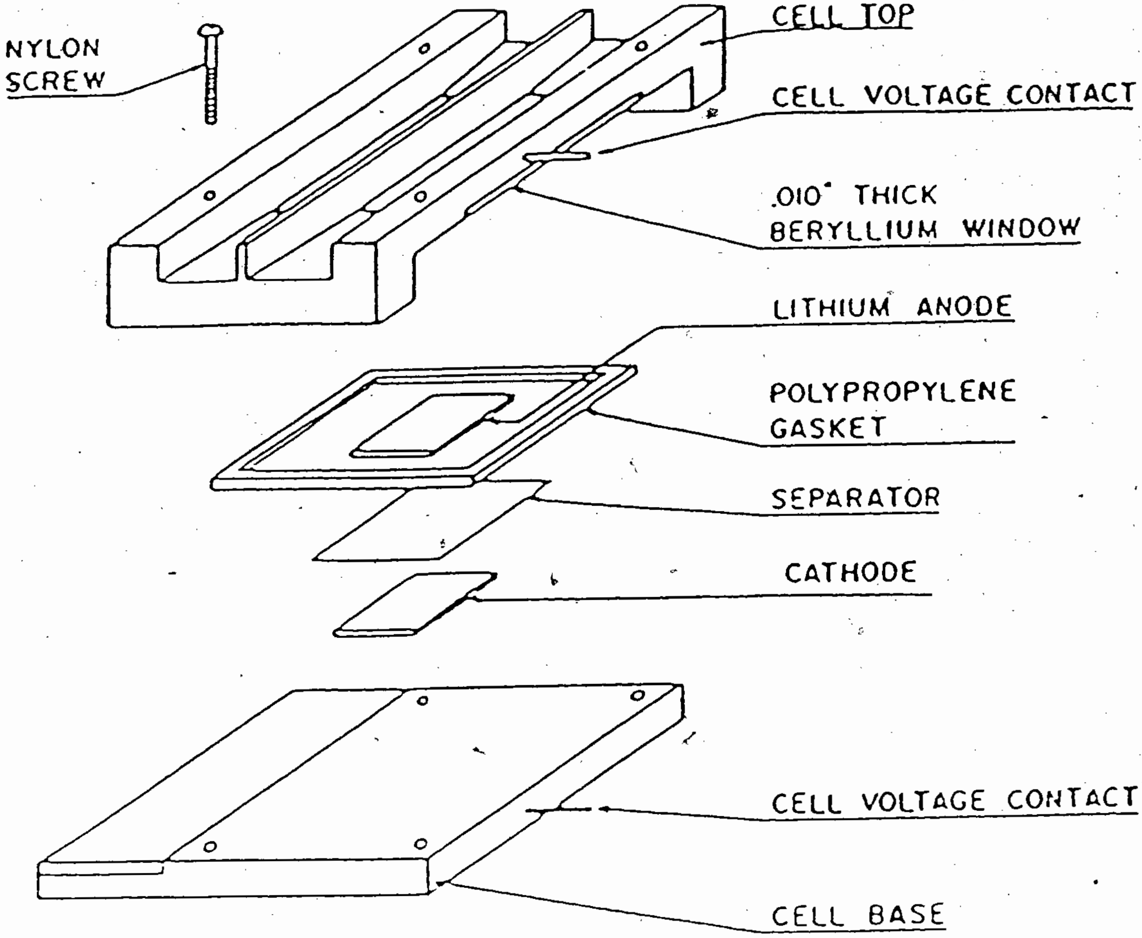
NYLON SCREW
CELL TOP
CELL VOLTAGE CONTACT
.010" THICK BERYLLIUM WINDOW
LITHIUM ANODE
POLYPROPYLENE GASKET
SEPARATOR
CATHODE
CELL VOLTAGE CONTACT
CELL BASE

This technique was also useful in verifying the purity of ammonium tetrathiomolybdate synthesized for this work. The powder pattern for this compound was calculated (32) using the single crystal structure information collected by Wyckoff.(33) Although only the cell dimensions a_o, b_o, c_o, are known for ATTM, the atom positions are considered to be similar to those determined for ammonium tungsten tetrasulfide which also has an orthorhombic pseudohexagonal unit structure.

2.5 Brunauer-Emmett-Teller Surface Area Determination

Physical adsorption of gases is commonly used for determining total surface area and pore structure of powders. A typical isotherm is shown in Fig.10. Isotherms are broken down into three useful sections:

a) in the Henry law region ($p/p_o < 0.01$), adsorption is normally proportional to pressure, surface area and the Henry law constant,

b) in the monolayer coverage region ($0.1 < p/p_o < 0.3$), sorption begins to level off, becoming proportional to surface area and (molecular area)$^{-1}$,

c) in the multilayer-capillary condensation region ($0.3 < p/p_o < 1.0$), sorption increases rapidly but levels off when the pores are filled. This region is used to determine surface area and pore structure.

The Brunauer-Emmett-Teller (BET) method(34) utilizes the monolayer coverage region and was used in this study. In this region we used the following equation:

$$\frac{p}{V(p_o - p)} = \frac{1}{V_m C} + \frac{C-1}{V_m C}\,\frac{p}{p_o} \qquad \text{Eq.10}$$

Figure 10 An ideal S-shaped adsorption isotherm.

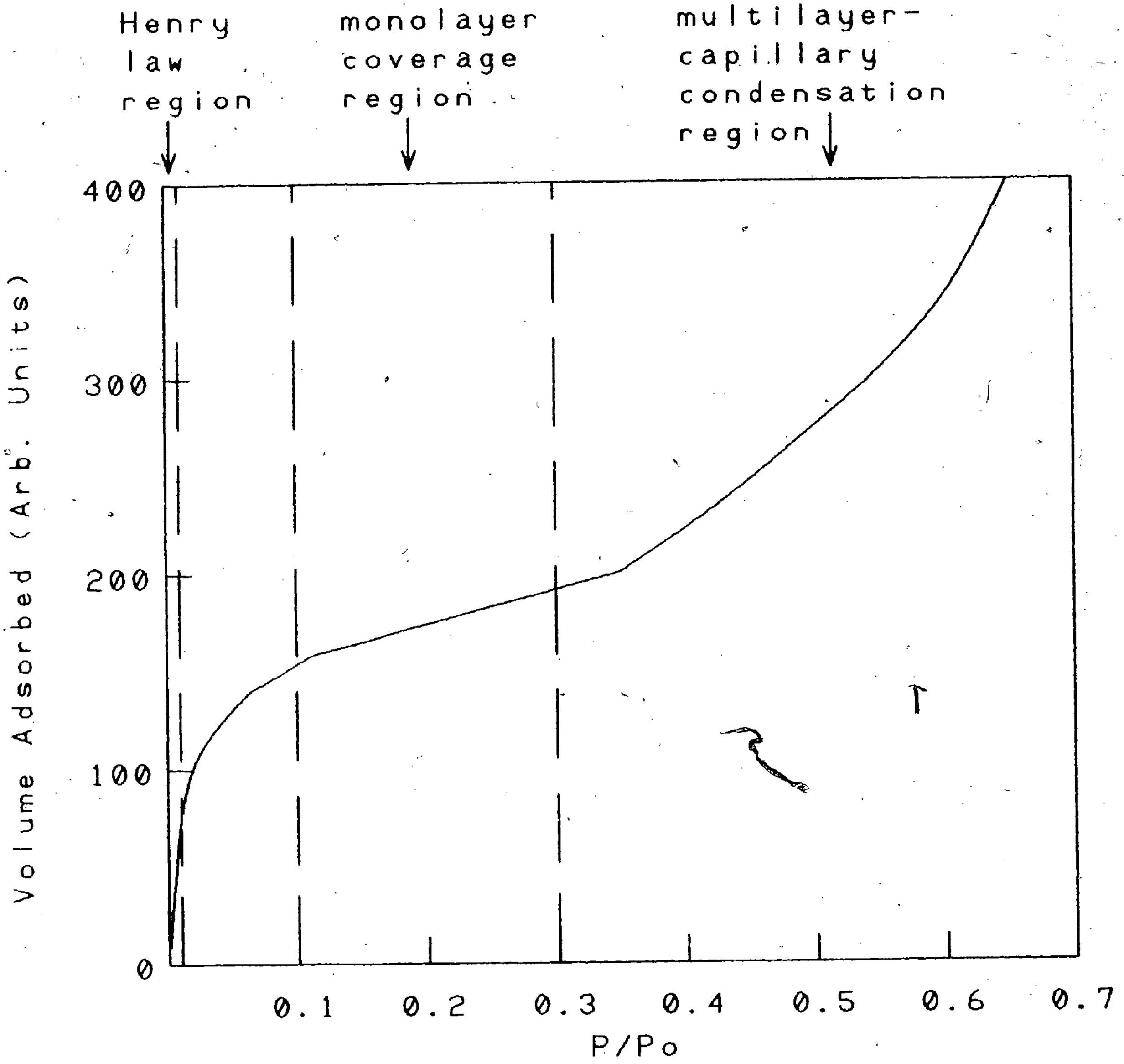
Henry law region
monolayer coverage region
multilayer-capillary condensation region
400
300
200
100
0
0.1
0.2
0.3
0.4
0.5
0.6
0.7
P/Po
Volume Adsorbed (Arb. Units)

Plotting $p/V(p_0 - p)$ versus p/p_0 gives a straight line where $0.1 < p/p_0 < 0.3$, whose intercept is $1/V_mC$ and slope is $(C - 1)/V_mC$. The two constants V_m and C are calculated from the slope and intercept. The former constant, V_m, is the volume of gas required for complete unimolecular adsorbed layer coverage of the sample. Using the surface area value of 16.2Å^2 per molecule of nitrogen(35), it is possible to calculate the total surface area of the sample:

$$S_{BET} = \frac{V_m(\text{ml})}{22414} \text{ X } 16.2\text{Å}^2 \text{ X } N \text{ X } 10^{-20} \qquad \text{Eq.11}$$

where N is Avogadro's number.

The latter constant C is approximately equal to $e^{E1-EL/RT}$, where E_1 is the average heat of adsorption of the first layer and E_L is the heat of liquification. Small values of C correspond to weak interactions between adsorbate and gas molecules while large values of C correspond to strong interactions.

Three and four point BET analyses were used in this study although Brunauer *et al* claim single point analysis should give valid results.(34) This ensured reliability in the collected data.

2.6 Thermal Gravimetric Analysis

In thermal gravimetric analysis, the mass of a sample is measured as a function of temperature in a controlled atmosphere. Typically samples are tested for thermal stability under inert atmospheres where weight losses correspond to liberated gases. Reactions of materials with various gases as a function of temperature may also be studied using this technique.

Previously in the elemental analysis of synthesized MoS_x, each element was determined separately.(36) Molybdenum sulfides were dissolved in aqua regia and diluted for molybdenum determination using atomic absorption. Sulfur was determined using a gravimetric technique. Molybdenum sulfide was oxidized in a hot mixture of bromine, carbon tetrachloride and nitric acid and the resulting precipitate was dissolved with hydrochloric acid. When cooled, $Ba(NO_3)_2$ was added to precipitate $BaSO_4$ which was filtered, dried and weighed.

To simplify the elemental analysis of MoS_x, a method utilizing thermal gravimetric analysis was developed. A Dupont 9000 Thermal Analyzer with a 951 Thermogravimetric Analyzer (TGA) plug-in module was used. This procedure is based on the reaction of MoS_x to MoO_3 when heated in the presence of oxygen. The weight loss in the reaction allows the determination of x in MoS_x to within 1%.

Parameters for the determination of the S/Mo ratio were:

1) Ramp 25°C/min to 550°C

2) Isothermal 20 min.

To calculate x in MoS_x the following equation was used:

$$x = \frac{100\left[\frac{\mathrm{M.W.(MoO_3)}}{100 - \delta}\right] - \mathrm{M.W.(Mo)}}{\mathrm{M.W.(S)}} \qquad \text{Eq.12}$$

where δ is the change in mass in percent.

Thermal gravimetric analysis was also used to verify that the prepared molybdenum sulfides were discrete compounds and not mixtures of MoS_2 and sulfur. If elemental sulfur was present one would expect weight loss below 300°C. The chemical composition and purity of ammonium tetrathiomolybdate were also determined by thermal gravimetric analysis under an inert atmosphere.

2.7 Residual Gas Analysis

Chemical reactions involving the reaction and/or formation of gaseous products are routinely monitored using residual gas analysis. It is possible to study reactions in progress by monitoring the partial pressures of various gases through the use of a mass spectrometer.

Residual gas analysis was performed using a Spectramass DataQuad spectrometer which uses a quadrupole mass filter. A Pfeiffer turbo pump creates a high vacuum ($<10^{-4}$ torr) as ionization of a sample by electron bombardment must occur in the vapour state. After the formation of ions, a mass analyzer using 4 electric poles (quadrupole) without a magnetic field separates ions according to their mass-to-charge (m/e) ratio. Applying both a dc voltage V and a radio-frequency voltage Vo to the poles, the ions travelling down the length of the quadrupole oscillate. As the oscillations are dependent on the m/e ratio of an ion, set values of V and Vo will allow only a single m/e value to traverse the entire distance without striking one of the poles. Each value of m/e is measured separately for a short period of time. The ions are focussed into a Faraday cup detector which produces a very small dc signal, which is amplified and sent to the Spectramass DataQuad control unit.

Continuous mass spectrometric analysis of varying gas samples at atmospheric pressure is a unique feature of residual gas analysis. A schematic diagram shown in Fig.11, illustrates the gas inlet system, an important feature. A capillary inlet with bypass consists of a length of S.S. capillary (0.325mm I.D., 1.0m in length) and a molecular flow leak. Due to the possibility of condensation of some gases the capillary is heated to ≈70°C. The bypass is connected via a low vacuum (≈10torr) line to a rotary pump, thus constantly providing fresh gaseous samples at the entrance site to the mass spectrometer. The molecular flow leak allows minute amounts of gas to enter the main high vacuum ($<1 \times 10^{-4}$torr) chamber which houses the ionizing filament, quadrupole mass filter and Faraday cup. The capillary inlet was situated in the gas output flow of a heated quartz reaction tube (52mm O.D., 1.2m in length).

Continuous sweeping of m/e values is possible over all values within set ranges. However more precise data were accumulated by choosing only the m/e values of interest to the thermal decomposition reactions involved. The data collected for each m/e value are recorded as a partial pressure of the high vacuum chamber and datalogged with an IBM-PC compatible computer in an ASCII form. This method of data storage allows a wide variety of graphic presentation forms.

Figure 11 Schematic diagram of the residual gas analysis spectrometer connected via a capillary tube to the thermal decomposition apparatus.

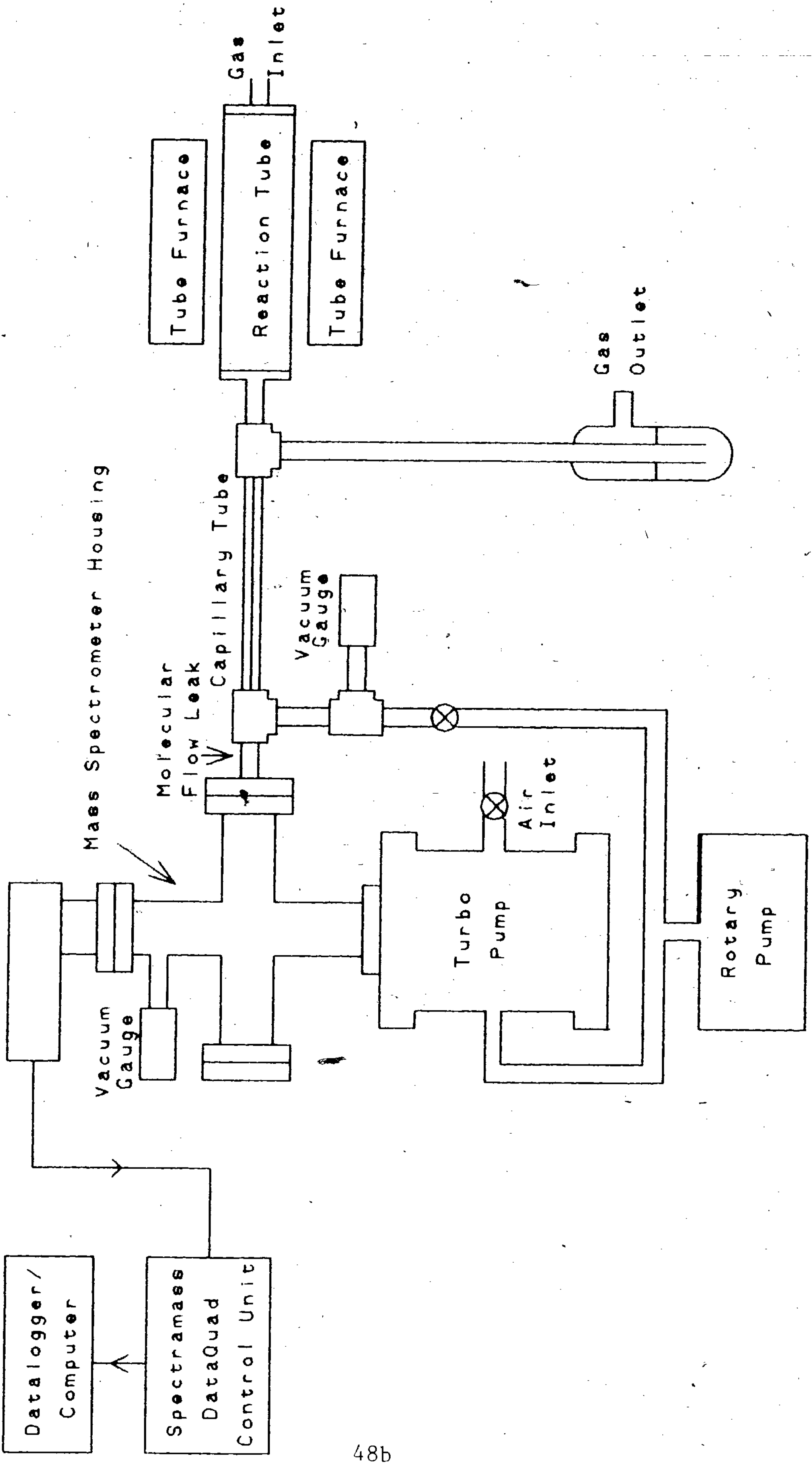
Gas Inlet
Tube Furnace
Reaction Tube
Tube Furnace
Gas Outlet
Capillary Tube
Mass Spectrometer Housing
Molecular Flow Leak
Vacuum Gauge
Air Inlet
Turbo Pump
Rotary Pump
Vacuum Gauge
Datalogger/ Computer
Spectramass DataQuad Control Unit

3.0 RESULTS AND DISCUSSION

3.1 Li_xMoS_2 Synthesis Introduction

Preparing molybdenum disulfide, MoS_2 from ammonium tetrathiomolybdate, $(NH_4)_2MoS_4$ resulted in high surface area powders. Initially other high surface area preparations were attempted but with little success. The experiments are described below.

3.1.1 Li_xMoS_2 Exfoliation

MoS_2 powder was exfoliated by first intercalating lithium and then reacting the powder with water at various pH values as described by Joensen et al.(37) Single layer MoS_2 in suspension is produced as the H_2 evolved in the reaction "blows" the layers apart.

$$Li_1MoS_2 + (1+x)H_2O \xrightarrow[\text{soln}]{\text{acidic}} MoS_2(H_2O)_x + LiOH + \tfrac{1}{2}H_2 \qquad \text{Eq.13}$$

Removal of the bulk water left water bilayers between the MoS_2 layers as seen in X-ray diffraction patterns. Restacking of the layers during drying resulted in low surface areas, generally $<2m^2/g$.

3.1.2 Low Temperature Solution MoS_2 Preparation

We made low temperature solution preparations of MoS_2 and MoS_3 using a sulphiding agent and a molybdenum halide dissolved in tetrahydrofuran or an aqueous NH_4OH solution.(38)

$$MoCl_4 + 2A_2S \xrightarrow{soln} MoS_2 + 4ACl \qquad \text{Eq.14}$$

$$MoCl_4 + 2AS \xrightarrow{soln} MoS_2 + 2ACl_2 \qquad \text{Eq.15}$$

$$MoCl_5 + 5/2(A_2S) \xrightarrow{soln} MoS_2 + 5ACl + ½S \qquad \text{Eq.16}$$

$$MoCl_5 + 5/2(AS) \xrightarrow{soln} MoS_2 + 5/2(ACl2) + ½S \qquad \text{Eq.17}$$

Molybdenum halides used were molybdenum (IV) chloride and molybdenum (V) chloride. We used lithium sulfide, Li_2S, lithium bisulfide, LiHS, thioacetamide, CH_3CSNH_2 and tert-butyl sulphide, $[(CH_3)_3C]_2S$ as sulphiding agents.

Typical yields were small, powders were very fine, X-ray powder diffraction results were inconclusive as to composition and surface areas were low, generally $<5m^2/g$.

3.1.3 Two Step Thermal Decomposition

Many samples were prepared by thermally decomposing ammonium tetrathiomolybdate, $(NH_4)_2MoS_4$ in an inert gas to molybdenum trisulfide, MoS_3. The MoS_3 was subsequently reduced to molybdenum disulfide, MoS_2 in a reducing atmosphere. This two step thermal reaction is discussed further in section 3.2.1 of the residual gas analysis results. Many authors have used the thermal decomposition of ATTM or MoS_3 to prepare MoS_2 catalyst with surface areas ranging from 1 to $158 m^2/g$.(39-43)

It was possible to achieve surface areas up to $49 m^2/g$ using the two step thermal decomposition of ATTM decribed above but the results were inconsistent. Achieving both a low S/Mo ratio (≈ 2) and high surface area was difficult. Variations in sample size, heating rate and temperature affected surface area and S/Mo ratios. There appeared to be an optimum temperature which implied competition between the two processes: desulfurization, exposing vacant sites on the surface yielding higher surface area and crystallization of MoS_2 yielding lower surface area. Best results were obtained by rapidly heating a small sample (<3g) spread evenly in an alundum or stainless steel boat. The sample was pushed into a tube furnace heated to 350°C. In this two step decomposition a 1h exposure to argon is followed by 1h of 5% H_2/Ar, 15% H_2/He or 100% H_2.

3.1.4 Acidic Aqueous Precipitation of MoS_3

Finally we attempted the precipitation of molybdenum (VI) from ATTM in acidic aqueous solution saturated with hydrogen sulfide.(18,36) This gave amorphous MoS_3 with varying densities and surface areas.

Initially, inorganic acids such as sulfuric and nitric were used in this chemical decomposition. We varied the temperature (0°C or room temperature), the agitation (stirring or ultrasonic vibration), the type and strength of acid, the size of ATTM crystals, the pH of the solution before ATTM was dissolved and the drying procedure (under argon at 100°C or under vacuum). The surface areas for MoS_3 prepared in these experiments ranged from 3 to $74m^2/g$.

When we replaced the inorganic acids with an organic acid, formic acid, we found a major increase in resulting surface areas. Once perfected, this technique gave MoS_3 with surface areas consistently between $190\text{-}240m^2/g$ and densities from 1.3-1.6g/ml.

3.1.5 Thermal Reduction to MoS_2

Various temperatures (200-500°C) and reaction times (4min to 6h) were used to optimize the thermal decomposition of MoS_3 to produce high surface area MoS_2 with a S/Mo ratio of ≈ 2. The best results were obtained at 250°C for 2h under $15\% H_2/He$ followed by a brief exposure to argon (10 min) to remove H_2 from the MoS_2 surface. Resulting surface areas were 70-110m^2/g.

Adsorption of carbon monoxide, CO onto thermally reduced MoS_2 reveals surface area due to edge planes(52) as opposed to total surface area determined by nitrogen adsorption. Using the surface area value of 16.0Å^2 per CO molecule(35), the edge plane surface area was determined to be 8.34% of the total surface area for a single MoS_2 sample.

3.1.6 Density Measurements

The densities of all the powder samples were measured by a "tap density" method. Powders were poured into a 4mm I.D. Pyrex® tube, which was tapped on the lab bench until there was no further change in the length of the powder column. The tube and powder were weighed, the length of powder was measured with calipers and the "tap density" was calculated. This method was used, as opposed to the Archimedean method, since it simulates the packing conditions of an MAS NMR tube.

After a review of the density measurements we realized that the density of MoS_3 was lower when commercial ATTM(Aldrich) was used instead of ATTM prepared by the author. The densities for MoS_3 using ATTM(Aldrich) were 0.6-0.8g/ml and for the resulting MoS_2 were 0.9-1.2g/ml. This is susbstantially lower than ρ = 1.9-2.1g/ml for MoS_2 prepared from the author's ATTM.

3.1.7 Lithium Intercalation of MoS_2

The next step was preparing high surface area, Li_xMoS_2, for $1 < x < 3$. In the first attempts we chemically lithiated MoS_2, with surface areas ranging from 40 to 73 m^2/g, using stoichiometric amounts of n-butyllithium in n-hexane. This resulted in surface areas ranging from <1 to 37m^2/g.

The large variation in surface area was related to the density of the MoS_2 starting material. MoS_2 with a density of 1.3g/ml and higher lost its high surface area during chemical lithiation with n-butyllithium in n-hexane during overnight stirring. Surprisingly, similar surface area losses were seen when higher density MoS_2 was stirred overnight in n-hexane solvent or tetrahydrofuran, another common lithiating solvent. We believe this effect may be due to increased ordering or crystal growth. Another possibility involves the solvent clogging the pores of the particles. However, the latter theory was discarded as the powders were evacuated at 100°C prior to BET surface analysis. In contrast, lower density MoS_2 of approximately 0.8g/ml retained its initial high surface area after chemical lithiation. Starting with low density MoS_2 was not desirable as high density, in addition to high surface area, Li_xMoS_2 samples were necessary for the ^{13}C-NMR experiments.

Next we tried lithium dissolved in liquid ammonia (Li/NH_3) to lithiate MoS_2 forming $Li_xMoS_2(NH_3)_y$. This method resulted in larger surface areas ranging from 40-75m^2/g and densities from 0.9-1.2g/ml.

The density of $Li_xMoS_2(NH_3)_y$ increased upon NH_3 removal. This was seen by visual inspection of MAS NMR samples, but was not accurately measured.

The co-intercalated NH_3 was removed from the $Li_xMoS_2(NH_3)_y$ powder by pumping under vacuum at 200-250°C for at least 12h. The removed ammonia was trapped with liquid nitrogen and subsequently measured using a gas-volumetric technique. For $Li_1MoS_2(NH_3)_y$, y was found to be 0.22 by the gas-volumetric method and 0.11 by ion chromatography. For $Li_3MoS_2(NH_3)_y$, y was 0.32. $Li_3MoS_2(NH_3)_y$ reacts more exothermically with water than $Li_1MoS_2(NH_3)_y$ does. To control the heat output of the former reaction, we exposed $Li_3MoS_2(NH_3)_y$ to water vapour for 24h. prior to dumping the powder in water. Ammonia gas was released during this exposure and subsequently did not show up in the ion chromatogram.

The lithium content of $Li_xMoS_2(NH_3)_y$ was determined by ion chromatography. Sample IIIP11 was repeated 4 times giving a value for x of 1.02±0.03. Sample IIIP73 gave a value for x of 3.19 twice.

3.1.8 Li_xMoS_2 Synthesis Summary

Table II outlines the molybdenum sulfide and lithiated molybdenum sulfide samples synthesized, the preparation method, and the surface area and density ranges. A more detailed table listing individual samples is included in Appendix A. Sample I.D.'s (e.g. IIIP97) refer to page numbers (P97) in a laboratory notebook (Roman numeral III).

Table II - Molybdenum Sulfide Powder Synthesis

Powder Type	Preparation Method	Surface Area (m^2/g)	Density (g/ml)
a-MoS_2	Low Temperature Chemical Route	<5	—
t-MoS_3	Thermal using $(NH_4)_2MoS_4$ (350°C)	32^b	—
c-MoS_3	Chemical using $(NH_4)_2MoS_4$	190 - 240	1.3-1.6
t-MoS_2	Thermal using $(NH_4)_2MoS_4$ (350°C)	30 - 50	1.2-1.3
c-MoS_2	Thermal using c-MoS_3 (200-250°C)	70 - 110	1.9-2.1
Li_xMoS_2 (x=1)	Chemical Intercalation of c-MoS_2 using n-BuLi	<1 - 37	—
Li_xMoS_2 (x=1,3)	Chemical Intercalation of c-MoS_2 using Li/NH_3	40 - 75	0.9-1.2

a - "Amorphous"

b - Single measurement value

c - Chemical / Thermal Decomposition

t - Thermal Decomposition

3.2 Residual Gas Analysis Results

3.2.1 Two Step $(NH_4)_2MoS_4$ Thermal Decomposition

The thermal decomposition of ATTM was monitored using residual gas analysis. In addition to the reaction and generated gases in this decomposition, air impurities were also monitored using nitrogen (M28). The sequence of events for this reaction were as follows:

0 min - Data acquisition started, sample placed in end of tube, Ar flow started,

17 min - Tube put into 350°C tube furnace, sample in end of tube at room temperature,

32 min - Sample pushed into furnace using push rod (with O-ring seal),

95 min - Switch to H_2 flow,

140 min - Reaction concluded, data acquisition stopped.

The reaction gases, argon (M40) and hydrogen (M2) are shown in Fig.12. The sensitivity of the RGA spectrometer to individual gases varies dramatically as shown when comparing 100% hydrogen to 100% argon. The rate each gas permeates the molecular flow leak moving into the spectrometer, the partial pressure of each gas, the difference in ionization potentials of gases and the pumping efficiency of the turbo pump for different gases are several explanations. Also note the drop in partial pressure of argon at the point where the sample begins to decompose. This corresponds to an increase in the partial pressures of

Figure 12 Reaction gases used in the two step $(NH_4)_2MoS_4$ thermal decomposition at 350°C.

Figure 13 Gases generated in the two step $(NH_4)_2MoS_4$ thermal decomposition at 350°C.

The background was monitored using M28 (nitrogen).

Figure 14 Y scale expansion of Figure 13.

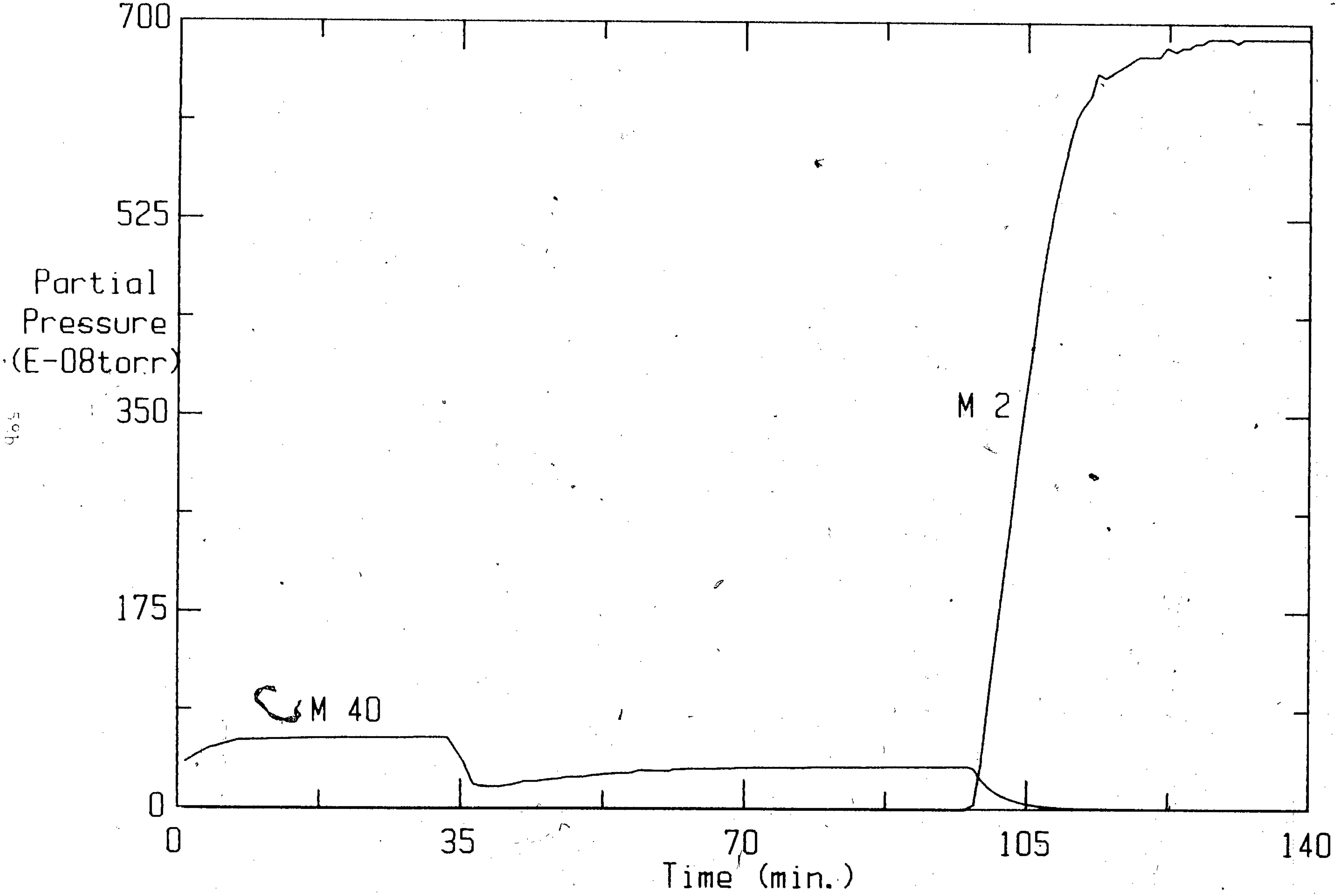
700
525
350
175
0
Partial
Pressure
(E-08torr)
M 40
M 2
0
35
70
105
140
Time (min.)

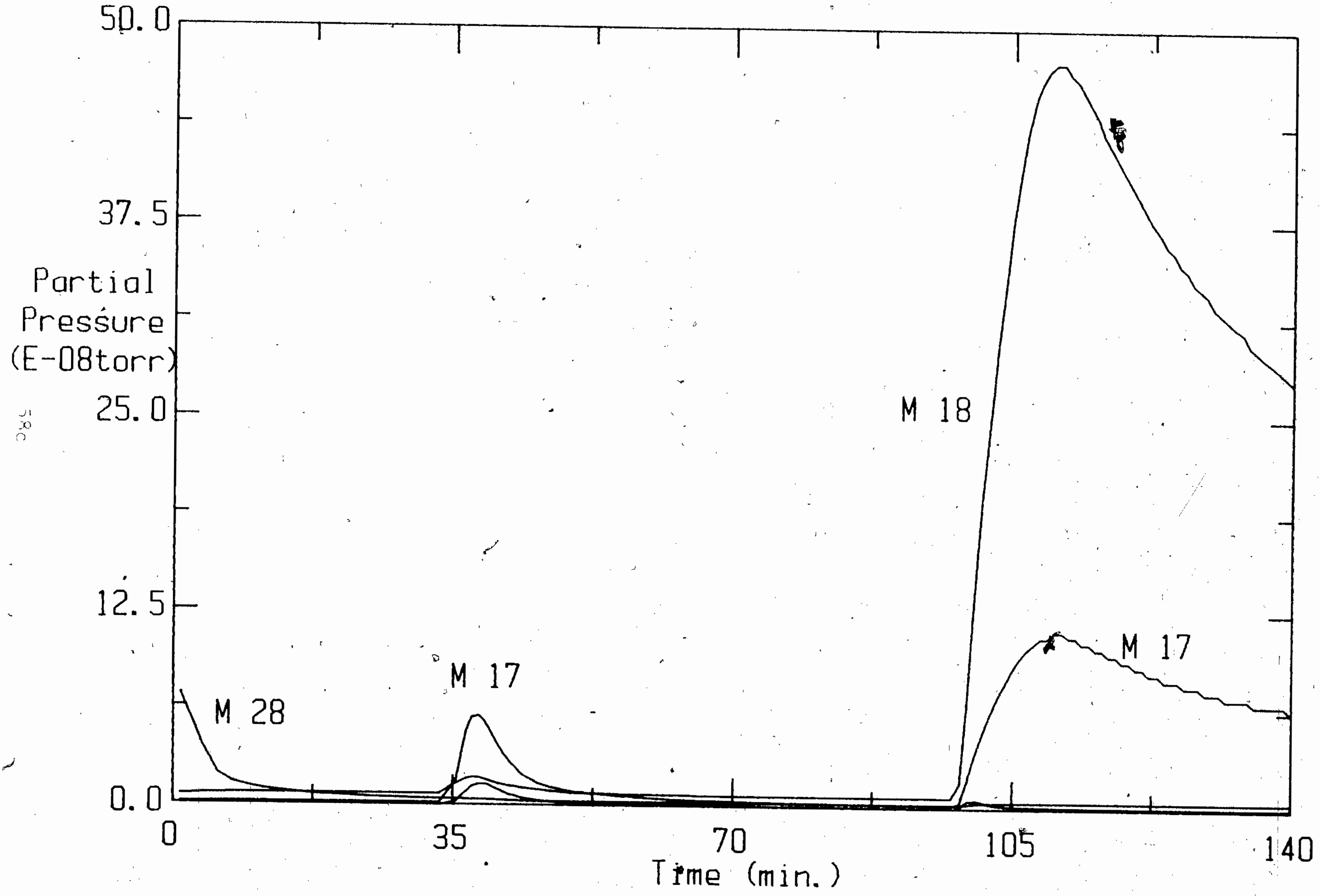
50.0
37.5
25.0
12.5
0.0
Partial Pressure (E-08torr)
0
35
70
105
140
Time (min.)
M 28
M 17
M 18
M 17

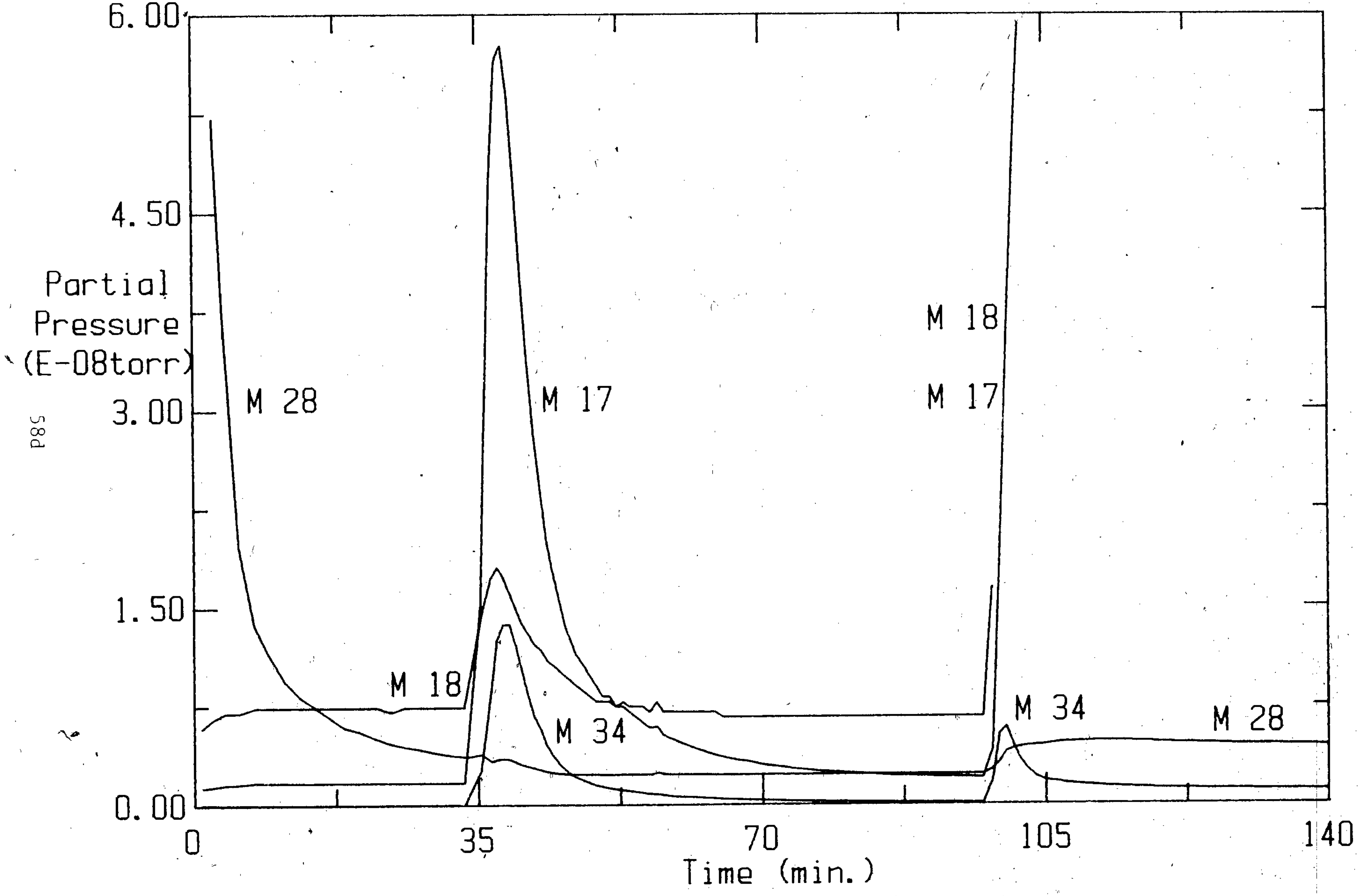
6.00
4.50
3.00
1.50
0.00
Partial
Pressure
(E-08torr)
0
35
70
105
140
Time (min.)
M 28
M 17
M 18
M 34
M 18
M 17
M 34
M 28

other gases shown in the next two figures.

Figures 13 and 14 show the major gases generated in the thermal decomposition of ATTM using different expansions of partial pressure on the y axis. The decreasing nitrogen (M28) background was used to indicate proper flushing of the reaction tube before starting the experiment.

Large water (M18) and H_2O molecular fragment (M17) peaks were seen in all runs where the sample was exposed to hydrogen. The reaction of oxides on the surface of the stainless steel boat with hydrogen gas at elevated temperatures is believed to produce these peaks.

The actual gases generated by the decomposition are shown in the expanded plot, Fig.14. Ammonia (M17) and hydrogen sulfide (M34) are seen after introduction of the sample at 32 min. At this point the M17 peak is generated by ammonia, as an M17 H_2O fragment is always seen as a peak of proportionately smaller size than a M18 H_2O peak. The water peak (M18) is due to evaporation of residual water from the ATTM sample, which was prepared in an aqueous solution. The absence of nitrogen (M28) and hydrogen (M2) peaks indicates the following reaction for the first decomposition step:

$$(NH_4)_2MoS_4 \xrightarrow[\text{Ar}]{350°\text{C}} 2NH_3 + H_2S + MoS_3 \qquad \text{Eq.18}$$

A single hydrogen sulfide (M34) peak is seen at 95 min, after the introduction of hydrogen gas and subsequent reduction of MoS_3. The following reaction may be written for the second step in the thermal decomposition / reduction of ATTM:

$$MoS_3 + (1-x)H_2 \xrightarrow{350^{\circ}C} MoS_{2+x} + (1-x)H_2S \qquad \text{Eq.19}$$

3.2.2 MoS_3 Thermal Reduction

The thermal decomposition or reduction of chemically formed molybdenum trisulfide, c-MoS_3 by hydrogen was also monitored by residual gas analysis. This reaction is similar to the second reaction in the ATTM decomposition with the exception of reaction time, temperature and preparation of the starting material. The sequence of events for this decomposition were as follows:

Prior to data acquisition - Sample placed in end of tube, Ar flow to remove air (particularly O_2), 15% H_2/He flow started, tube into 250°C tube furnace, sample at room temperature,

0 min - Data acquisition started, N_2 background very low,

20 min - Sample pushed into furnace using push rod (with O-ring seal),

140 min - Switch to Ar flow,

150 min - Tube out of furnace,

175 min - Data acquisition stopped.

From the plot of the reaction gases shown in Fig.15, it is seen that the hydrogen (M2) partial pressure decreases during the reduction of c-MoS_3 while the helium (M4) partial pressure remains constant.

Figure 15 Reaction gases used in the thermal reduction of *c*-MoS_3 at 250°C.

Figure 16 Gases generated in the thermal reduction of *c*-MoS_3 at 250°C. The background was monitored by using M28 (nitrogen).

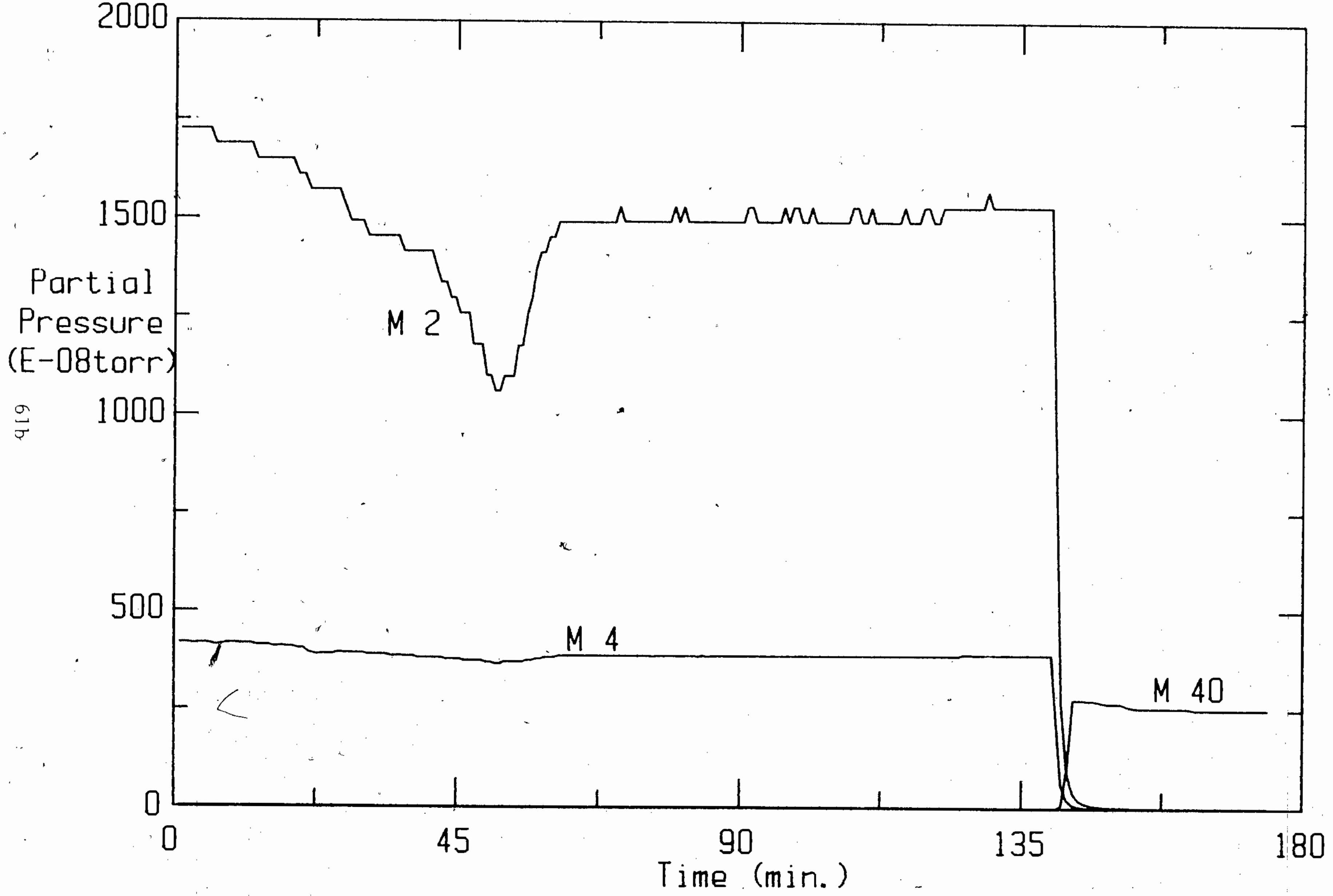
2000
1500
1000
500
0
Partial
Pressure
(E-08torr)
0
45
90
135
180
Time (min.)
M 2
M 4
M 40

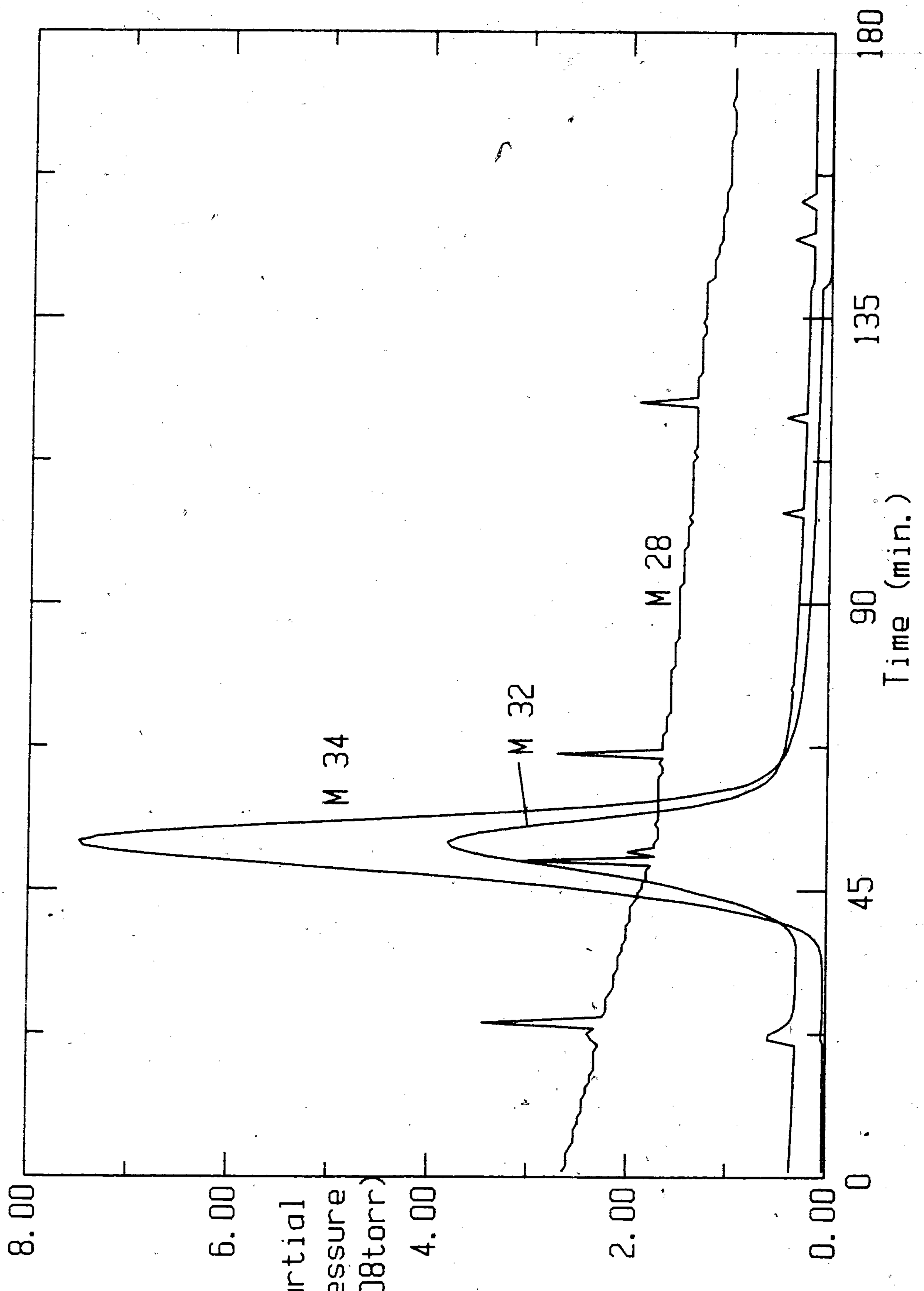
Partial Pressure (E-08torr)
8.00
6.00
4.00
2.00
0.00
Time (min.)
0
45
90
135
180
M 34
M 32
M 28

Figure 16 shows hydrogen sulfide (M34) and H_2S molecular fragment (M32) peaks generated after the sample is pushed into the tube furnace. Hydrogen sulfide (M34) was generated for a longer period (≈25 min) in this decomposition at 250°C than in the second step of the ATTM decomposition (≈7 min) at 350°C.

The first peak in the nitrogen (M28) and oxygen (M32) background partial pressures at 22 min was due to a small air contamination during the pushing of the sample into the middle of the tube furnace. This has been seen in previous runs. Nitrogen peaks without coinciding oxygen peaks are not due to air contamination but are speculated to be due to M28 fragments sporadically desorbing from the inside walls of the system.

3.2.3 RGA Summary

Reaction equations 18 and 19 generated from the residual gas analysis of thermal decomposition of ATTM and *c*-MoS_3 were as expected. It was expected that information on the actual reaction times would help to optimize the decomposition parameters. This was not the case as S/Mo ratios were found to continue to decrease after the reaction appears complete in the residual gas analysis. With closer inspection it was found that the generated gases decayed exponentially with time. Longer runs were therefore necessary to reach S/Mo≈2 .

3.3 X-ray Powder Diffraction Results

X-ray powder diffraction patterns of the compounds synthesized and of crystalline MoS_2 are presented in this section. These patterns contain structural information but could not be used for the study of phase changes during intercalation due to poor crystallinity of the samples.

Figure 17 shows the pattern of ammonium tetrathiomolybdate, $(NH_4)_2MoS_4$ synthesized by the author. This was used to confirm the identity of this material. An X-ray powder pattern calculated for ATTM agreed very well with this experimental data.(32,33) Appendix B shows the comparison.

Figure 18 is an X-ray diffraction pattern of MoS_3 prepared by chemical decomposition of ATTM. This pattern is consistent with an amorphous material.

Figure 19 shows the pattern of crystalline MoS_2 or x-MoS_2 (x denotes high crystallinity). The assignment of the Miller indices was made by comparing a calculated MoS_2(2H) pattern.(32) The MoS_2(2H) crystal structure information was collected by Wyckoff.(44)

The two step thermal decomposition of ATTM gives poorly crystalline *t*-MoS_2.(*t* denotes thermal decomposition) Figure 20 shows the diffraction pattern of *t*-MoS_2. *c*-MoS_2 (*c* denotes chemical

Figure 17 X-ray powder diffraction pattern of $(NH_4)_2MoS_4$ synthesized by the author.

Figure 18 X-ray powder diffraction pattern of *c*-MoS_3; room temperature preparation.

Figure 19 X-ray powder diffraction pattern of crystalline MoS_2. The Miller indices for the corresponding peaks are labelled.

Figure 20 X-ray powder diffraction pattern of *t*-MoS_2 prepared by thermal decomposition of $(NH_4)_2MoS_4$ at 350°C.

Figure 21 X-ray powder diffraction pattern of *c*-MoS_2 prepared by thermal decomposition of chemically produced MoS_3 at 200°C.

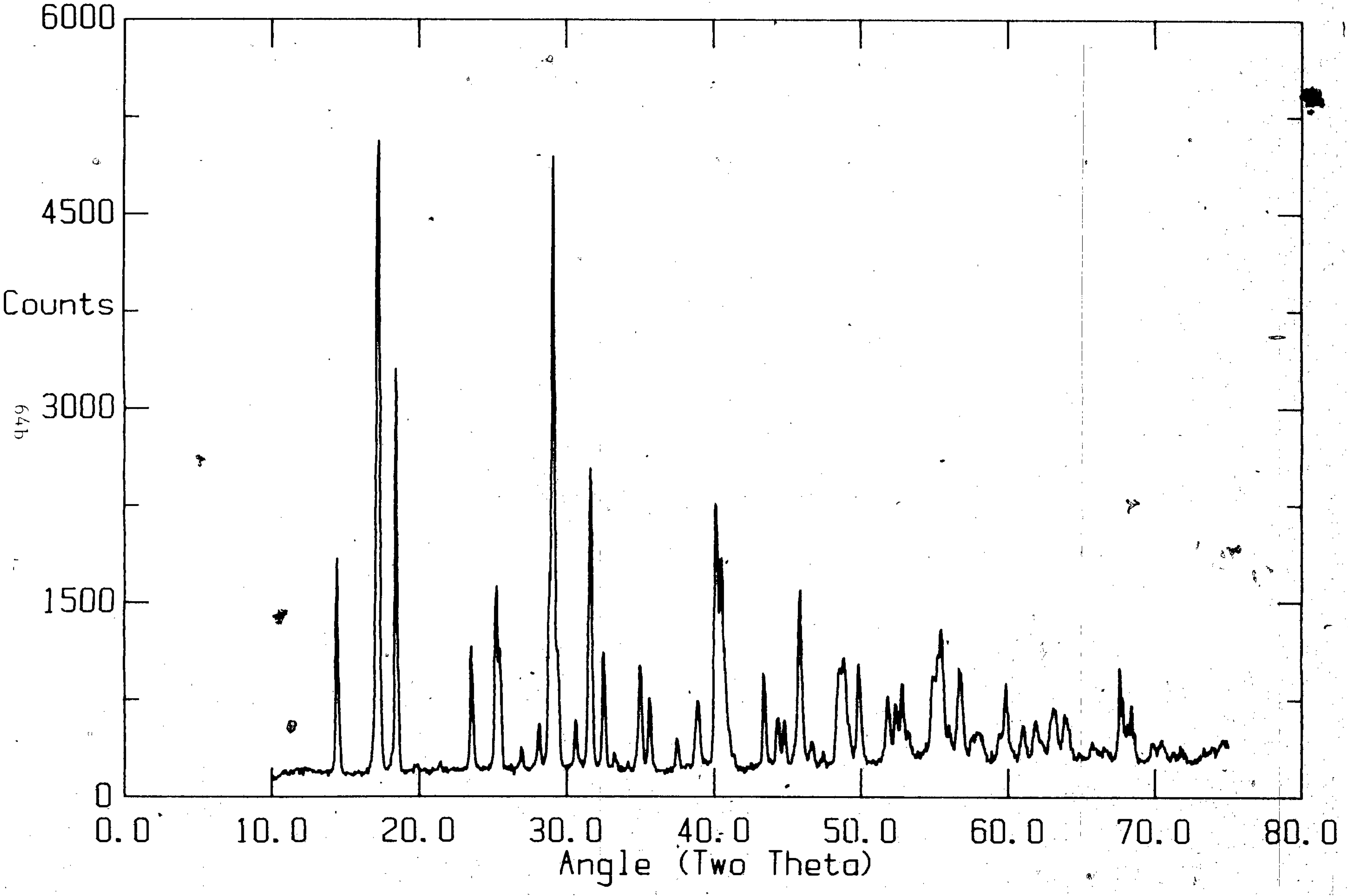
6000
4500
3000
1500
0
Counts
0.0
10.0
20.0
30.0
40.0
50.0
60.0
70.0
80.0
Angle (Two Theta)

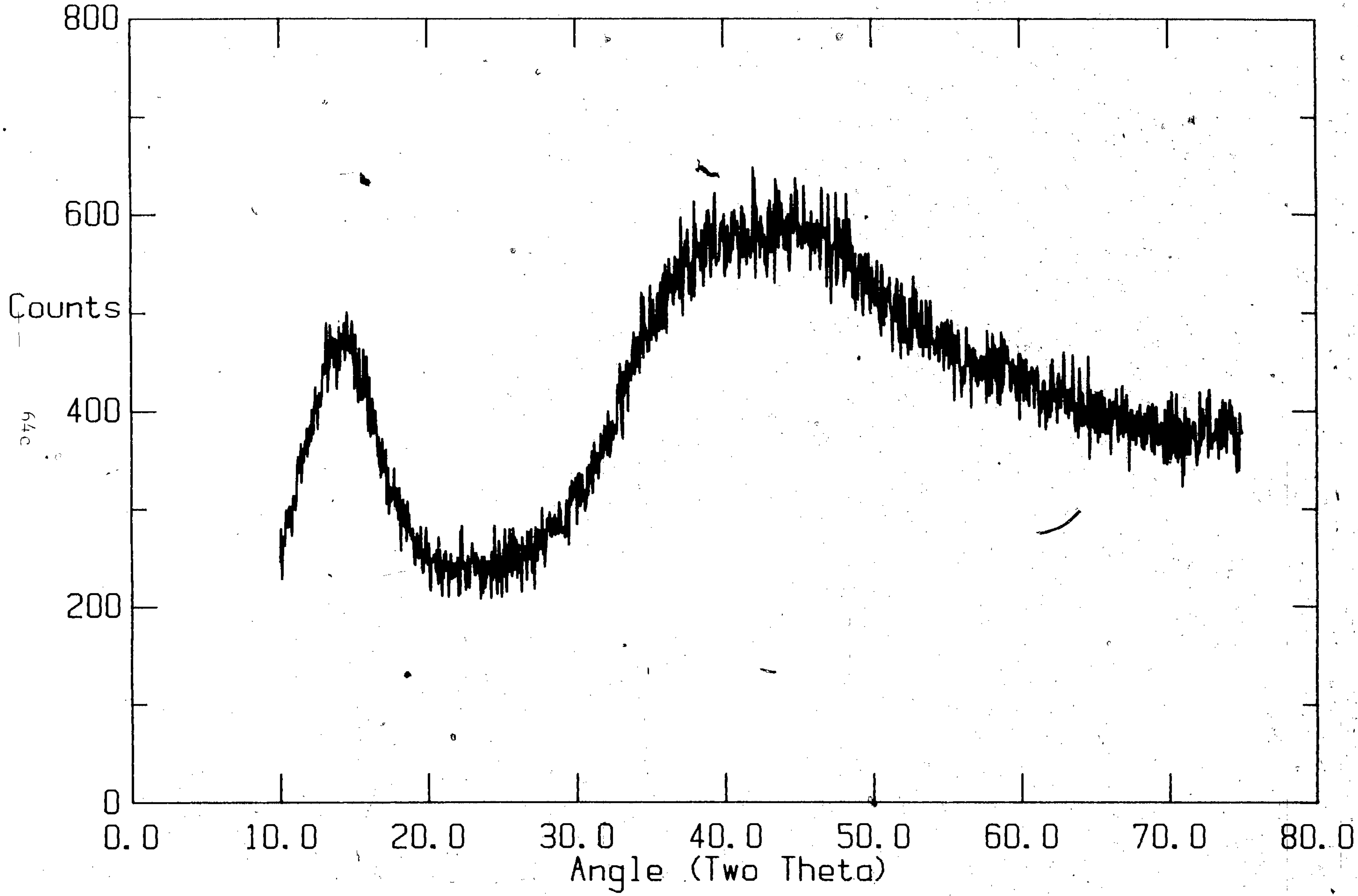
800
600
400
200
0
Counts
0.0
10.0
20.0
30.0
40.0
50.0
60.0
70.0
80.0
Angle (Two Theta)

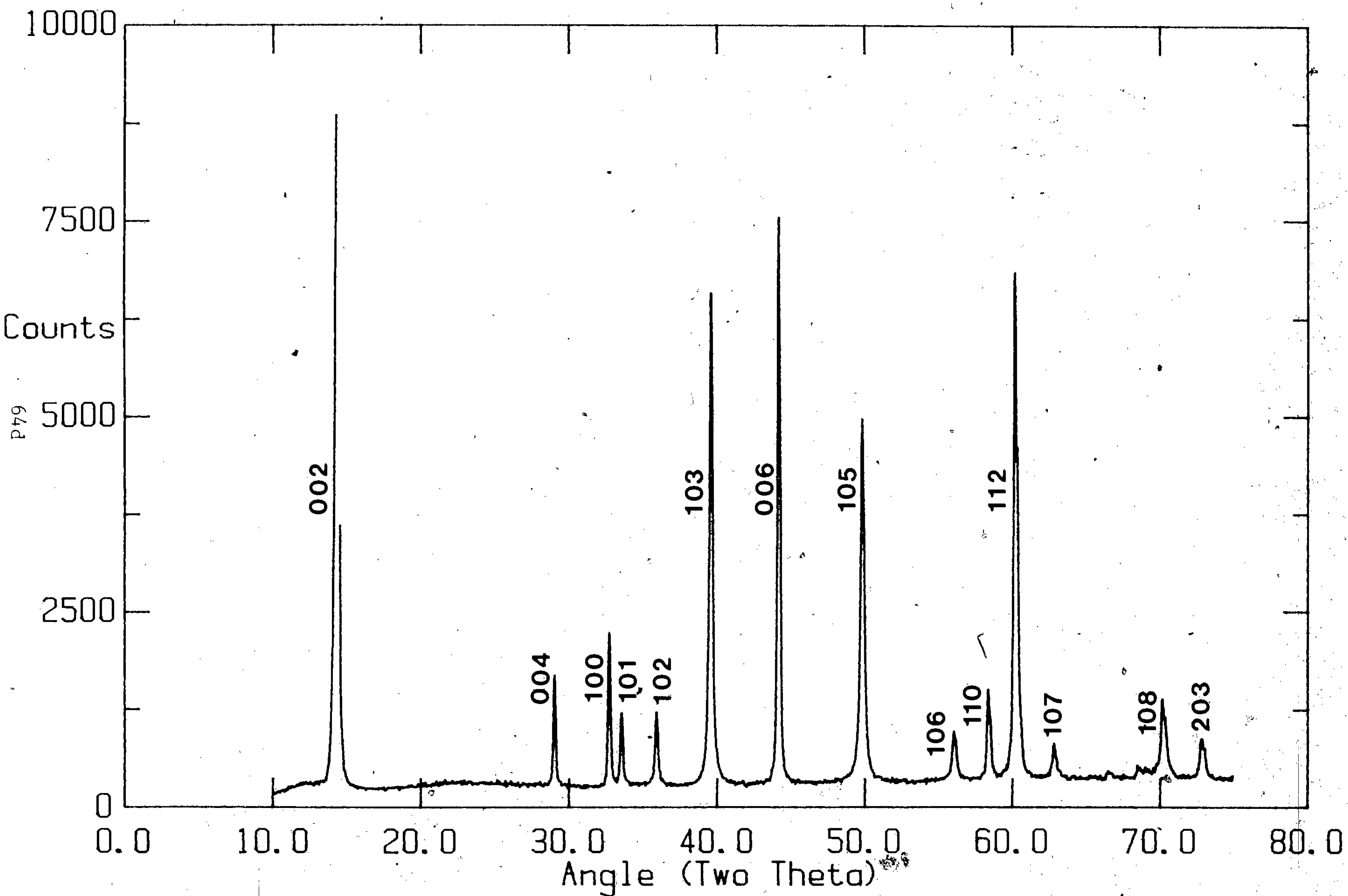
10000
7500
Counts
5000
2500
0
0.0
10.0
20.0
30.0
40.0
50.0
60.0
70.0
80.0
Angle (Two Theta)
002
004
100
101
102
103
006
105
106
110
112
107
108
203

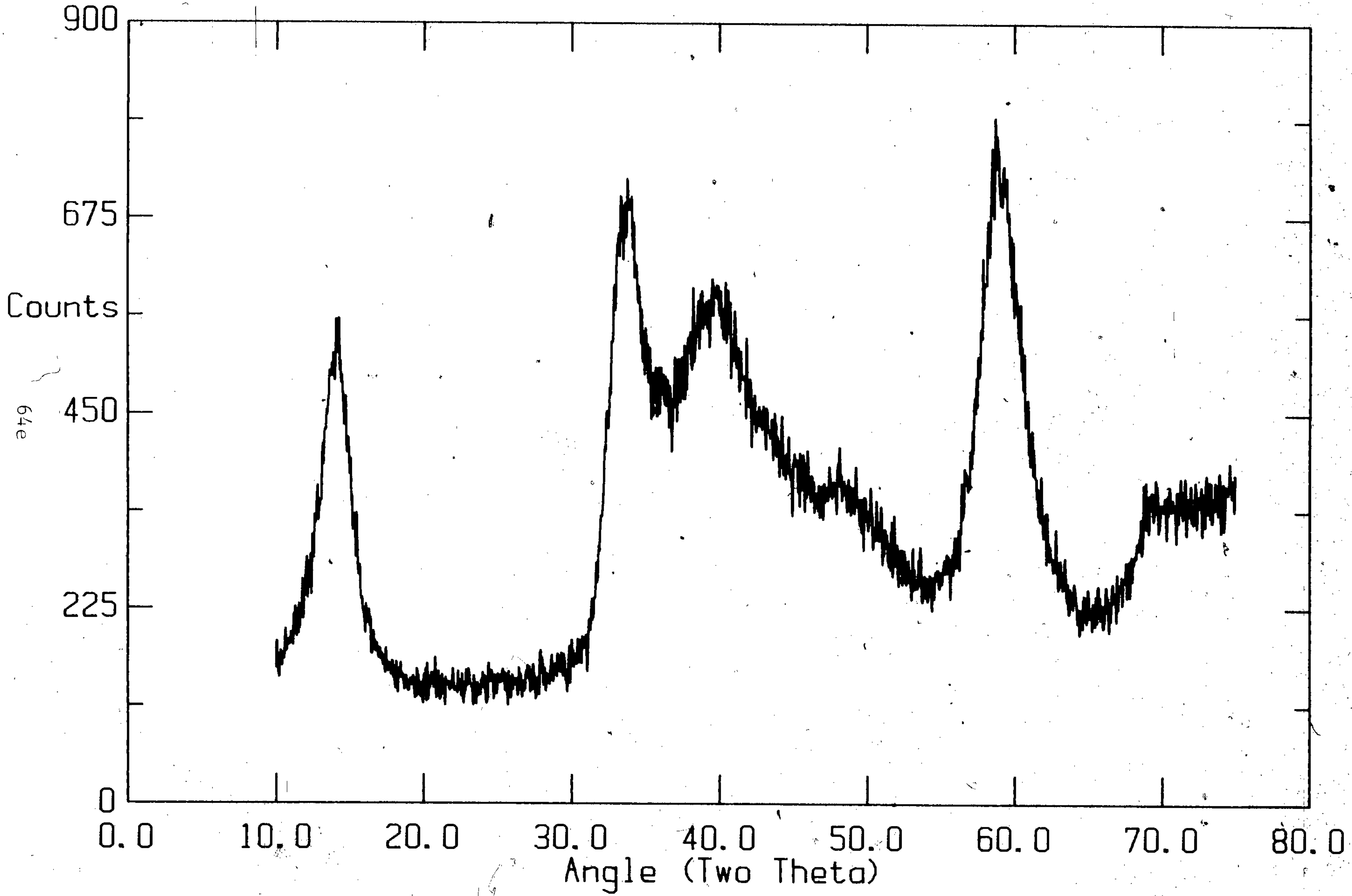
900
675
Counts
450
225
0
0.0
10.0
20.0
30.0
40.0
50.0
60.0
70.0
80.0
Angle (Two Theta)

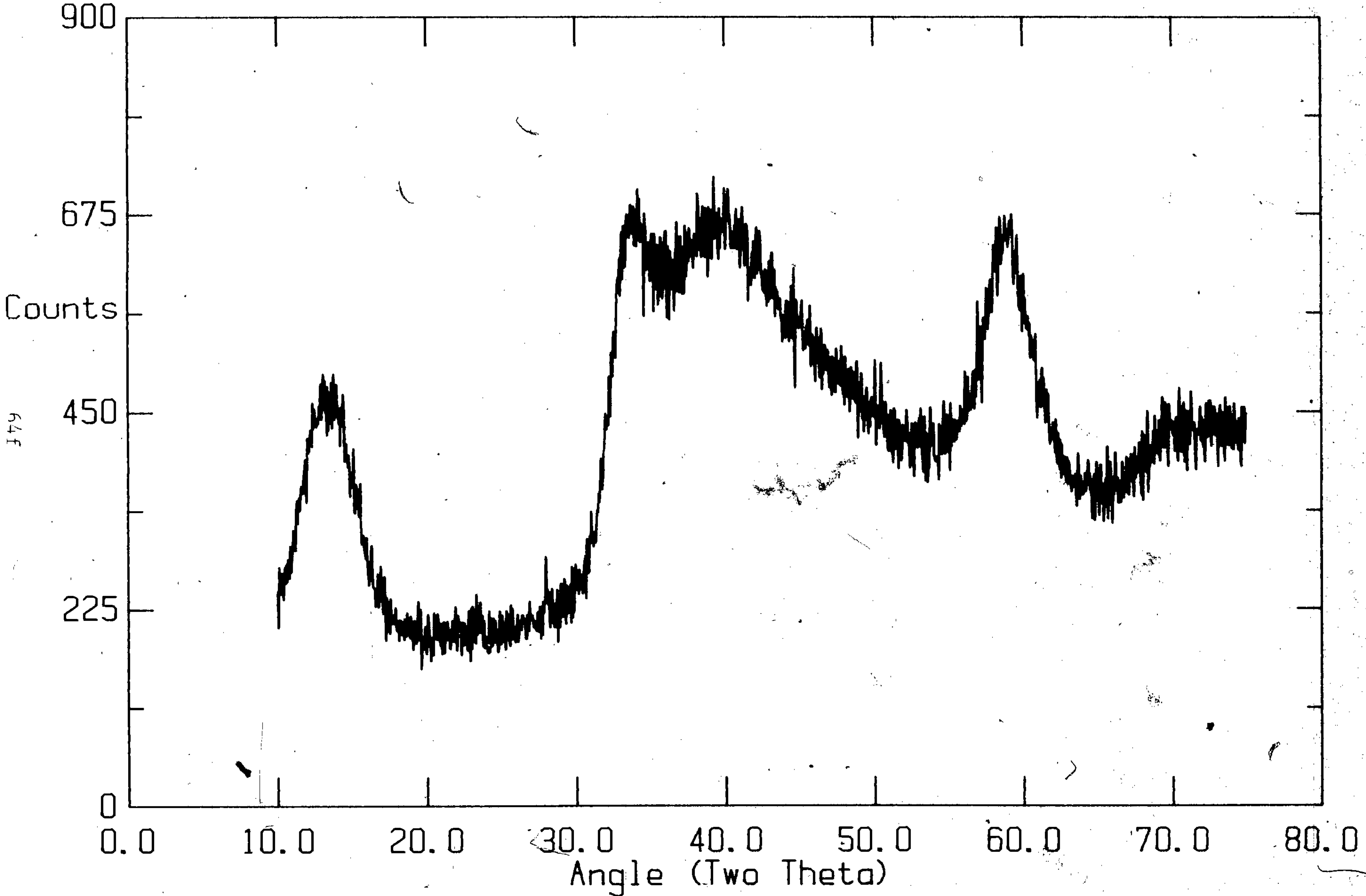
900
675
Counts
450
225
0
0.0
10.0
20.0
30.0
40.0
50.0
60.0
70.0
80.0
Angle (Two Theta)

decomposition) prepared from ATTM, which is chemically decomposed to *c*-MoS_3 and then thermally reduced, is also poorly crystalline and shown in Fig.21. Assignment of reflections, using the crystalline MoS_2 results, were made for *t*-MoS_2 and *c*-MoS_2.

Although the X-ray powder patterns for *t*-MoS_2 and *c*-MoS_2 are characteristic of poorly crystalline materials, useful information may be obtained.

The position of the (002) peak is displaced to lower angles for *t*-MoS_2 (14.2°) and *c*-MoS_2 (13.8°) from that for crystalline MoS_2 (14.5°). As shown later, this shift in the 002 peak is due to imperfect stacking in the crystals.

The width of the 002 reflection indicates that the average number of stacked layers for *t*-MoS_2 is 6 and for *c*-MoS_2 is 3 as calculated from the Scherrer formula.(29) Assuming the layers are infinite in extent, the edge planes can be neglected and the surface area depends only on the basal planes. From primitive unit cell dimensions for MoS_2(2H), the theoretical surface area, S, was calculated:

$$S = 651/n \quad (m^2/g) \qquad \text{Eq.20}$$

where n is the number of stacked sheets. Using Equation 20 the predicted surface area of *t*-MoS_2 is $108 m^2/g$ and *c*-MoS_2 is $217 m^2/g$. These predictions are greater than experimental values; for *t*-MoS_2,

$S = 30\text{-}50 m^2/g$ and for c-MoS_2, $S = 70\text{-}110 m^2/g$.

The X-ray diffraction patterns of t-MoS_2 and c-MoS_2 show that the former is more crystalline. t-MoS_2 is decomposed at a higher temperature (350°C) than c-MoS_2 (200°C) which explains the difference.

Many reflections are contained inside the broad envelope between $2\theta \approx 30°$ and $2\theta \approx 60°$. These include the (100), (101), (102), (103), (006), (105), (106), (110), and (008) reflections. The strongest are the (100), (103), and (110) with a small (105) peak in the t-MoS_2 pattern. The (100)-(103)-(105) series is very sensitive to the interlayer order.(45) As ℓ increases in the zone of (10ℓ), mixing of pure intralayer (100) with interlayer effects occurs. Important structural information such as rotational disordering about the c axis can be obtained in this region.

X-ray diffraction patterns of small crystallites of MoS_2(2H) where $n = 1$ to 4 were calculated by Liang *et al.*(45) The (103) and (105) peaks in their initial calculated patterns were more prominent than in the experimental t- and c-MoS_2 patterns. By assuming interlayer rotational disordering about the c axis, calculated patterns with less prominent (103) and (105) reflections were obtained which more closely matched the experimental data in this work.

X-ray diffraction patterns were measured for Li_1MoS_2 and Li_3MoS_2 powders to determine if any structural changes or increase in crystallinity occurred during the lithiation process. These samples were measured in an air-tight X-ray cell with a beryllium window. To remove the strong, sharp beryllium reflections and the X-ray case background from the sample patterns, a blank pattern with the X-ray case was measured and subtracted from each sample. These poorly crystalline patterns for Li_1MoS_2 and Li_3MoS_2 could not be seen without this subtraction.

The X-ray powder diffraction technique is often used to study crystalline materials with strong, sharp reflections. In those instances the few beryllium reflections are easy to identify and background subtraction becomes unnecessary.

Figures 22 and 23 show that the subtraction of the sample patterns from the X-ray case background pattern were not ideal. Sharp positive and negative peaks are seen at the angles expected for beryllium reflections. The largest Be reflections are ≈50,000 counts. With an error in intensity of $\pm\sqrt{N}$, the error in subtraction is $\pm 2\sqrt{N}$ or ≈450 counts. This large error in intensities is the source of the sharp peaks seen.

The diffraction patterns of the lithiated samples do not have any strong reflections at angles other than those of a Be pattern. The crystallinity of both lithiated samples decreases compared to the *c*-MoS_2 starting material. This is explained by the increased disorder of the lattice due to the co-intercalation of lithium and ammonia.

Figure 22 X-ray powder diffraction pattern of Li_nMoS_2 using background subtraction of the beryllium window X-ray case.

Figure 23 X-ray powder diffraction pattern of Li_3MoS_2 using background subtraction of the beryllium window X-ray case.

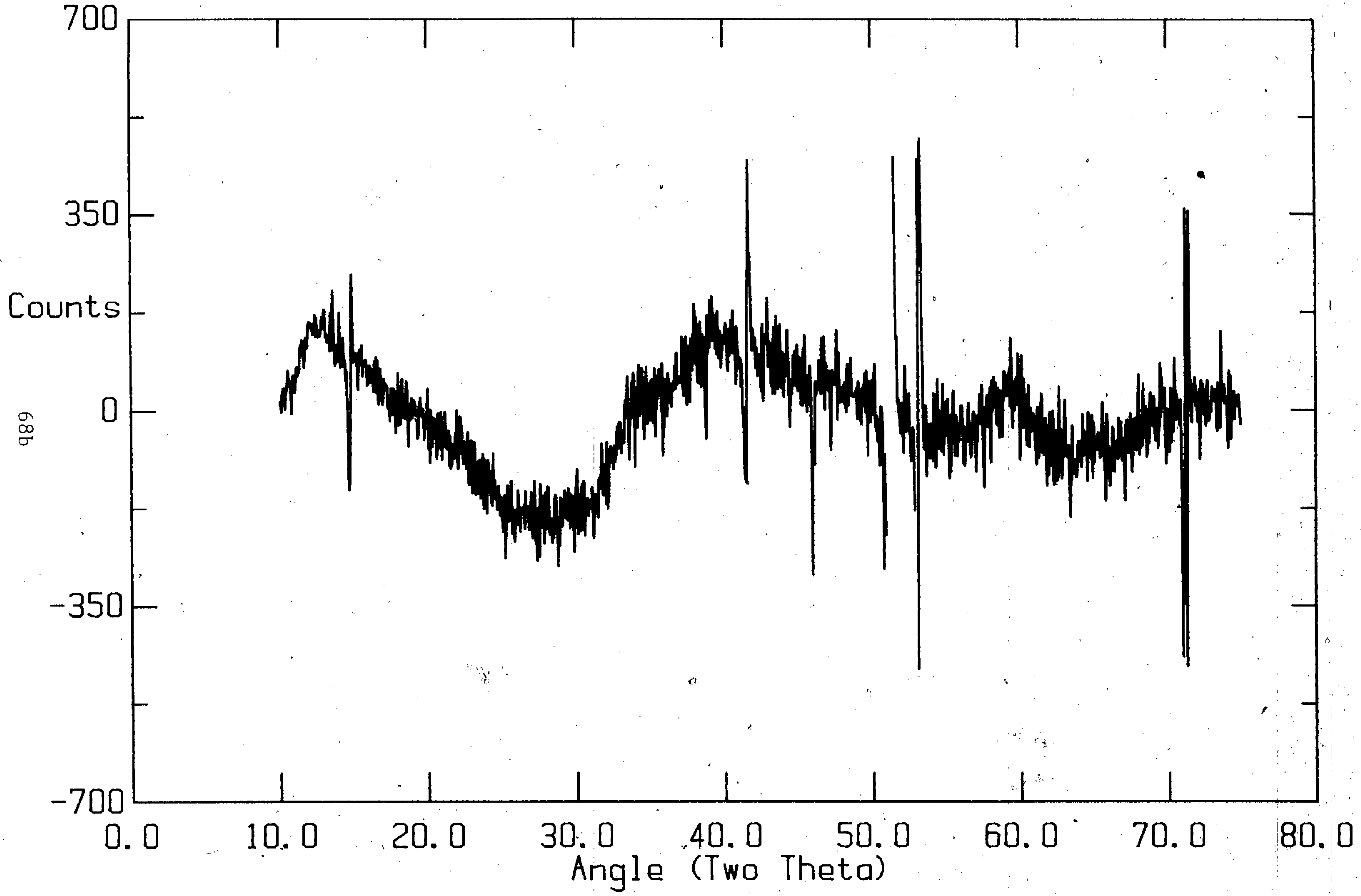
700
350
0
-350
-700
Counts
0.0
10.0
20.0
30.0
40.0
50.0
60.0
70.0
80.0
Angle (Two Theta)

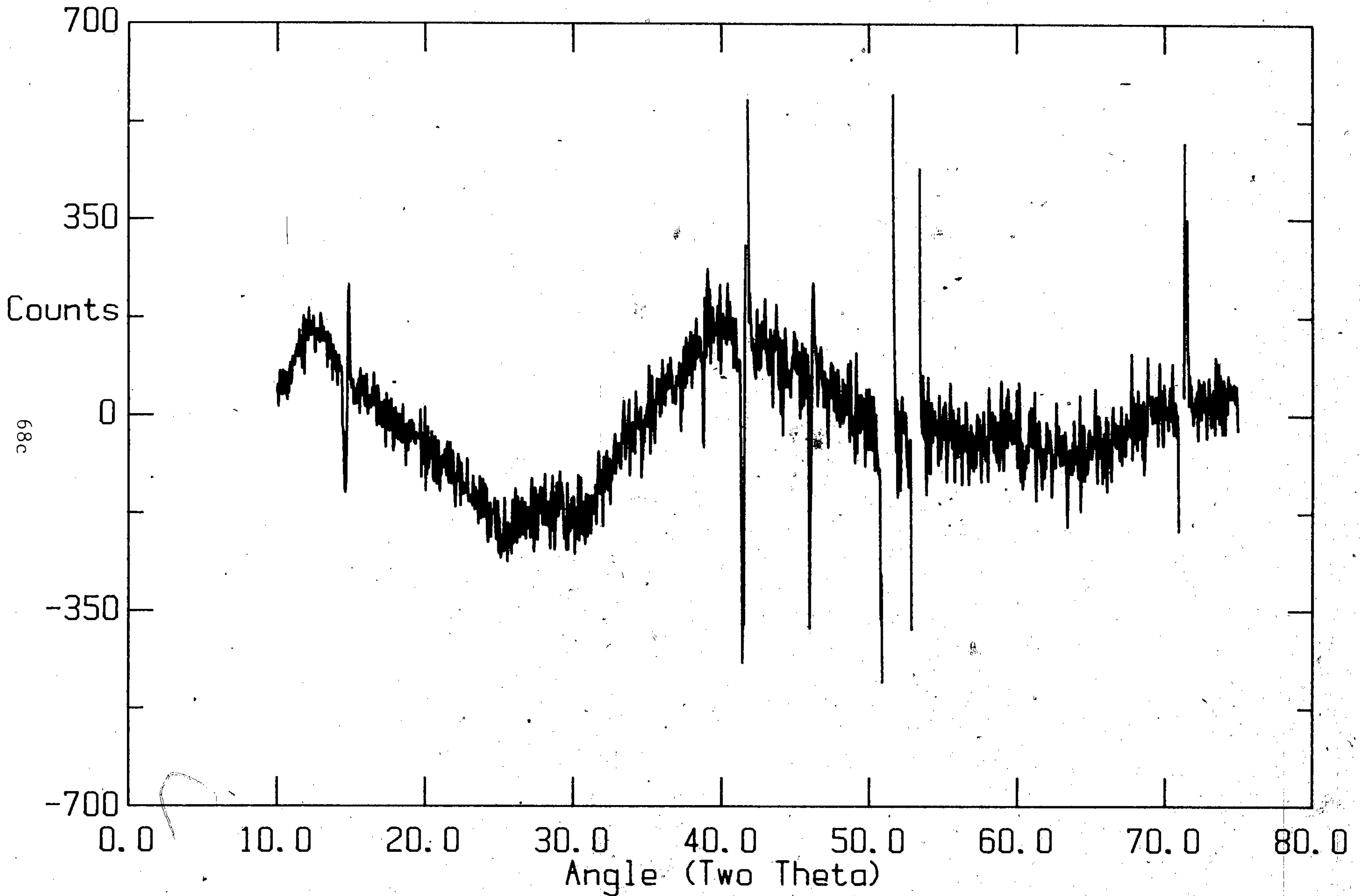
700
350
Counts
0
-350
-700
0.0
10.0
20.0
30.0
40.0
50.0
60.0
70.0
80.0
Angle (Two Theta)

3.4 Thermal Gravimetric Analysis Results

Two examples of the oxidation of molybdenum disulfide to molybdenum trioxide are shown in Fig.24. The powders were heated at 25°C/min to 550°C followed by a 20 min isothermal period under an air atmosphere.

The high purity MoS_2 standard(Intermagnetics General Corp.) had a weight loss of 10.00% corresponding to an S/Mo ratio of 2.00. Sample IIIP100 had a weight loss of 14.35% corresponding to an S/Mo ratio of 2.26.

Samples of molybdenum disulfide from the two step thermal decomposition and the chemical / thermal decomposition, a high purity crystalline sample and sulfur(Fisher) were heated at 20°C/min to 500°C under a helium amosphere. These runs shown in Fig.25 were used to ensure that the prepared molybdenum disulfides were discrete compounds and not mixtures of MoS_2 and sulfur.

Thermal gravimetric analysis was also used to check the composition of synthesized $(NH_4)_2MoS_4$. ATTM was heated to 550°C under a helium atmosphere and is shown in Fig.26. A sharp weight loss of 26.0% corresponding to the decomposition of $(NH_4)_2MoS_4$ to MoS_3 occurred between 150 and 220°C. This value is in agreement with the theoretical value of 26.2% calculated from Equation 18.

Figure 24 Oxidation of MoS_2 to MoO_3 under an air atmosphere. Temperature ramped at 25°C/min. to 550°C(actual $T_f=530°C$), followed by a 20 min. isothermal period.

x-MoS_2 = low surface area, crystalline MoS_2 : S/Mo=2.00,
c-MoS_2 = chemically/thermally reduced MoS_2 : S/Mo=2.26.

Figure 25 Thermal stability experiments under a helium atmosphere. Temperature ramped at 20°C/min to 500°C(actual $T_f=490°C$).

x-MoS_2 = low surface area, crystalline MoS_2,
c-MoS_2 = chemically/thermally reduced MoS_2,
t-MoS_2 = thermally decomposed MoS_2,
Sulfur was included for comparison.

Figure 26 Thermal decomposition of $(NH_4)_2MoS_4$(synthesized by the author) under a helium atmosphere. Temperature ramped at 20°C/min. to 550°C(actual $T_f=530°C$). The plateau compositions are labelled.

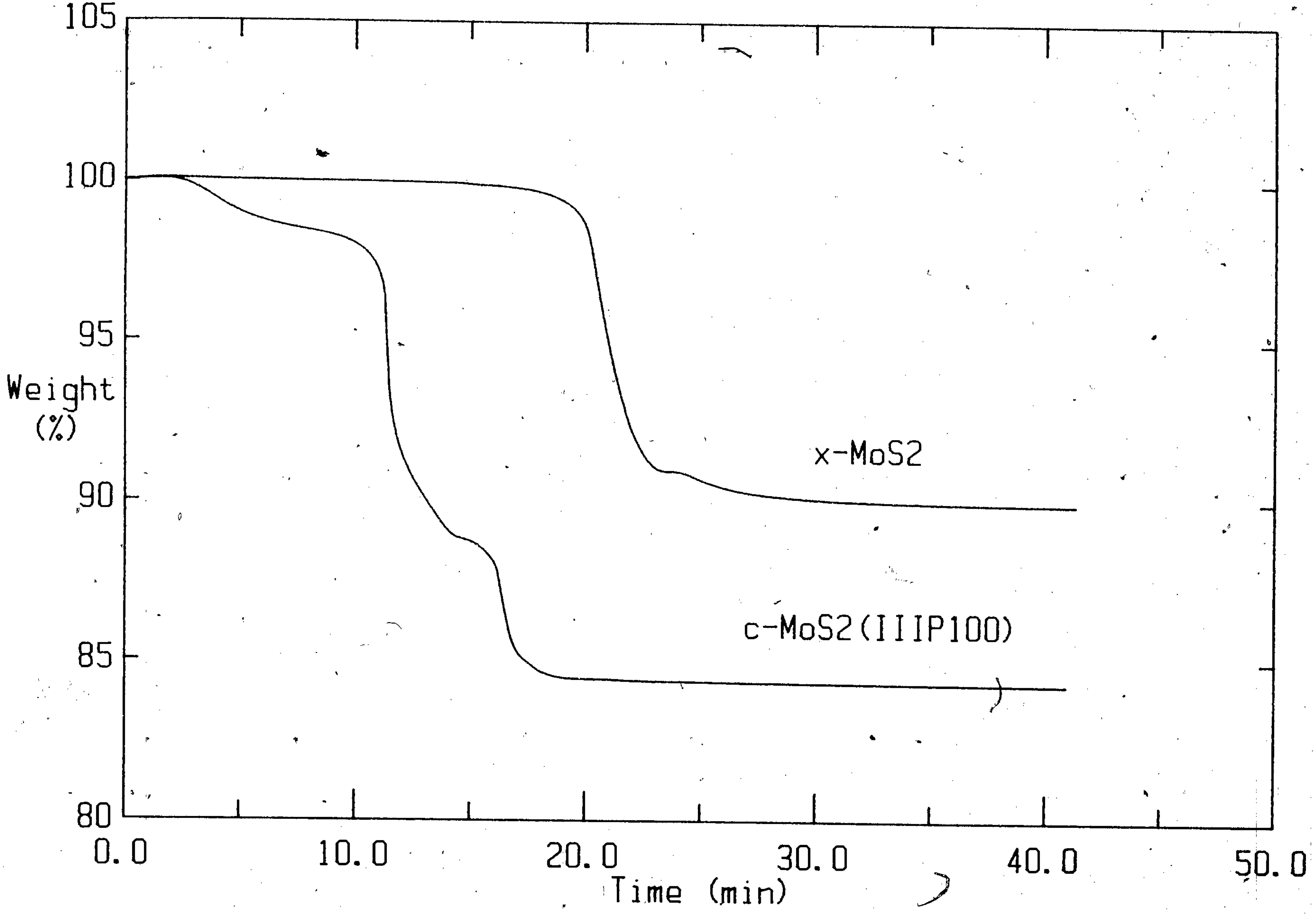
105
100
95
90
85
80
Weight
(%)
0.0
10.0
20.0
30.0
40.0
50.0
Time (min)
x-MoS2
c-MoS2(IIIP100)

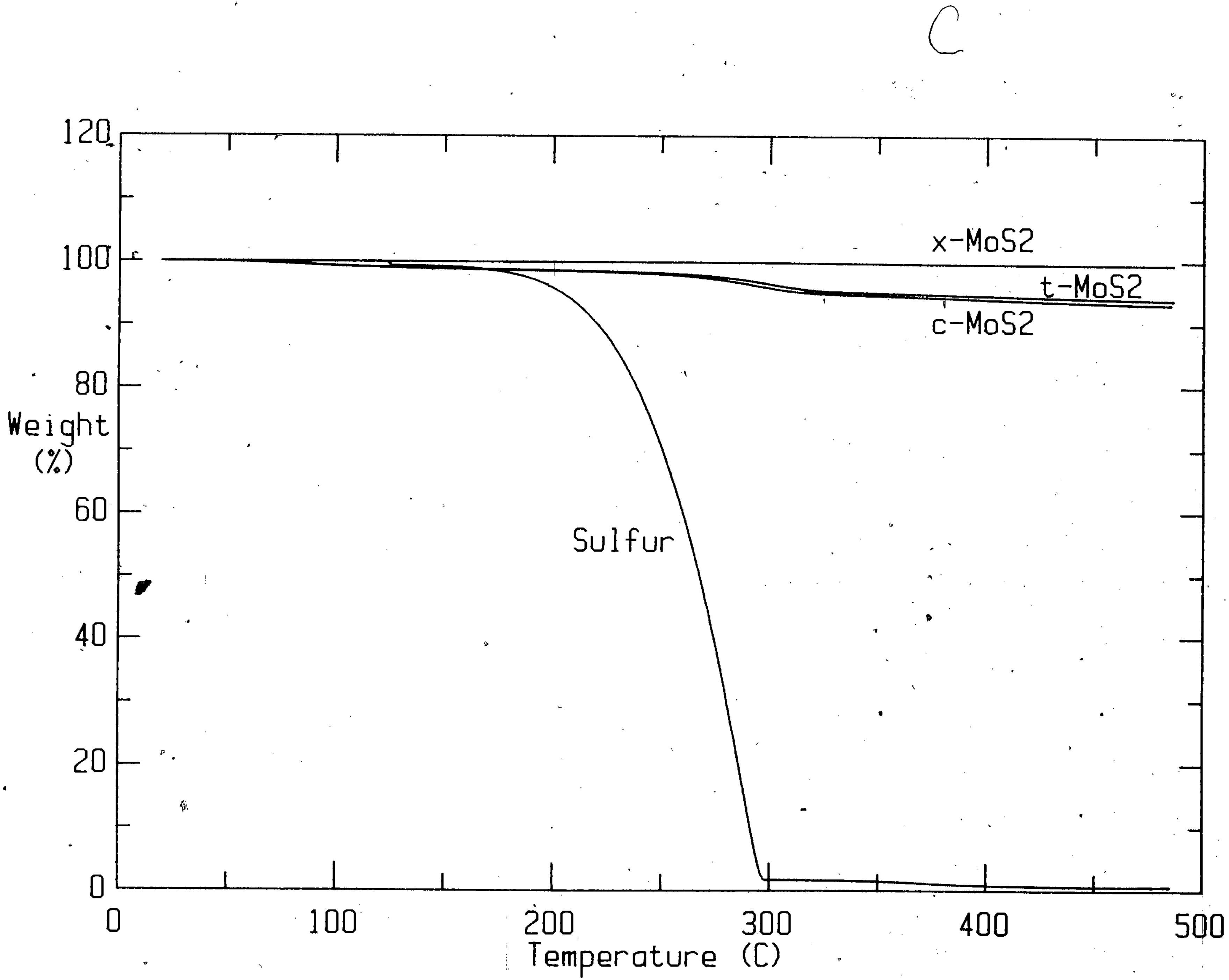
C
x-MoS2
t-MoS2
c-MoS2
Sulfur
Weight (%)
120
100
80
60
40
20
0
Temperature (C)
0
100
200
300
400
500

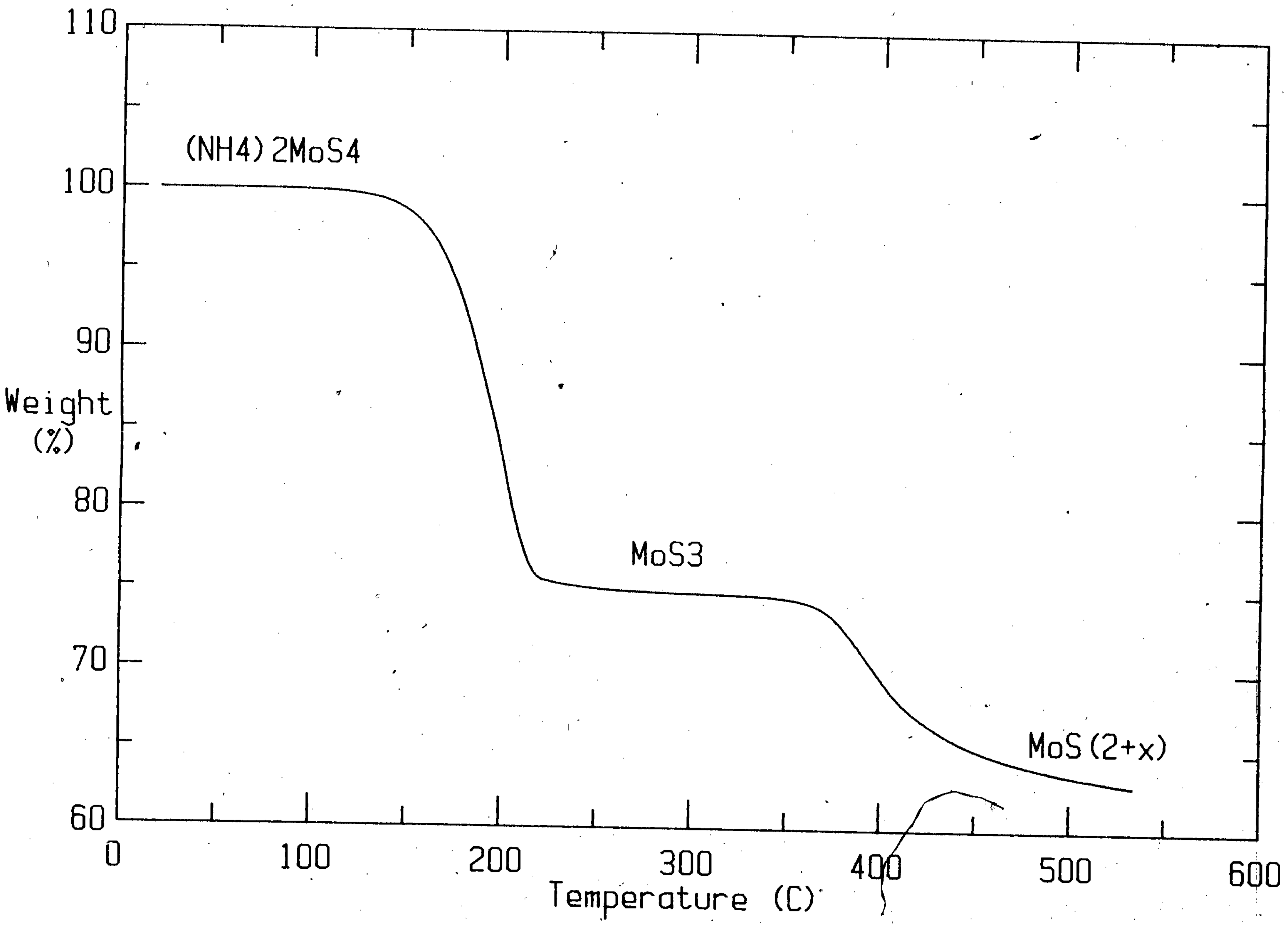
110
100
90
80
70
60
Weight (%)
0
100
200
300
400
500
600
Temperature (C)
(NH4) 2MoS4
MoS3
MoS (2+x)

3.5 **Electrochemical Characterization**

3.5.1 Introduction

In this section we compare the electrochemical properties of high and low surface area MoS_2, the latter used in commercial lithium batteries.(2) In this study it is important to know the cathode potential, with respect to lithium metal, for all values of *x* in high surface area Li_xMoS_2. With this data it is possible to correlate the solvent reactivity at a particular value of *x* value in Li_xMoS_2 with a solvent reduction potential.

3.5.2 Low Surface Area MoS_2

Crystalline or low surface area MoS_2 has been studied in Li/Li_xMoS_2 electrochemical cells by Py and Haering.(4) As lithium is intercalated into Li_xMoS_2 $(0.1 < x < 1)$ the structure changes from the α-phase (2H polytype; trigonal prismatic) to a β-phase (1T polytype; octahedral Mo co-ordination). Electrons from the lithium are inserted in the π^* conduction band of the semi-conducting α-MoS_2 to $Li_{0.1}MoS_2$. Due to the large band gap (≈1eV) between π and π^* in α-MoS_2, phase transformation to conducting β-MoS_2 with no energy band gap begins at $Li_{0.1}MoS_2$ and concludes at $Li_{1.0}MoS_2$.

A third phase, known as γ-phase, was studied by Selwyn *et al.*(46) γ-phase is formed if intercalation continues $(x > 1)$ and was found to be a mixture of molybdenum metal and lithium sulfide using X-ray diffraction on Li/Li_xMoS_2 electrochemical cells.

Electrochemical data from a research cell containing low surface area MoS_2 is shown in Fig.27 and 28. Figure 27 shows the voltage curves V(x) for the first discharge (D1) and recharge (R1) and second discharge (D2). Figure 28 shows $|(\partial x/\partial V)|_T$ versus V, better illustrating the plateaus in the V(x) curves. These plateaus are caused by the phase changes described above. In the first discharge there is a plateau at about 1.0V corresponding to the $\alpha \rightarrow \beta$ transition and a plateau at 0.55V corresponding to the $\beta \rightarrow \gamma$ transition. At the end of the first discharge, $x = 3.92$ based on total charge, compared to a theoretical value of 4 from the equation:

$$4Li + MoS_2 \longrightarrow 2Li_2S + Mo \qquad \text{Eq. 21}$$

According to Selwyn *et al*, the reaction during γ-phase cycling is:

$$Mo + 2Li_2S \longleftrightarrow 4Li + (Mo,2S) \qquad \text{Eq. 22}$$

where (Mo,2S) is a mixture of molybdenum metal and sulfur particles or some compound(s) of Mo and S. Assuming γ-phase is a mixture of particles, the theoretical electrochemical cell potential is:

$$V = \frac{-1}{2Fe}\left[\Delta G(Li_2S) - \Delta G(S) - 2\Delta G(Li)\right] \qquad \text{Eq. 23}$$

Figure 27 Voltage versus intercalated lithium is plotted for a low surface area molybdenum disulfide experimental cell. First discharge (D1) to 0.1V, first recharge (R1) to 2.8V and second discharge (D2) to 0.7V.

Constant current = C/20 rate or 0.90mA.
Cathode weight = 107 mg.
Temperature = 21°C.
Electrolyte : 1M $LiAsF_6$/PC.

Figure 28 Derivative plot for Figure 27. $|(\partial x/\partial V)|_T$ is plotted versus voltage, V for the first discharge and recharge and the second discharge.

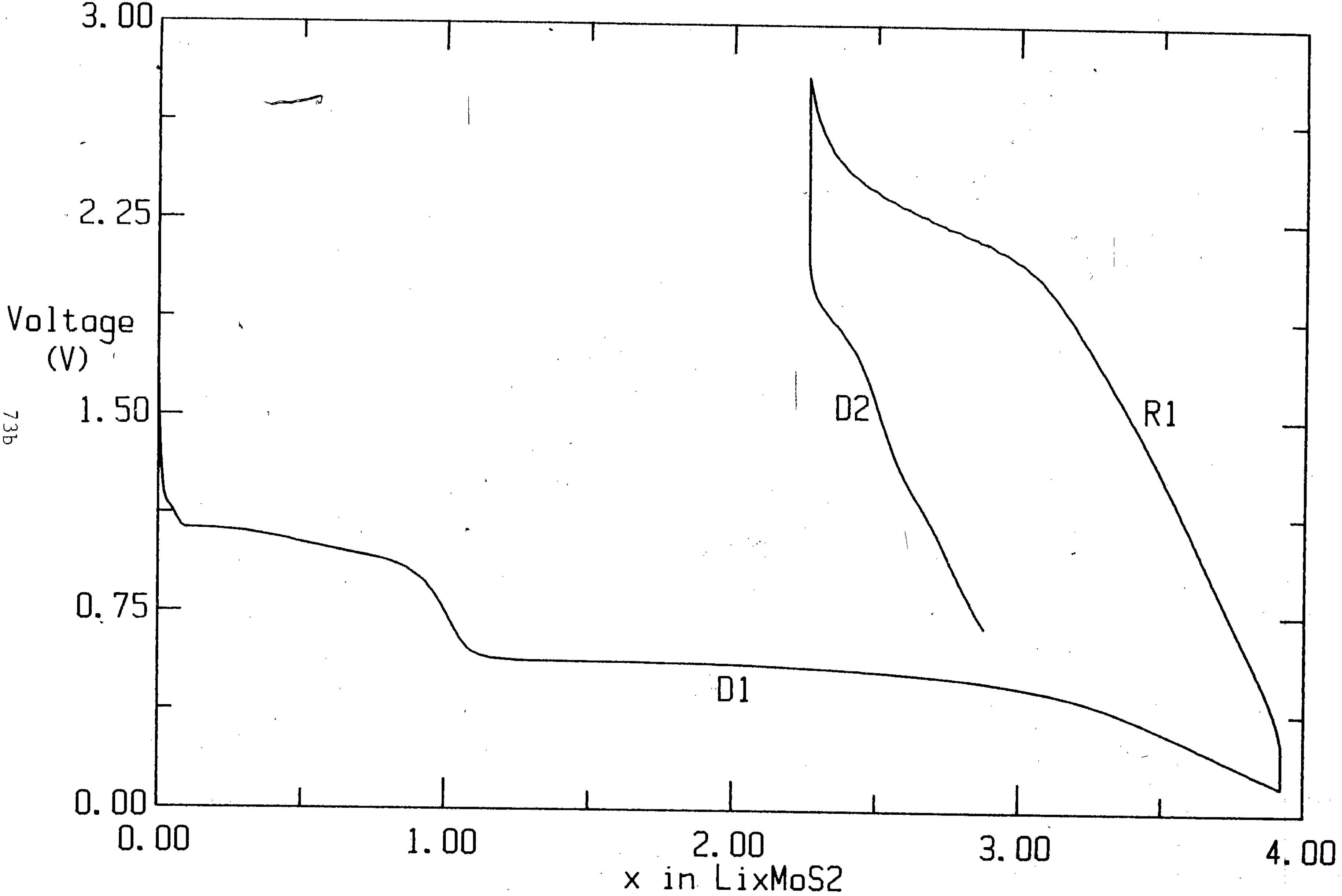
3.00
2.25
1.50
0.75
0.00
Voltage
(V)
0.00
1.00
2.00
3.00
4.00
x in LixMoS2
D1
D2
R1

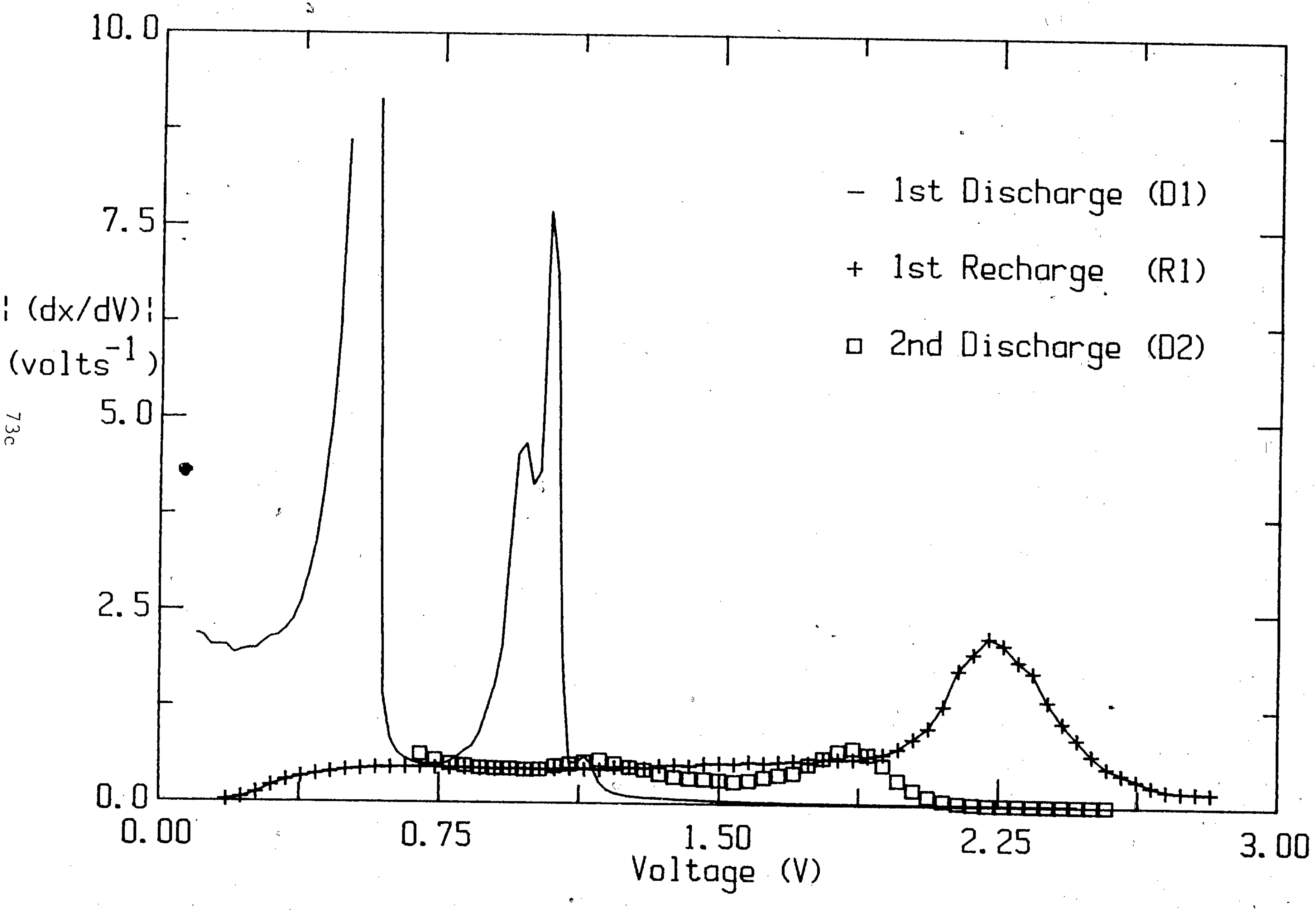

10.0
7.5
5.0
2.5
0.0
| (dx/dV) |
(volts^{-1})
0.00
0.75
1.50
2.25
3.00
Voltage (V)
– 1st Discharge (D1)
+ 1st Recharge (R1)
□ 2nd Discharge (D2)

where -e is the charge on an electron and ΔG is the free energy of formation at constant temperature. The predicted potential of $V = 2.18V$ agrees with the single voltage plateau of 2.2V observed in the first recharge of the γ-phase material.

3.5.3 High Surface Area MoS_2

Limited electrochemical data was found in the literature for poorly crystalline or high surface area MoS_2. Results were obtained for MoS_2 prepared by low temperature nonaqueous precipitation from molybdenum tetrachloride, $MoCl_4$ and hexamethyldisilathiane, HMDST(18) or $MoCl_4$ and lithium sulfide, Li_2S.(47,48)

Poorly crystalline MoS_2, prepared by Auborn *et al* from $MoCl_4$ and HMDST, was mixed with 20% carbon to improve the initial conductivity of the cathodes in the test cells. On the first discharge, the voltage curve gradually declined for $x \rightarrow 1$ with an average voltage of 1.9V, then dropped off sharply to a 1.2V cutoff, where $x = 2.3$. The subsequent recharge to 2.8V and discharge reversibly cycled $\Delta x = 1.5$.

Jacobson *et al* (47) prepared poorly crystalline MoS_2 from $MoCl_4$ + Li_2S. A series of samples with increasing crystallinity were made by heating this material to progressively higher temperatures. Li/MoS_2 cells were made using these samples and the voltage curves $V(x)$ were measured. MoS_2 heat treated at 150 and 275°C intercalated lithium to $x = 0.83$ and 1.12 respectively, using a 1.4V cut-off. The voltage plateaus were approximately 1.7 and 1.8V for the 150 and 275°C MoS_2 cathodes. The cell heat treated at 150°C was observed to reversibly cycle between 1.40 and 2.72V for 244 cycles until the discharge capacity dropped to 50% of the second discharge.

Electrochemical cells using high surface area MoS_2, prepared from a chemical / thermal decomposition described previously, were cycled over wide voltage limits in an attempt to characterize this material. In Fig.29 a sloping first discharge was observed with three gradually declining plateaus separated by regions of sharper voltage drop. These weak plateaus appeared at 1.2, 0.8 and 0.4V, as shown in Fig.30. Lithium intercalated into this MoS_2 to $x = 3.06$ with a 0.1V cut-off.

Close examination of the first discharge reveals a plateau similar to the $\alpha \rightarrow \beta$ phase transition in the crystalline MoS_2 cells. This first plateau in the high surface area MoS_2 cell has a greater slope and higher voltage than low surface area MoS_2 but the length of $x = 1$ is similar. The voltage profile for $x > 1$ is significantly different. Cycling studies, between 0.7 and 2.8V, to study the reversibility of these cells were still in progress at the time of this writing. The cycling data in Fig.31 shows some reversibility. The subsequent recharge and discharge voltage plateaus at 2.2V (R1), and 1.85 and 1.2V (D2) are similar to crystalline MoS_2 cycling in β-phase.

Without X-ray diffraction patterns it is not possible to predict the cycling mechanisms for high surface area MoS_2. Data was however, obtained which correlated x in Li_xMoS_2 to the cell potential with

Figure 29 Voltage versus intercalated lithium is plotted for a high surface area molybdenum disulfide experimental cell. First discharge (D1) to 0.1V, first recharge (R1) to 2.8V and second discharge (D2) to 0.7V.

Constant current = C/20 rate or 0.38mA.
Cathode weight = 45mg.
Temperature = 21°C.
Electrolyte : 1M $LiAsF_6$/PC.

Figure 30 Derivative plot for Figure 29. $|(\partial x/\partial V)|_T$ is plotted versus voltage, V for the first discharge and recharge and the second discharge.

Figure 31 Capacity cycle life plot for a lithium high surface area molybdenum disulfide experimental cell. Δx for discharge and recharge are plotted versus cycle number.

Voltage limits : 0.7 → 2.8V.
Other parameters similar to Figure 29.

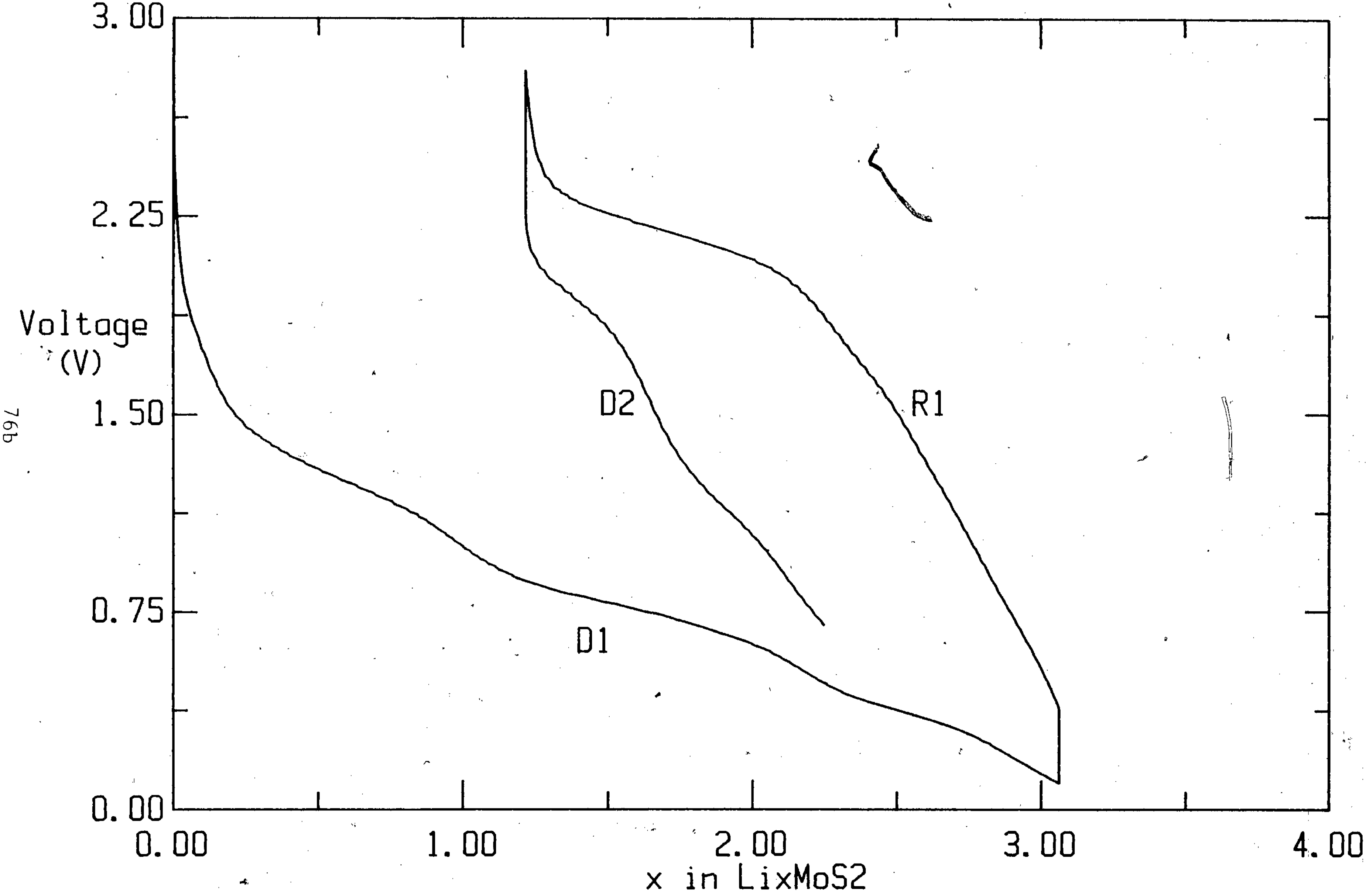
3.00
2.25
1.50
0.75
0.00
Voltage
(V)
0.00
1.00
2.00
3.00
4.00
x in LixMoS2
R1
D2
D1

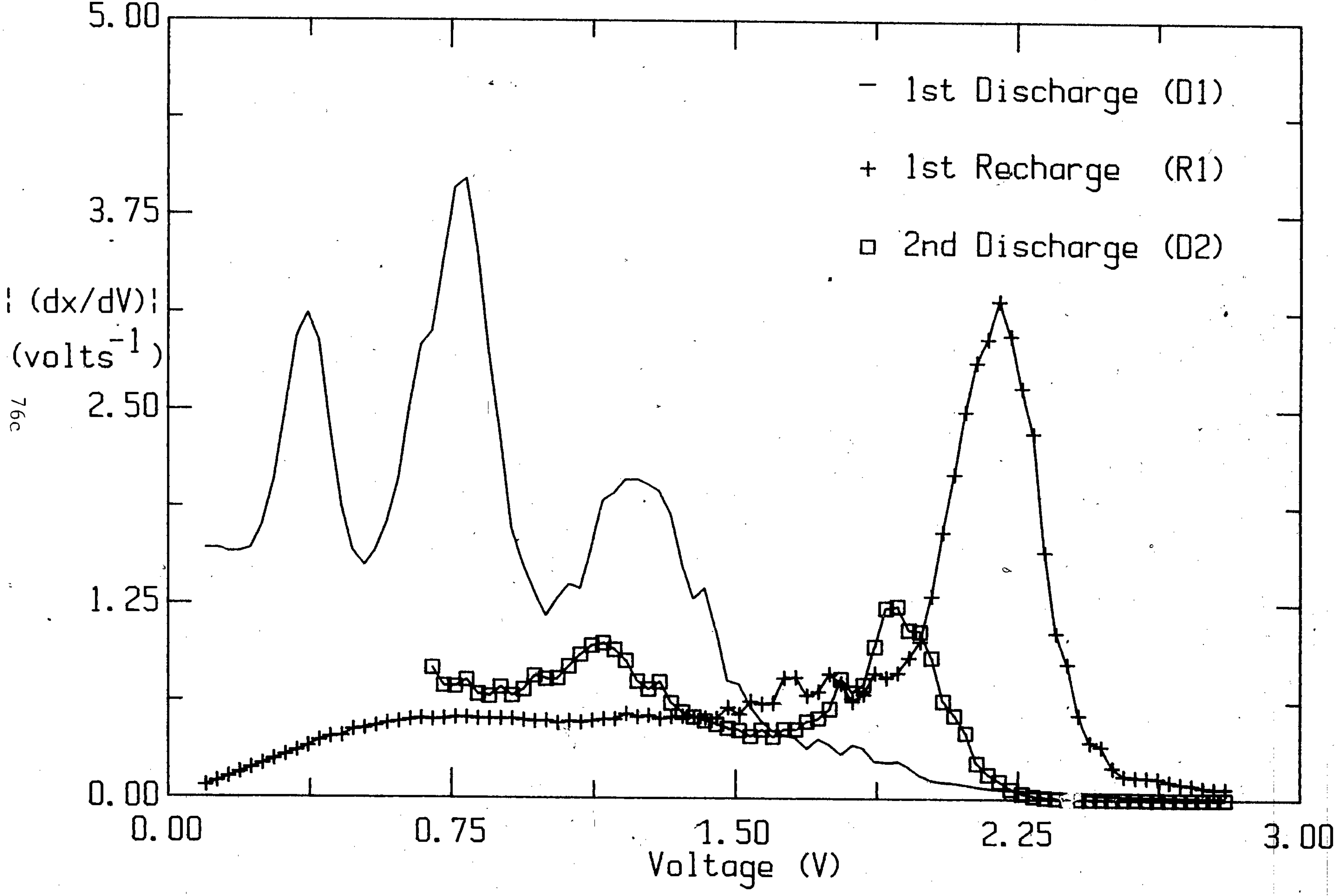

5.00
3.75
2.50
1.25
0.00
| (dx/dV)|
(volts^{-1})
0.00
0.75
1.50
2.25
3.00
Voltage (V)
— 1st Discharge (D1)
+ 1st Recharge (R1)
□ 2nd Discharge (D2)

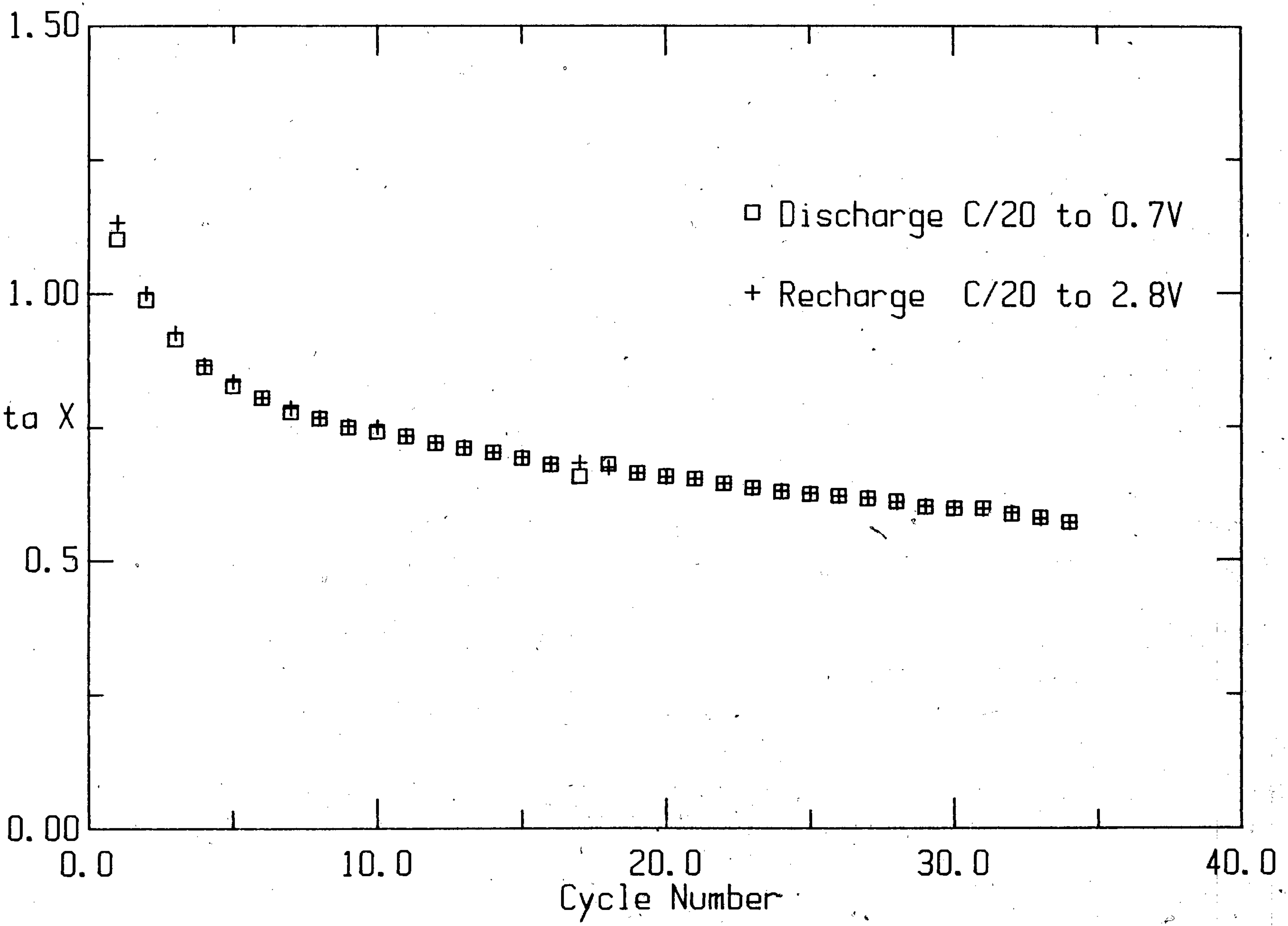
□ Discharge C/20 to 0.7V
+ Recharge C/20 to 2.8V
Delta X
1.50
1.00
0.5
0.00
0.0
10.0
20.0
30.0
40.0
Cycle Number

respect to lithium metal. This data may be useful when combined with the results of the ^{13}C-NMR solvent reactivity study in the next section.

3.5.4 Gas Evolution Results

An experimental cell containing 1M $LiAsF_6$/THF electrolyte between lithium and high surface area MoS_2 electrodes was prepared. The cell was discharged at a C/10 rate or 0.67mA for 30 hours. The gas evolution was monitored at room temperature. No gas was evolved during the first discharge to $x=3$ for Li_xMoS_2.

Tetrahydrofuran does not produce gaseous decomposition products by catalysis with Li_xMoS_2 at room temperature. Any liquid, polymer or solid decomposition products were not detectable in this experiment.

3.6 ^{13}C-NMR Results

3.6.1 Introduction and Preliminary Results

Static NMR samples were prepared to determine to what extent tetrahydrofuran, THF would adsorb onto the surface of molybdenum disulfide powders. Line widths and signal-to-noise ratios of the adsorbed THF spectra were examined. These tests used large, static (12mm O.D.) samples as they contained up to 10 times the number of moles of adsorbate as the Magic Angle Spinning (MAS)(5mm O.D.) samples. Various pre-treatments of H_2 and/or O_2 on MoS_2 were tested. Our results showed THF to adsorb to the MoS_2 surface and provide a strong ^{13}C-NMR signal-to-noise ratio.

An experiment to determine optimum cross polarization or contact times was then performed. Fig.32 shows the relative peak heights of the C_1-C_4 and C_2-C_3 carbons of THF versus the time of contact between the ^{13}C and ^{1}H spins. In an ideal situation an optimum contact time, t, is reached, after which the extra contact leads to the exponential decay of the ^{13}C magnetization, Mc. This decay is equal to $\exp(-t/T_{1\rho})$ where $T_{1\rho}$ is the rotating frame relaxation time. From Fig.32, the optimum contact time for ^{1}H-^{13}C cross-polarization experiments on MoS_2/THF samples was found to be $\approx 2000\mu S$.

This ^{1}H-^{13}C cross-polarization experiment also provides information as to the nature of the solvent-surface interaction. The

Figure 32 Plot of ^{13}C-NMR peak heights vs contact times for the sample of 5.25 μmole/m^2 of THF on H_2 treated MoS_2. CP/static.

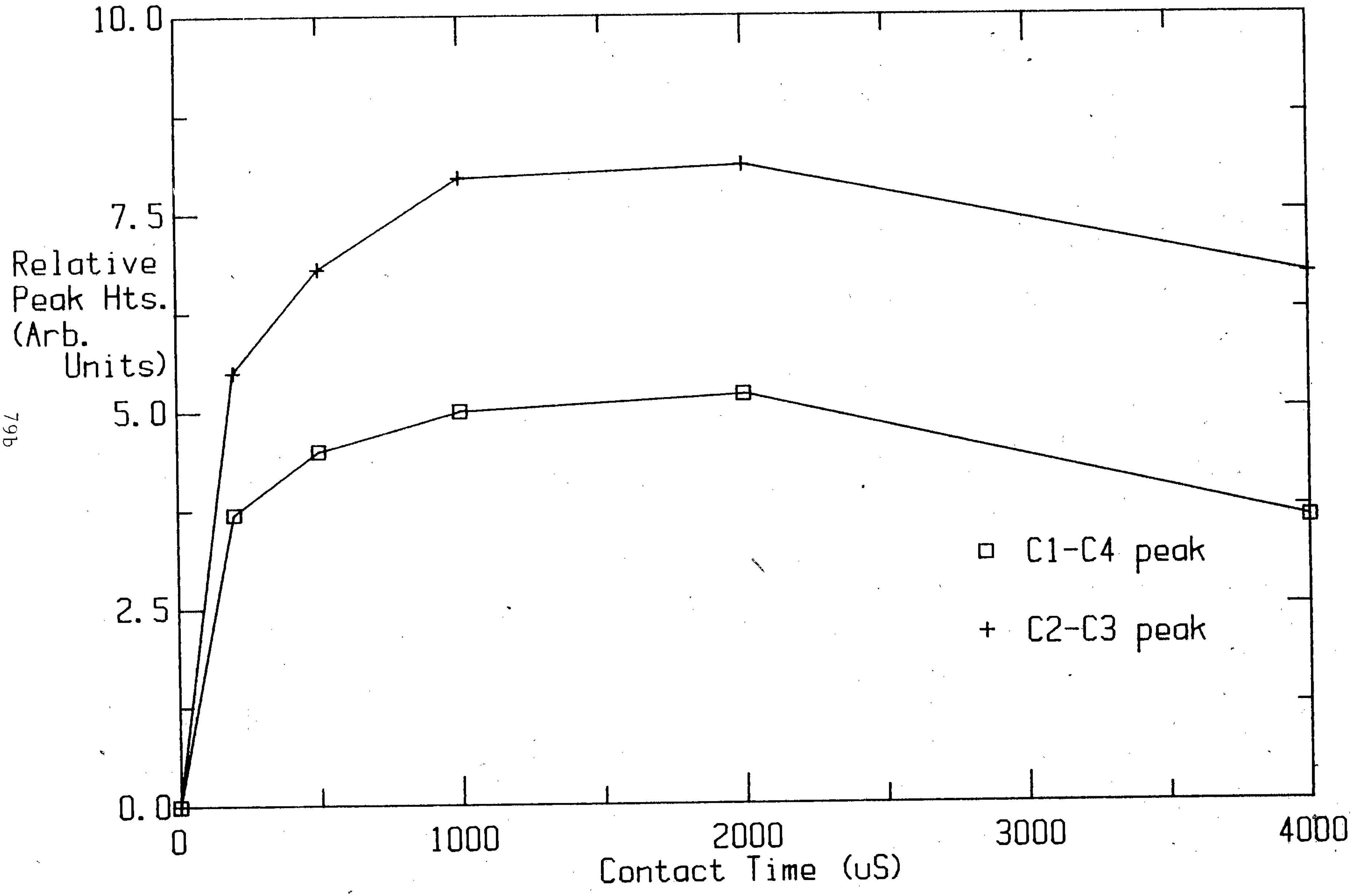
10.0
7.5
5.0
2.5
0.0
Relative Peak Hts. (Arb. Units)
0
1000
2000
3000
4000
Contact Time (uS)
□ C1-C4 peak
+ C2-C3 peak

THF molecules must be more than physisorbed, ie. chemisorption, as the polarization growth is nearly complete in only 200μS.

3.6.2 Sample Pretreatment

Extensive ^{13}C-NMR experiments were performed on samples of Li_xMoS_2, where x=0,1 and 3, with adsorbed THF. These samples were pretreated using different techniques.

The surfaces of the MoS_2 (x=0) samples were carefully pretreated prior to THF adsorption. Two methods were used to prepare the samples. The first used the reaction of H_2 at 200-300°C to remove any oxide impurities, followed by a vacuum treatment at 200-300°C. The second preparation was similar to the first but also included the chemisorption of oxygen at room temperature, followed by another vacuum treatment. This second method simulates the actual room temperature reactions of MoS_2 cathode powder with oxygen. The average amount of oxygen chemisorbed to the MoS_2 surface in these experiments was $3.13 \pm 0.55 \times 10^{-4}$ moles/g.

Lithiated molybdenum disulfides were prepared in liquid ammonia and transferred to the NMR sample preparation apparatus (glass vacuum rack) under inert atmosphere. These samples were pretreated under vacuum to $<1 \times 10^{-5}$ torr at temperatures of ≈200-250°C to remove co-intercalated ammonia.

The NMR tubes were sealed after pre-treatment of the Li_xMoS_2 powder and adsorption of THF. These samples were thermally decomposed in 50°C increments from room temperature, RT to 500°C for 3 hours at each temperature. The samples were cooled to RT at which all NMR measurements were taken.

3.6.3 ^{13}C-NMR Techniques

CP-MAS ^{13}C-NMR measurements were taken at each temperature in the thermal decomposition series. A 52 kHz spin-locking and decoupling field strength was used. The MAS samples were spun at the magic angle at 1.8-2.2kHz, therefore in the low field of 1.4T used for these spectra no spinning sidebands were seen. Other NMR techniques were used at certain temperatures to gain specific information not available through cross-polarization.

Cross-polarization experiments do not provide the whole picture as they discriminate in favour of static carbons which are bonded to protons. Gaseous molecules and rapidly moving physisorbed species, such as rotating methyl groups, produce very small signals. Gaseous decomposition components were identified using excitation of ^{13}C with 90° pulses with and without continuous decoupling of protons in a field of 52 kHz.

The ^{13}C-NMR results are summarized in Tables III and IV on page 82 and in Tables V and VI on page 92.

Table III - $MoS_2/H_2/THF$ ^{13}C-NMR Results	
Temperature	NMR Features
RT ⟶ 100°C	THF
150°C	THF, butanal (minor)
200°C	butane, propane, aromatics, butanal (minor)
250°C	butane, aromatics, butanal (minor), ethylene (minor)
300°C	aromatics, butane, propane, ethylene
350°C	aromatics, propane, butane, ethylene
400°C	aromatics, ethylene
450°C	aromatics, gases*
500°C	aromatics, methane, CO_2

Table IV - $MoS_2/H_2/O_2/THF$ ^{13}C-NMR Results	
Temperature	NMR Features
RT ⟶ 100°C	THF
150°C	THF, RCOOH, butanal (minor)
200°C	aromatics, butanal, RCOOH
250°C	aromatics, butanal, RCOOH, butane, ethylene
300°C	aromatics, propane, butane, butanal (minor)
350°C	aromatics, propane, ethane, CO_2
400°C	aromatics, CO_2, methane, ethane, propane
450°C	aromatics, gases*
500°C	aromatics, CO_2, methane

$R = CH_3-$ or $CH_3CH_2CH_2-$

* Specific experiments for gases not done at these temperatures.

3.6.4 $MoS_2/H_2/THF$

A thermal decomposition series from room temperature to 500°C was performed on a sample of MoS_2, pretreated with H_2, with adsorbed THF. CP-MAS-^{13}C-NMR was used at each step and the spectra from MAS #5 are shown in Fig.33 and 34.

At room temperature, RT and 100°C, the spectra are consistent with liquid THF which has ^{13}C shifts of 68.0 and 26.0ppm for the C_1-C_4 and C_2-C_3 carbons, respectively.(49) All chemical shifts are reported wrt TMS, calculated from a benzene standard run after each experiment. As the decomposition temperature is raised, the size of the 68.0ppm peak decreases suggesting ring cleavage at the C-O bonds.

At 150-250°C a small peak in the 190-200ppm range appears, consistent with either a ketone or an aldehyde. Using a 100μS delayed decoupling experiment on MAS #19, shown in Fig.35, this peak has a decreased intensity and is identified as an aldehyde. The peak does not completely disappear due to some degree of motion. This aldehyde is believed to be butanal due to the new peaks at 13-16 and 40ppm. Butanal has ^{13}C shifts of 13.3, 15.7, 45.7 and 201.6ppm.(50) The simultaneous disappearance of the 40 and 200ppm peaks at 300°C also suggests a relationship betweeen these two peaks.

Another new resonance is a broad 130ppm peak in the olefinic or aromatic region, first appearing at 200°C. The sp^3 (0-30ppm) and

Figure 33, 34 ^{13}C CP/MAS spectra of MAS #5: $MoS_2/H_2/THF$ thermal decomposition series. Temperature is designated on the right side of the spectra; decomposition period was 3 hours. Spinning rate = 2kHz. Rep. rate = $5s^{-1}$. 5.44 μmoles THF/m^2 MoS_2.

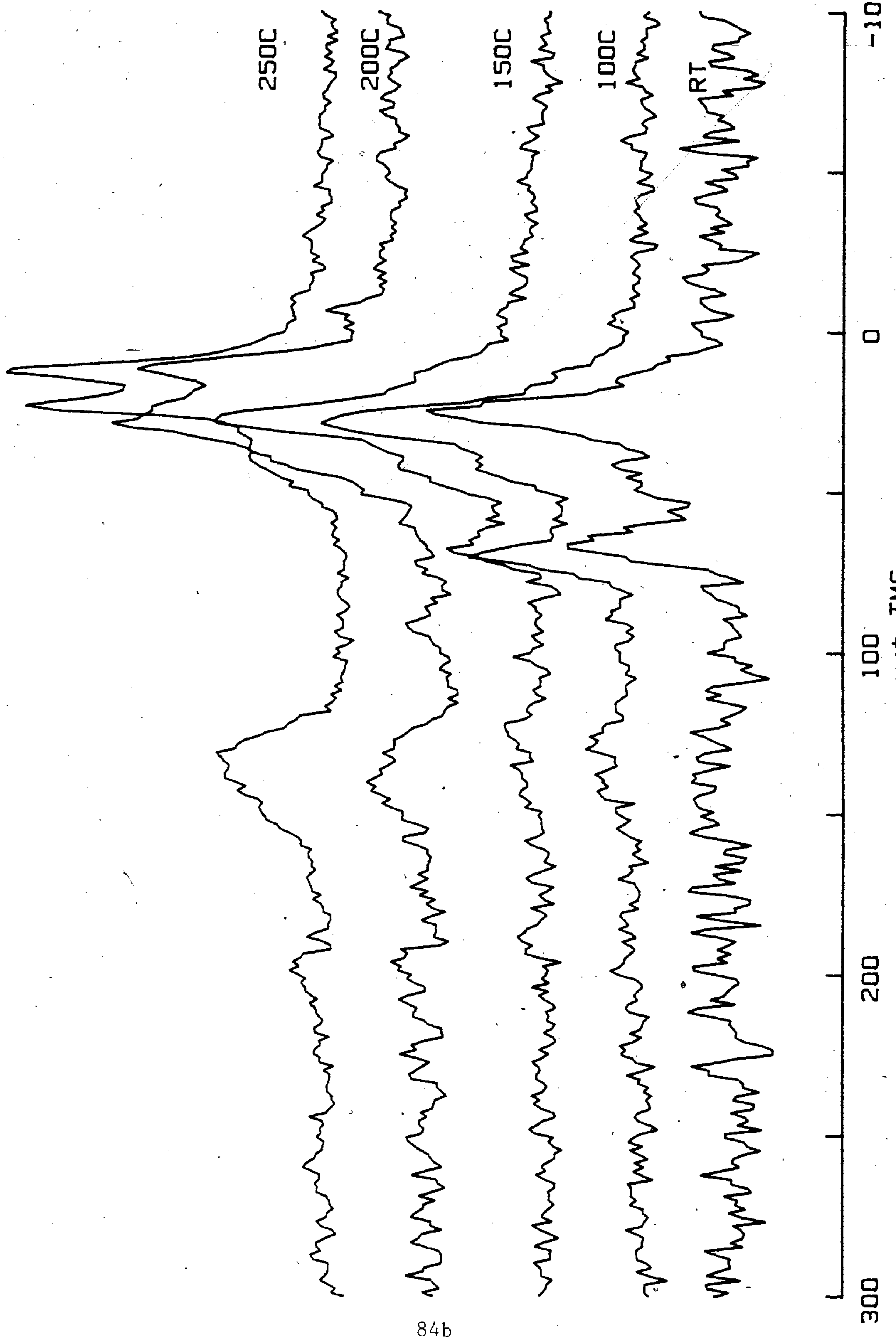
250C
200C
150C
100C
RT
-100
0
100
200
300
ppm wrt TMS

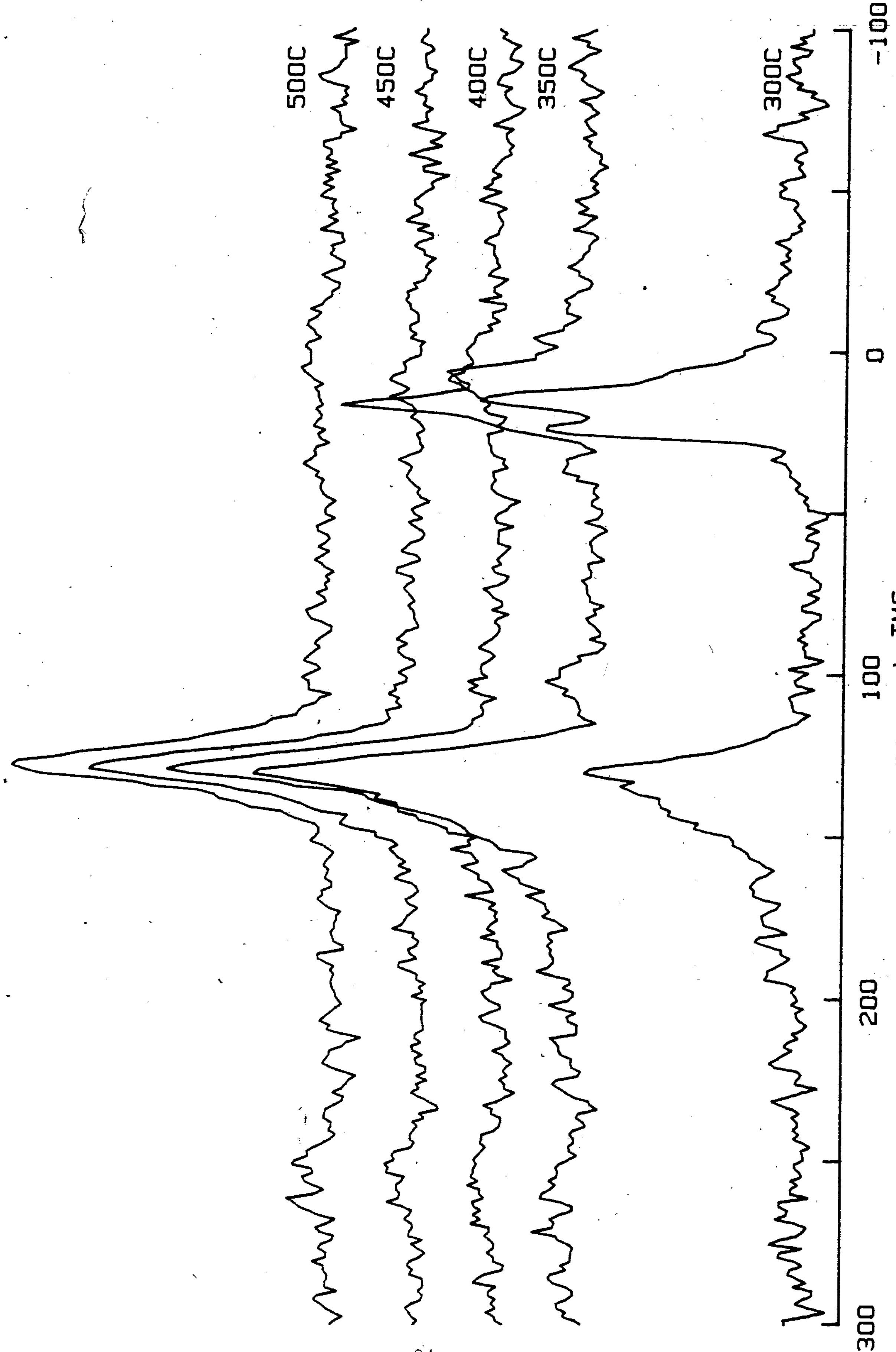
500C
450C
400C
350C
300C
-100
0
100
200
300
ppm wrt TMS

Figure 35 Various Pulsing Sequence of MAS #19: $MoS_2/H_2/THF$. 250°C thermal decomposition. 2.93 μmoles THF/m^2 MoS_2. All samples spun at 2kHz.

90/MAS: 90° pulse ^{13}C-NMR with ^1H decoupling. Rep. rate = 1 s^{-1}.

90/MAS/NoD: 90° pulse ^{13}C-NMR without ^1H decoupling. Rep. rate = 1 s^{-1}.

CP/MAS: Cross-polarization with ^1H decoupling. Rep. rate = 4s^{-1}. Contacts = 262,739.

CP/MAS/DD: Cross-polarization with 100μS delayed ^1H decoupling. Rep. rate = 4s^{-1}. Contacts = 262,739.

(The cross-polarization spectra have equivalent vertical scales.)

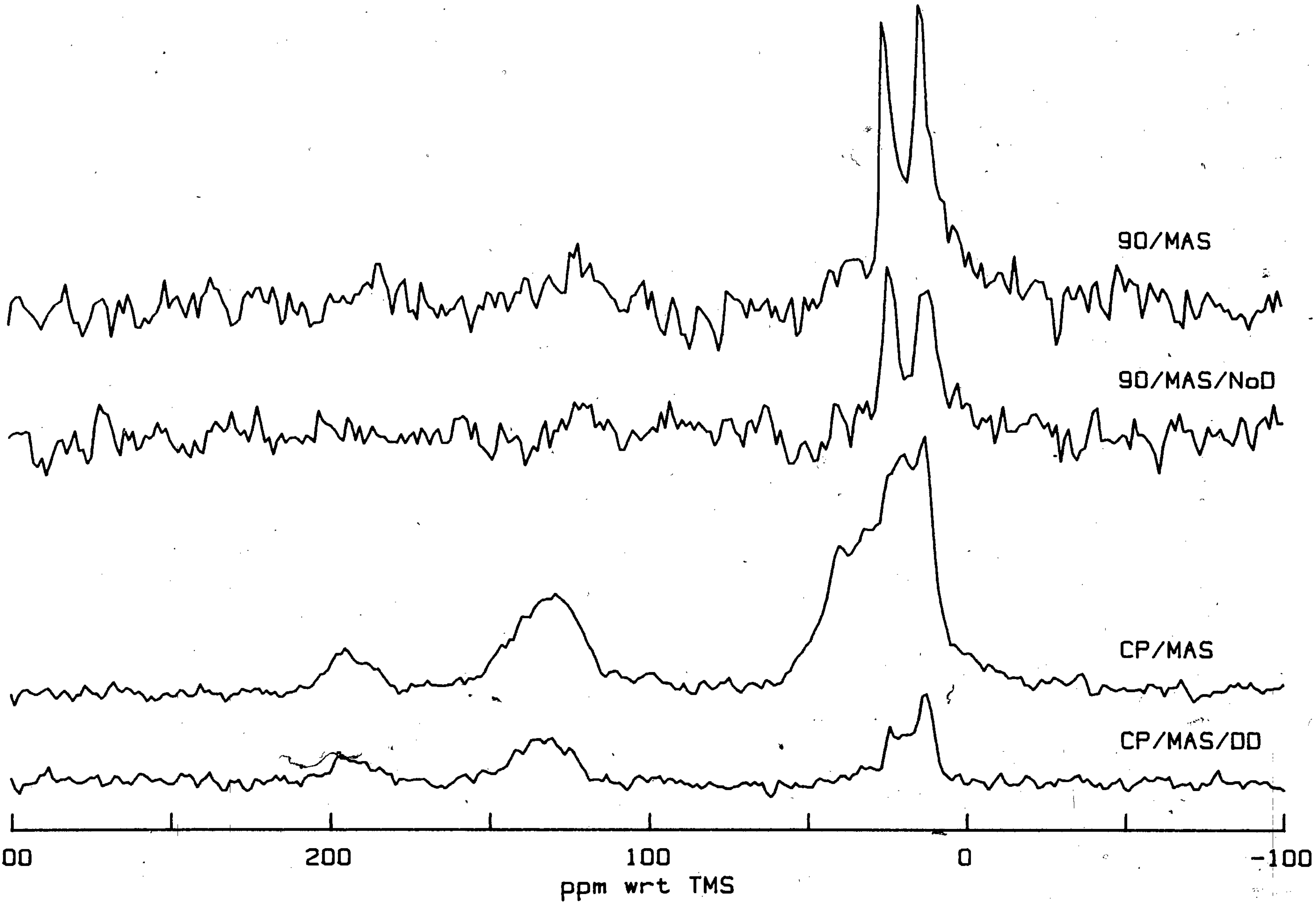
90/MAS
90/MAS/NoD
CP/MAS
CP/MAS/DD
300
200
100
0
-100
ppm wrt TMS

Figure 36 Various Pulsing Sequence of MAS #5: $MoS_2/H_2/THF$. 500°C thermal decomposition. 5.44 μmoles THF/m^2 MoS_2. All samples spun at 2kHz.

90/MAS: 90° pulse ^{13}C-NMR with ^1H decoupling.
Rep. rate = 1 s^{-1}.

90/MAS/NoD: 90° pulse ^{13}C-NMR without ^1H decoupling.
Rep. rate = 1 s^{-1}.

CP/MAS: Cross-polarization with ^1H decoupling.
Rep. rate = $5s^{-1}$. Contacts = 231,480.

CP/MAS/DD: Cross-polarization with 100μS delayed ^1H decoupling. Rep. rate = $5s^{-1}$.
Contacts = 231,480.

(The cross-polarization spectra have equivalent vertical scales.)

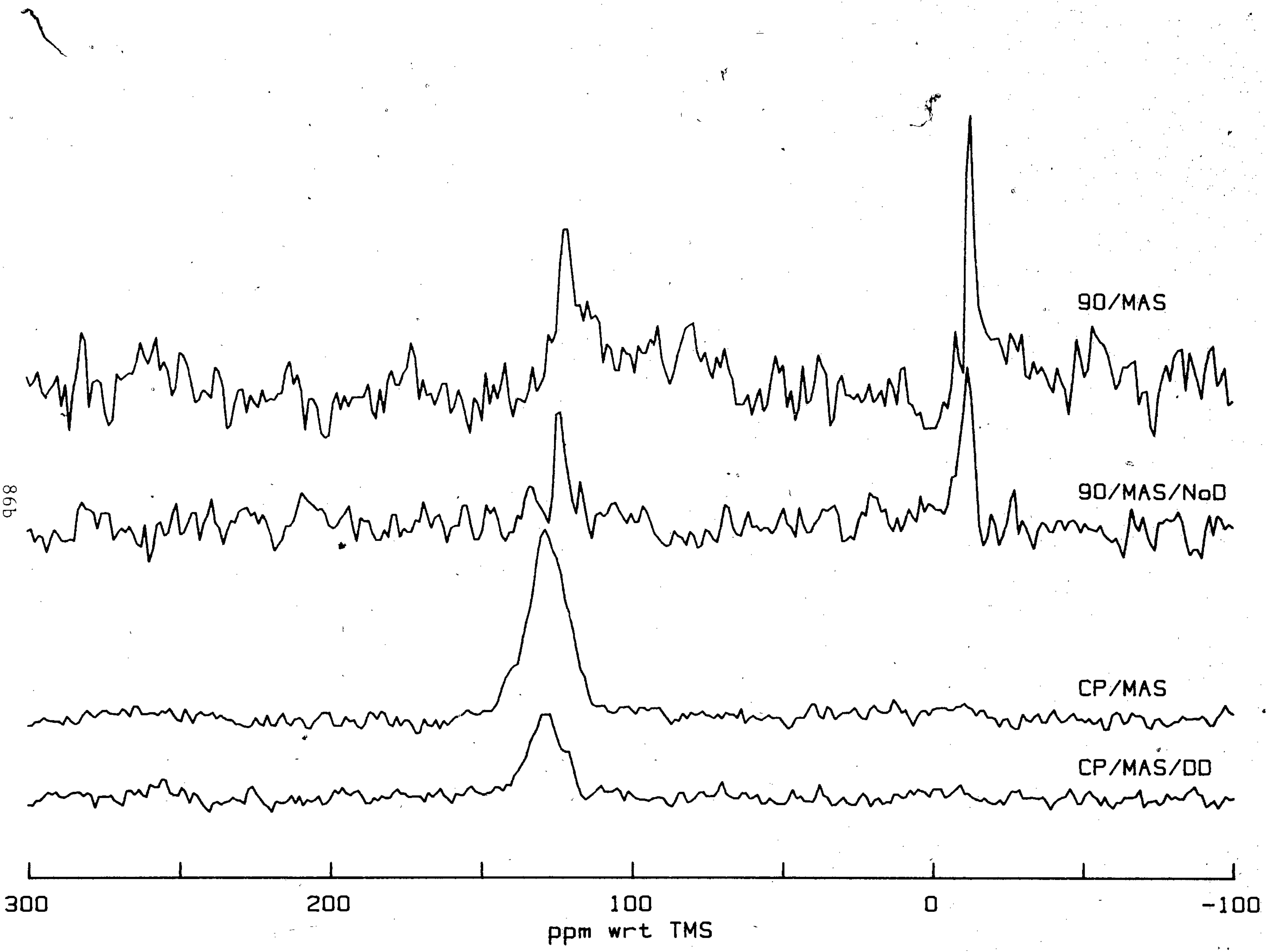
90/MAS
90/MAS/NoD
CP/MAS
CP/MAS/DD
300
200
100
0
-100
ppm wrt TMS

aldehydic carbons gradually disappear as the decomposition temperature is raised to 450°C, while the aromatic/olefinic peak at 128-130ppm grows considerably to become the lone peak in these cross-polarization experiments. At 500°C a delayed decoupling CP-MAS-^{13}C-NMR experiment was run on MAS #5 and is shown in Fig.36. These results show that only 1/2 of the carbons were directly bonded to protons. This resonance is probably due to aromatic ring structures.

Excitation of ^{13}C with 90° pulses was done at 250°C(Fig. 35), 300°C, 350°C, 400°C and 500°C(Fig. 36). The major gaseous component at 250°C is butane, while some ethylene is also present. Propane is also seen at 300-350°C. Ethylene was found at 400°C, while at 500°C methane and CO_2 are seen. The gases found by NMR at 500°C were verified by GC/MS experiments.

3.6.5 $MoS_2/H_2/O_2$/THF

A thermal decomposition series from room temperature to 500° was performed on a sample of MoS_2, pretreated with H_2 and O_2, with adsorbed THF. CP-MAS-^{13}C-NMR was used at each step and the spectra from MAS #6 are shown in Fig.37 and 38.

As with MoS_2/H_2/THF, the peaks in the room temperature, RT and 100°C spectra are adsorbed THF. Also similar is the appearance of an aldehydic/ketonic peak at 150-250°C, however, the size of this peak at

Figure 37, 38 ^{13}C CP/MAS spectra of MAS #6: $MoS_2/H_2/O_2$/THF thermal decomposition series. Temperature is designated on the right side of the spectra; decomposition period was 3 hours. Spinning rate = 2kHz. Rep. rate = $5s^{-1}$. 5.82 μmoles THF/m^2 MoS_2.

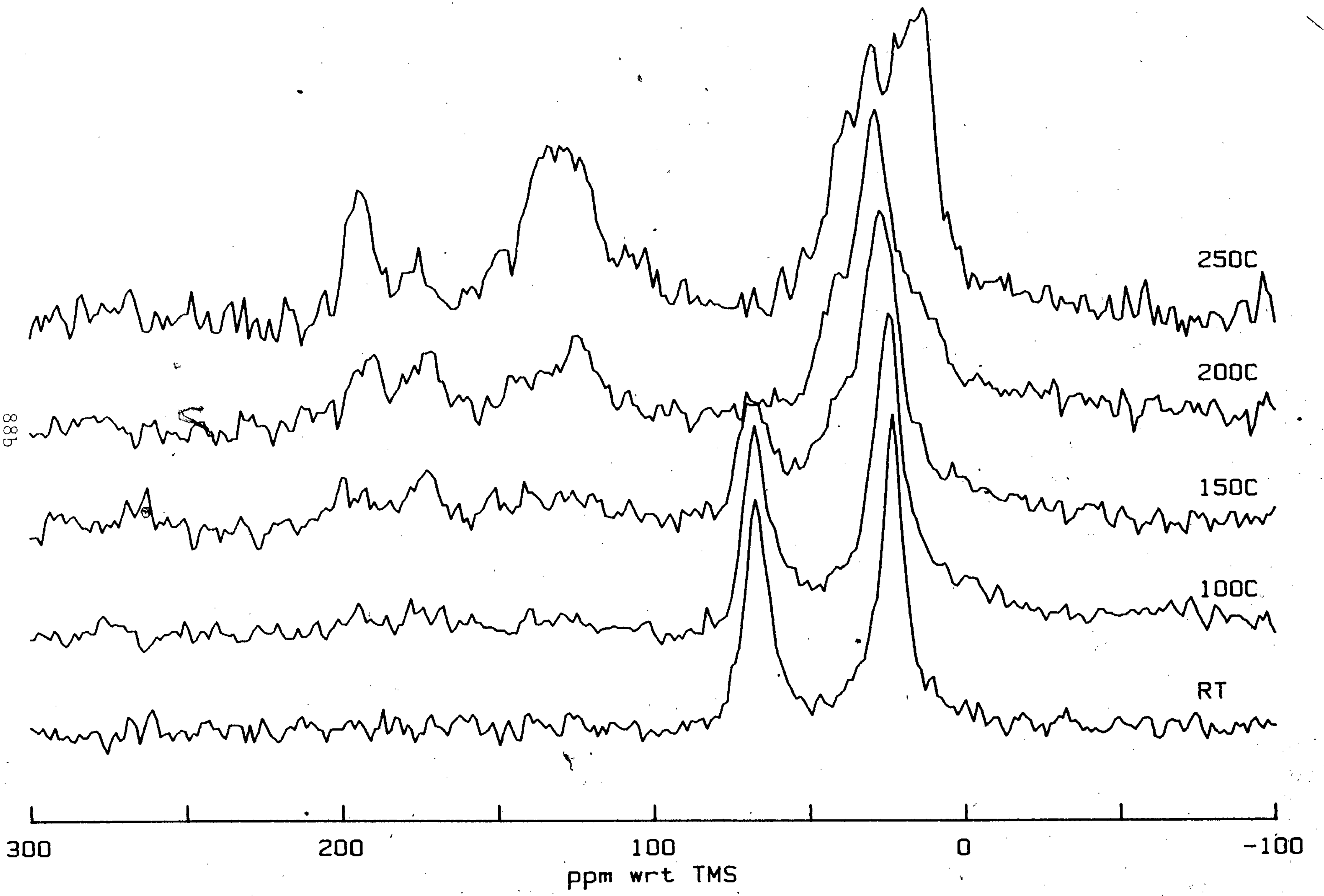
250C
200C
150C
100C
RT
300
200
100
0
-100
ppm wrt TMS

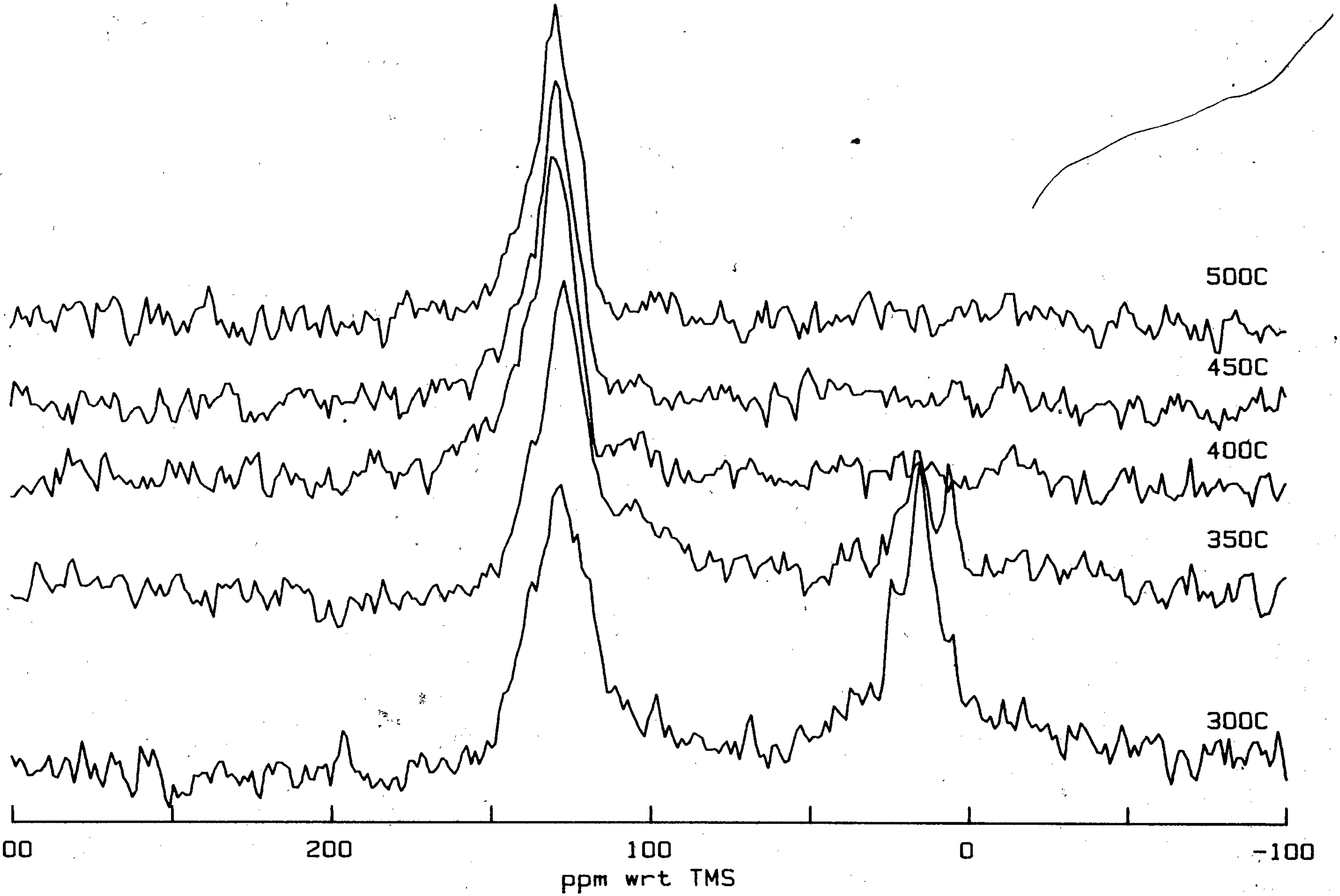
500C
450C
400C
350C
300C
300
200
100
0
-100
ppm wrt TMS

Figure 39 Various Pulsing Sequence of MAS #16: $MoS_2/H_2/O_2/THF$. 250°C thermal decomposition. 6.03 µmoles THF/m^2 MoS_2. All samples spun at 2kHz.

90/MAS:	90° pulse ^{13}C-NMR with ^{1}H decoupling. Rep. rate = 1 s^{-1}.
90/MAS/NoD:	90° pulse ^{13}C-NMR without ^{1}H decoupling. Rep. rate = 1 s^{-1}.
CP/MAS:	Cross-polarization with ^{1}H decoupling. Rep. rate = 4s^{-1}. Contacts = 390,510.
CP/MAS/DD:	Cross-polarization with 100µS delayed ^{1}H decoupling. Rep. rate = 4s^{-1}. Contacts = 390,510.

(The cross-polarization spectra have equivalent vertical scales.)

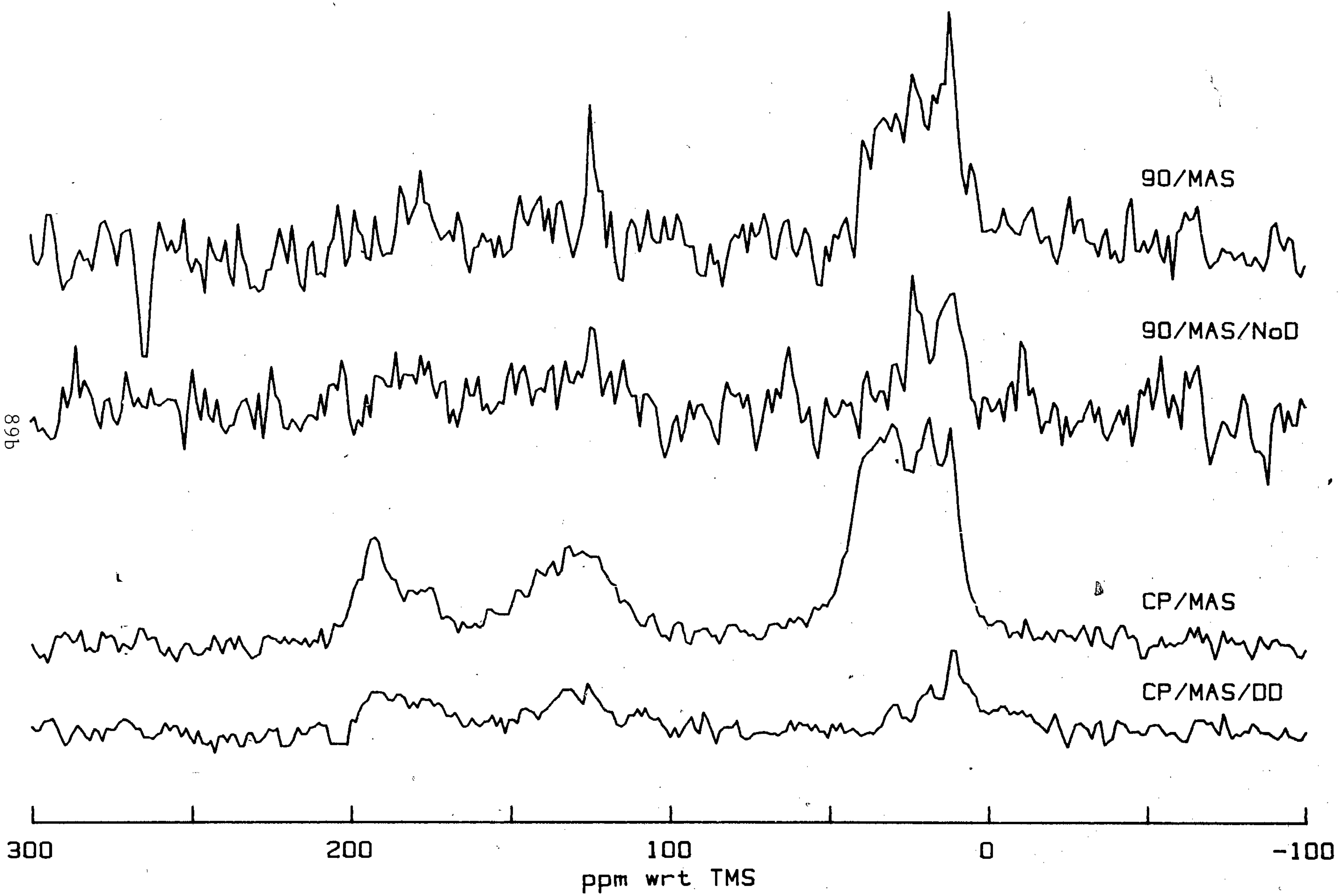
90/MAS
90/MAS/NoD
CP/MAS
CP/MAS/DD
300
200
100
0
-100
ppm wrt TMS

Figure 40 Various Pulsing Sequence of MAS #6: $MoS_2/H_2/O_2/THF$. 500°C thermal decomposition. 5.82 μmoles THF/m^2 MoS_2. All samples spun at 2kHz.

90/MAS: 90° pulse ^{13}C-NMR with ^1H decoupling. Rep. rate = 5 s^{-1}.

90/MAS/NoD: 90° pulse ^{13}C-NMR without ^1H decoupling. Rep. rate = 1 s^{-1}.

CP/MAS: Cross-polarization with ^1H decoupling. Rep. rate = 5s^{-1}. Contacts = 426,360.

CP/MAS/DD: Cross-polarization with 100μS delayed ^1H decoupling. Rep. rate = 5s^{-1}. Contacts = 426,360.

(The cross-polarization spectra have equivalent vertical scales.)

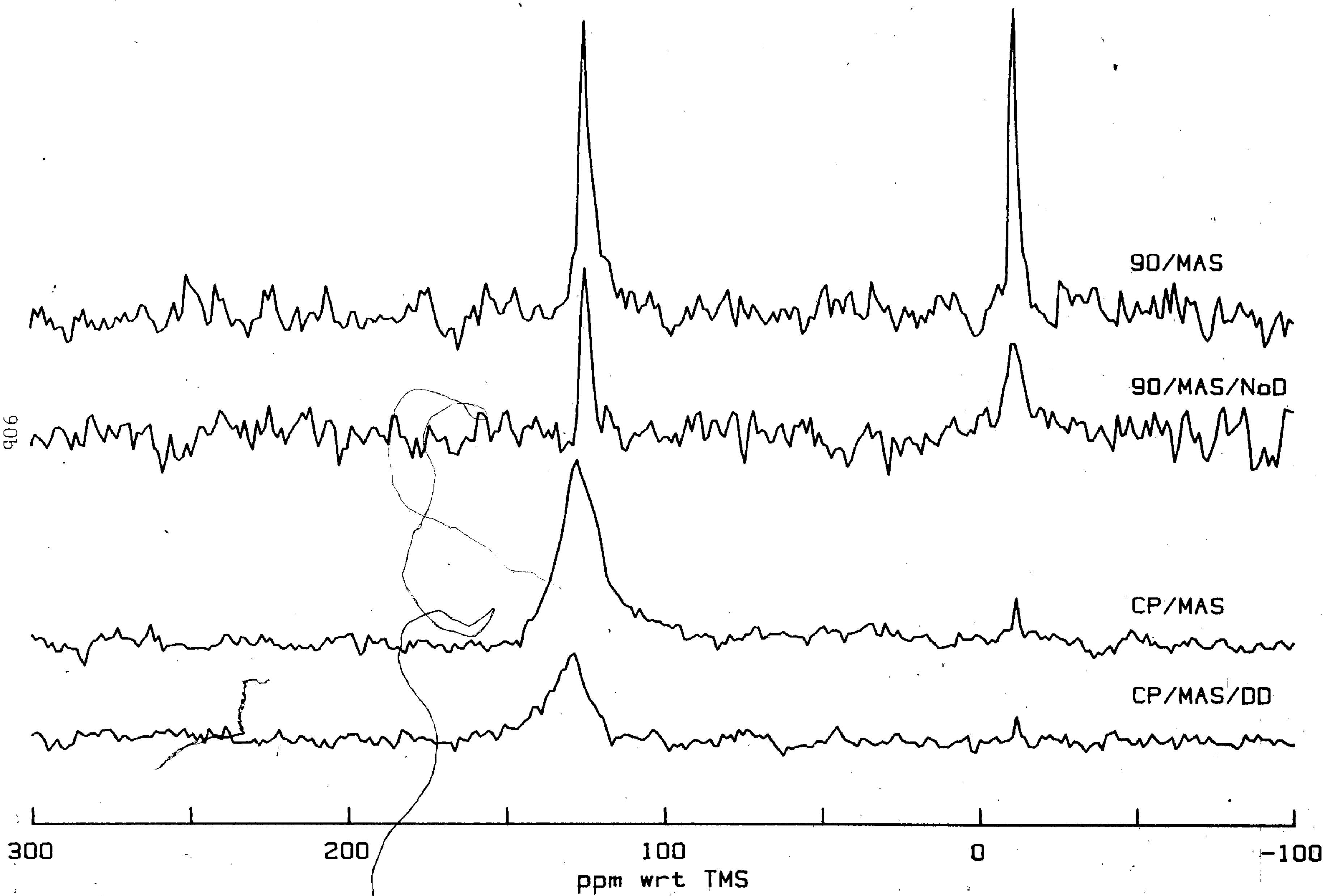
90/MAS
90/MAS/NoD
CP/MAS
CP/MAS/DD
300
200
100
0
-100
ppm wrt TMS

250°C is much greater in this $MoS_2/H_2/O_2$/THF sample. Delayed decoupling experiments on MAS #16 in Fig.39 show this peak to be aldehydic in nature. This peak is believed to be butanal as in the previous sample. The aromatic peak appears at 200°C and grows into the lone peak as before. Delayed decoupling experiments at 500°C in Fig.40 show only 1/2 of the carbons to be directly bonded to protons.

There appear to be two differences in the CP experiments between MoS_2/H_2/THF and $MoS_2/H_2/O_2$/THF. Firstly, the oxygen treated sample has a larger butanal peak relative to the sp^3 peaks in comparison to the hydrogen treated sample. Secondly, coincident with the aldehyde peaks at 150-250°C are peaks at 173-175ppm which are consistent with carboxylic acids or esters. The formation of an ester during THF decomposition is not probable. It is difficult to identify the exact acid from the spectra, but two possible choices are ethanoic acid (21, 177.2ppm) and butanoic acid (13.4, 18.5, 36.3, 179.6ppm).(50)

Excitation of ^{13}C with 90° pulses was done at 250°C(Fig.39), 300°C, 350°, 400°C and 500°C(Fig.40). At 250°C the major gases are butane and ethylene. Minor gases include propane and ethane. The general trend from 250 → 500°C is butane → propane → ethane → methane with combinations of gases in the intermediate temperature intervals. Ethylene and CO_2 resonances occur at similar frequencies but through nondecoupled proton experiments we found this peak due to ethylene below 350°C and due to CO_2 at 350°C or higher. At 500°C the two major gases are CO_2 and methane, which was confirmed by GC/MS experiments.

Table V - Li_1MoS_2/THF ^{13}C-NMR Results

Temperature	NMR Features
RT → 200°C	THF
250°C	butanal, butane, propane, ethanal (minor), methane (minor), THF(gas) (minor)
300°C	butanal
350°C	butanal, 12, 20, 30ppm
400°C	12, 20, 30ppm, aromatics (minor)
450°C*	methane, butane, ethylene
500°C*	methane, ethane, propane, butane

Table VI - Li_3MoS_2/THF ^{13}C-NMR Results

Temperature	NMR Features
RT → 100°C	THF
150°C	THF, n-butanol (minor)
200°C	THF, n-butanol (minor)
250°C	butane, propane, 29, 32, 42, 44ppm
300°C	sp^3 carbons
350°C	butane, propane, 2, 10, 20ppm
450°C*	12ppm

* No cross-polarization results at these temperatures.

3.6.6 Li_1MoS_2/THF

A thermal decomposition series from room temperature to 400°C was performed on a sample of Li_1MoS_2 with adsorbed THF. Due to the large initial amount of THF and subsequent gaseous decomposition, the sealed NMR sample exploded during the 450°C decomposition. CP-MAS-^{13}C-NMR was used at each step and the spectra for MAS #13 are shown in Fig.41 and 42.

From the thermal decomposition series of Li_1MoS_2 the first sign of THF decomposition is at 250°C, 100° higher than for MoS_2. The peaks present at 250°C are consistent with butanal, however, a small 31 ppm peak could be due to the ethanal (31.2, 199.6ppm).(50) The aldehydic peak at 185ppm is verified using a delayed decoupling experiment and is shown in Fig.43. The size of the aldehyde peak decreases until 400°C where it is not present, while a resonance at 30-31ppm grows into a large peak at 400°C. The combination of peaks at 400°C (12, 20 and 31ppm) are not consistent with any decomposition product we could hypothesize. A broad aromatic/olefinic peak is beginning to appear at 400°C.

Excitation of ^{13}C with 90° pulses was done at 250°C(MAS #15 shown in Fig.43) and 500°C(MAS # 9) using MAS samples. A thermal decomposition series was done using a larger, static sample #22 at RT, 150°C, 250°C, 350°C and 450°C. Gaseous decomposition products are first found at 250°C where butane, propane and methane(minor) along with

Figure 41, 42 ^{13}C CP/MAS spectra of MAS #13: Li_1MoS_2/THF thermal decomposition series. Temperature is designated on the right side of the spectra; decomposition period was 3 hours. Spinning rate = 2kHz. Rep. rate = $4s^{-1}$. 4.55 μmoles THF/m^2 Li_1MoS_2.

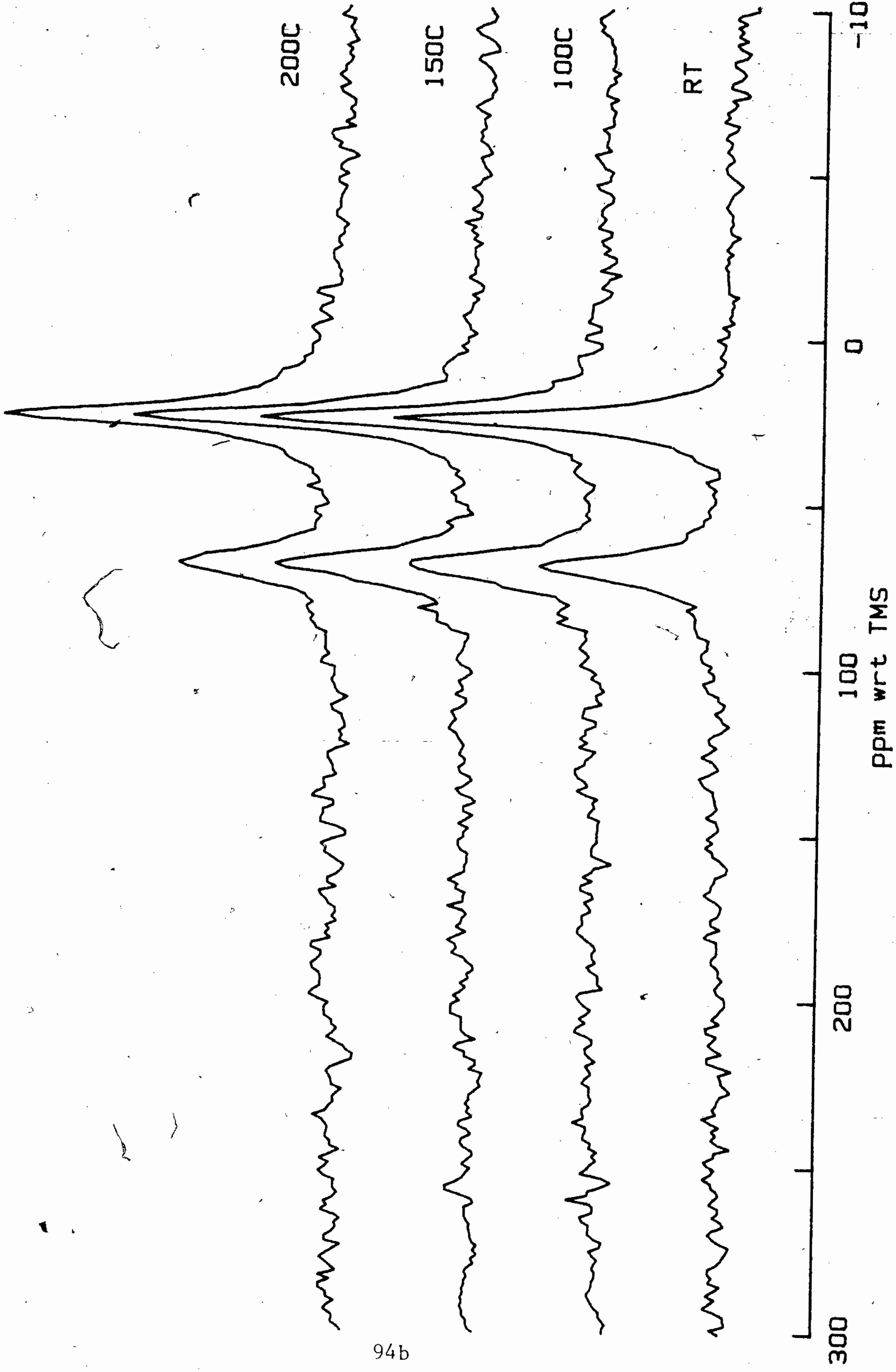
200C
150C
100C
RT
-100
0
100
200
300
ppm wrt TMS

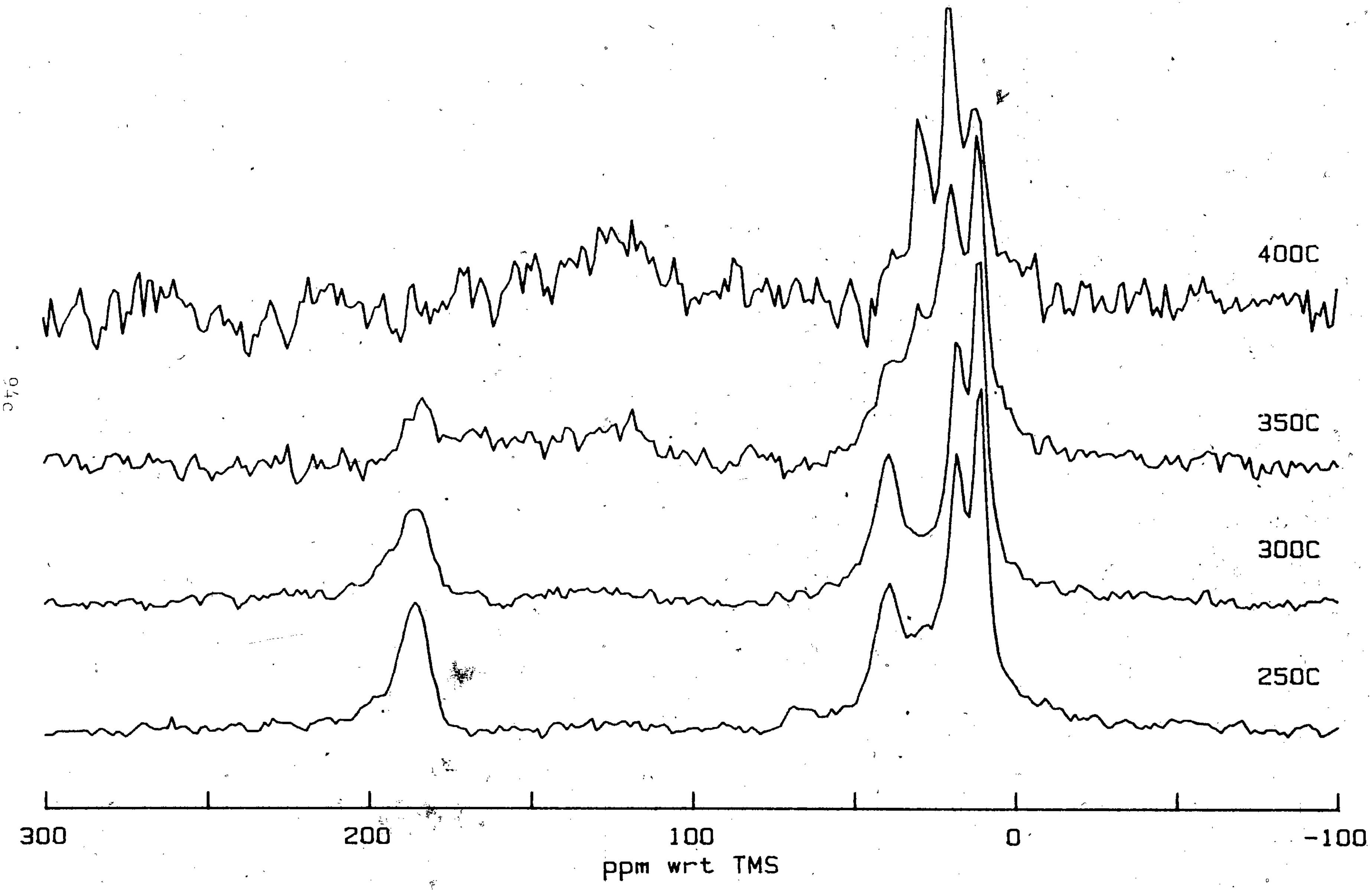
400C
350C
300C
250C
300
200
100
0
-100
ppm wrt TMS

Figure 43 Various Pulsing Sequence of MAS #15: Li_1MoS_2/THF. 250°C thermal decomposition. 6.32 μmoles THF/m^2 Li_1MoS_2. All samples spun at 2kHz.

90/MAS: 90° pulse ^{13}C-NMR with ^{1}H decoupling. Rep. rate = 1 s^{-1}.

90/MAS/NoD: 90° pulse ^{13}C-NMR without ^{1}H decoupling. Rep. rate = 1 s^{-1}.

CP/MAS: Cross-polarization with ^{1}H decoupling. Rep. rate = 4s^{-1}. Contacts = 234,556.

CP/MAS/DD: Cross-polarization with 100μS delayed ^{1}H decoupling. Rep. rate = 4s^{-1}. Contacts = 234,556.

(The cross-polarization spectra have equivalent vertical scales.)

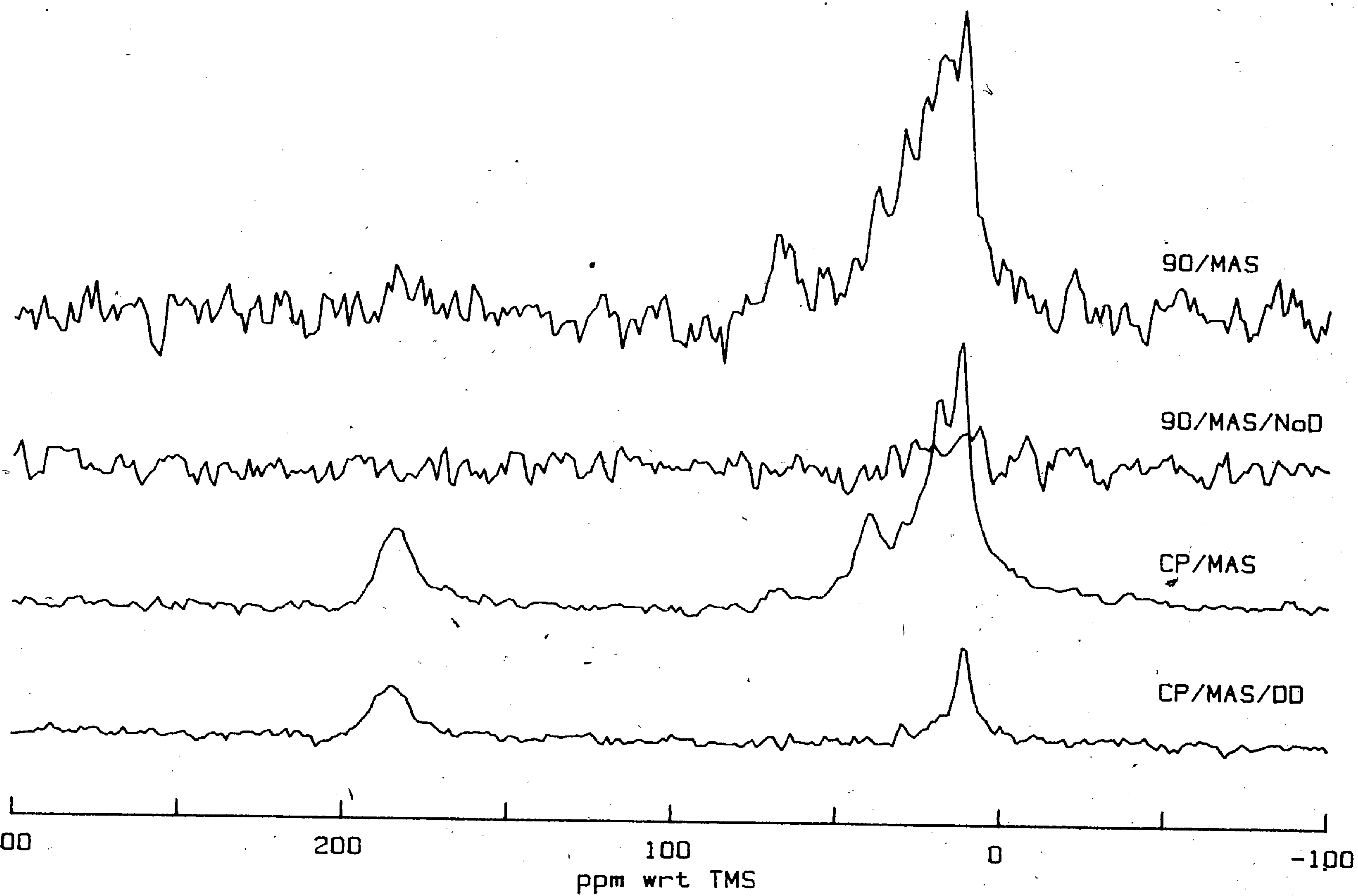
90/MAS
90/MAS/NoD
CP/MAS
CP/MAS/DD
300
200
100
0
-100
ppm wrt TMS

residual THF are seen. At 350°C we obtained the 10, 21, 29ppm combination previously seen using cross-polarization. This molecule(s) therefore had some degree of freedom or some molecules must be in the gas phase. This combination of peaks overlap one another from 10-30ppm and any gases expected in this region may be hidden beneath. At 450°C we see a large ethylene peak along with the C_1 to C_4 alkanes, but using MAS #9 at 500°C we see only the C_1 to C_4 alkanes: methane, ethane, propane and butane.

3.6.7 Li_3MoS_2/THF

A thermal decomposition series from room temperature to 350°C was performed on a sample of Li_3MoS_2 with adsorbed THF. This sample exploded during the 400°C decomposition. CP-MAS-^{13}C-NMR was used at each step and the spectra for MAS #18 are shown in Fig.44 and 45.

The first sign of decomposition occurs at 150°C where small peaks appear in addition to the THF spectra. The ^{13}C shifts for butanol are 13.9, 19.4, 35.3 and 61.7ppm(50) and all of the peaks are present at 150-200°C. It is believed that a butanol or lithium n-butoxide species is formed at this point.. At 250°C the spectrum has a saw tooth appearance. No THF or butanol/n-butoxide species are present at this point due to the absence of 67 and 61ppm peaks respectively. The peaks are due to sp^3 bonded carbons but are not consistent with any hypothesized decomposition products. Thermal decomposition at 300-350°C produces more gaseous species shown by the decrease in signal-to-noise

Figure 44, 45 ^{13}C CP/MAS spectra of MAS #18: Li_3MoS_2/THF thermal decomposition series. Temperature is designated on the right side of the spectra; decomposition period was 3 hours. Spinning rate = 2kHz. Rep. rate = $4s^{-1}$. 8.28 μmoles THF/m^2 Li_3MoS_2.

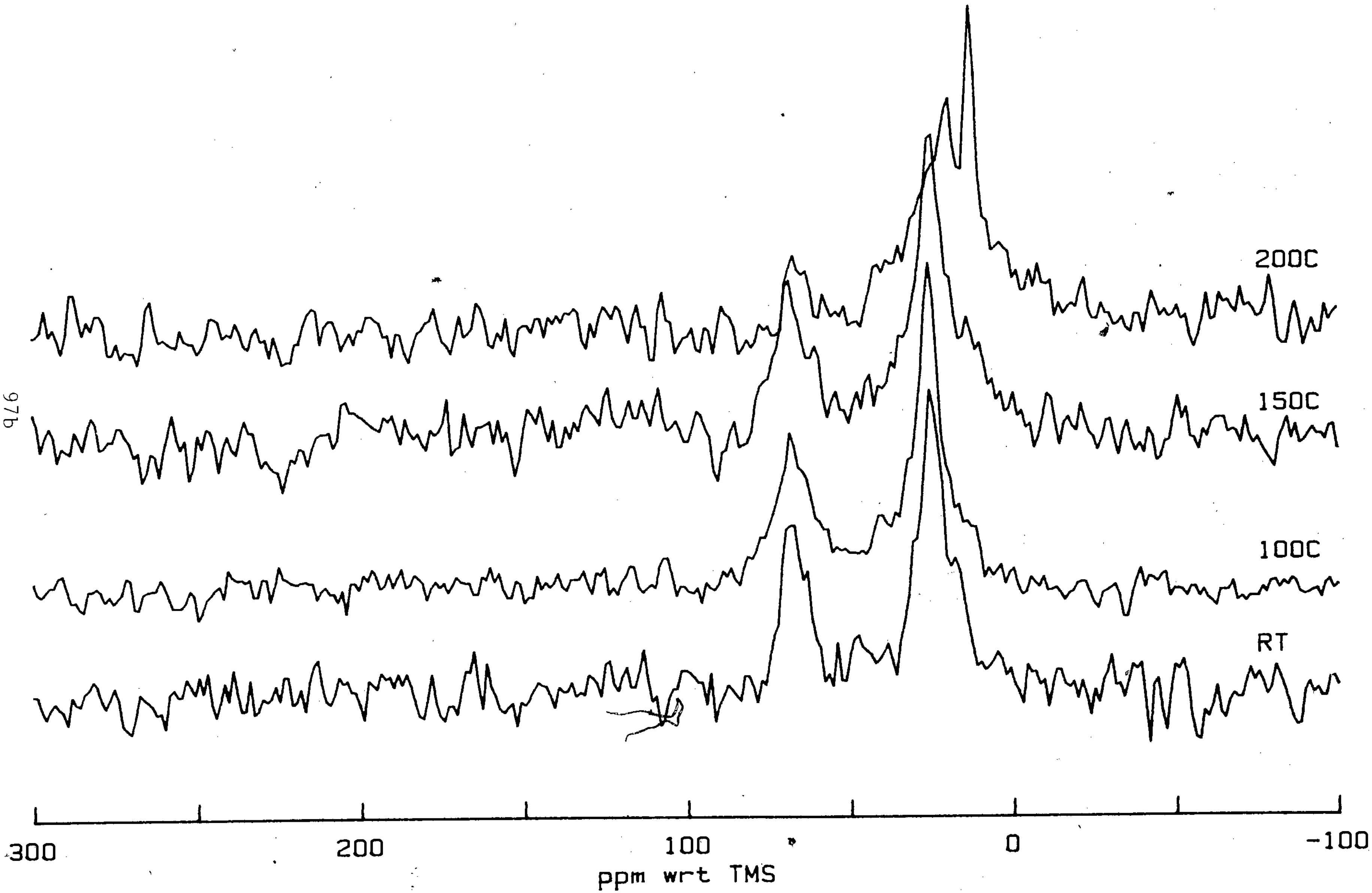
200C
150C
100C
RT
300
200
100
0
−100
ppm wrt TMS

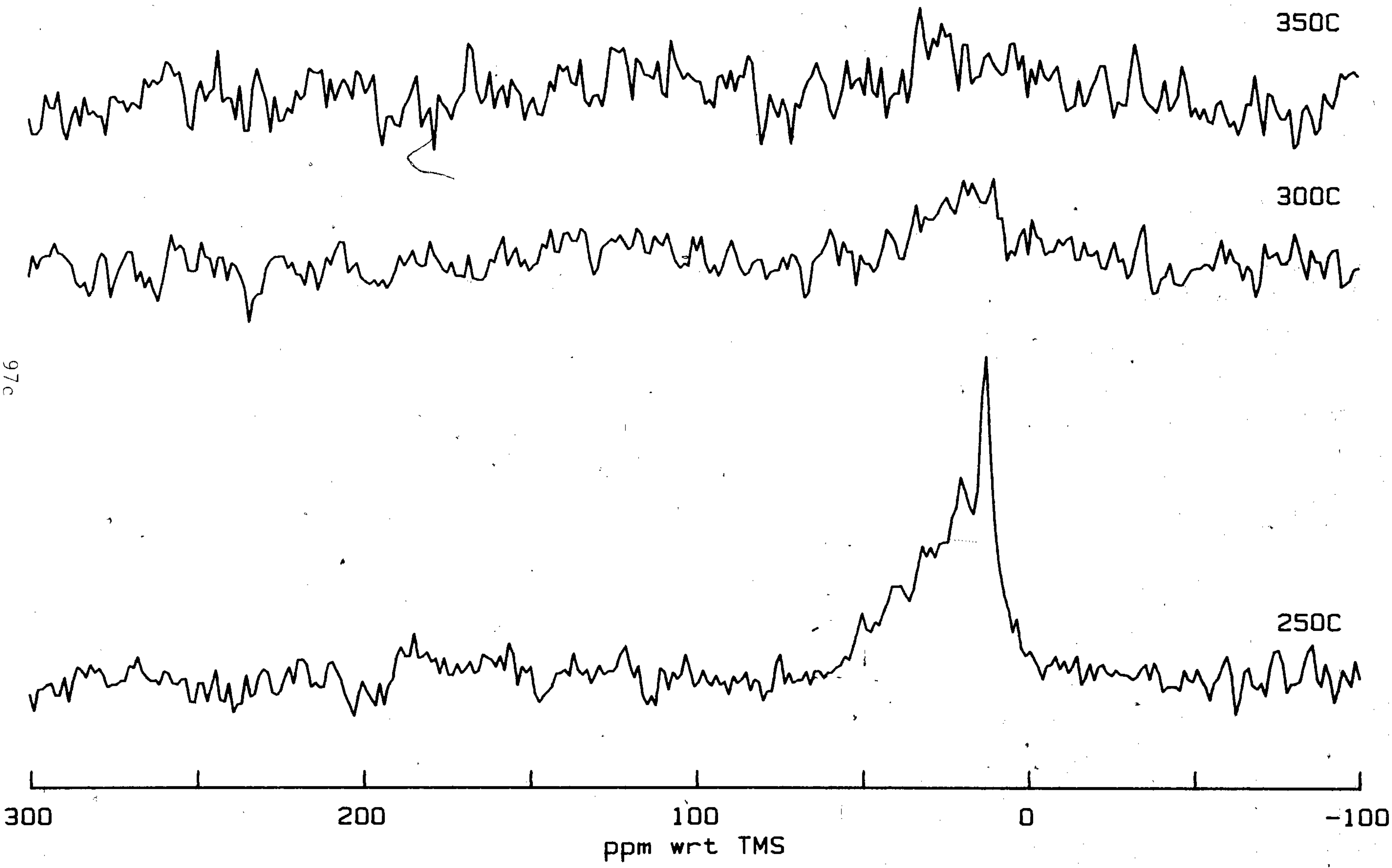
350C
300C
250C
300
200
100
0
-100
ppm wrt TMS

Figure 46 Various Pulsing Sequence of MAS #18: Li_3MoS_2/THF. 250°C thermal decomposition. 8.28 μmoles THF/m^2 Li_3MoS_2. All samples spun at 2kHz.

90/MAS: 90° pulse ^{13}C-NMR with ^{1}H decoupling. Rep. rate = 4 s^{-1}.

90/MAS/NoD: 90° pulse ^{13}C-NMR without ^{1}H decoupling. Rep. rate = 1 s^{-1}.

CP/MAS: Cross-polarization with ^{1}H decoupling. Rep. rate = $4s^{-1}$. Contacts = 269,604.

CP/MAS/DD: Cross-polarization with 100μS delayed ^{1}H decoupling. Rep. rate = $4s^{-1}$. Contacts = 269,604.

(The cross-polarization spectra have equivalent vertical scales.)

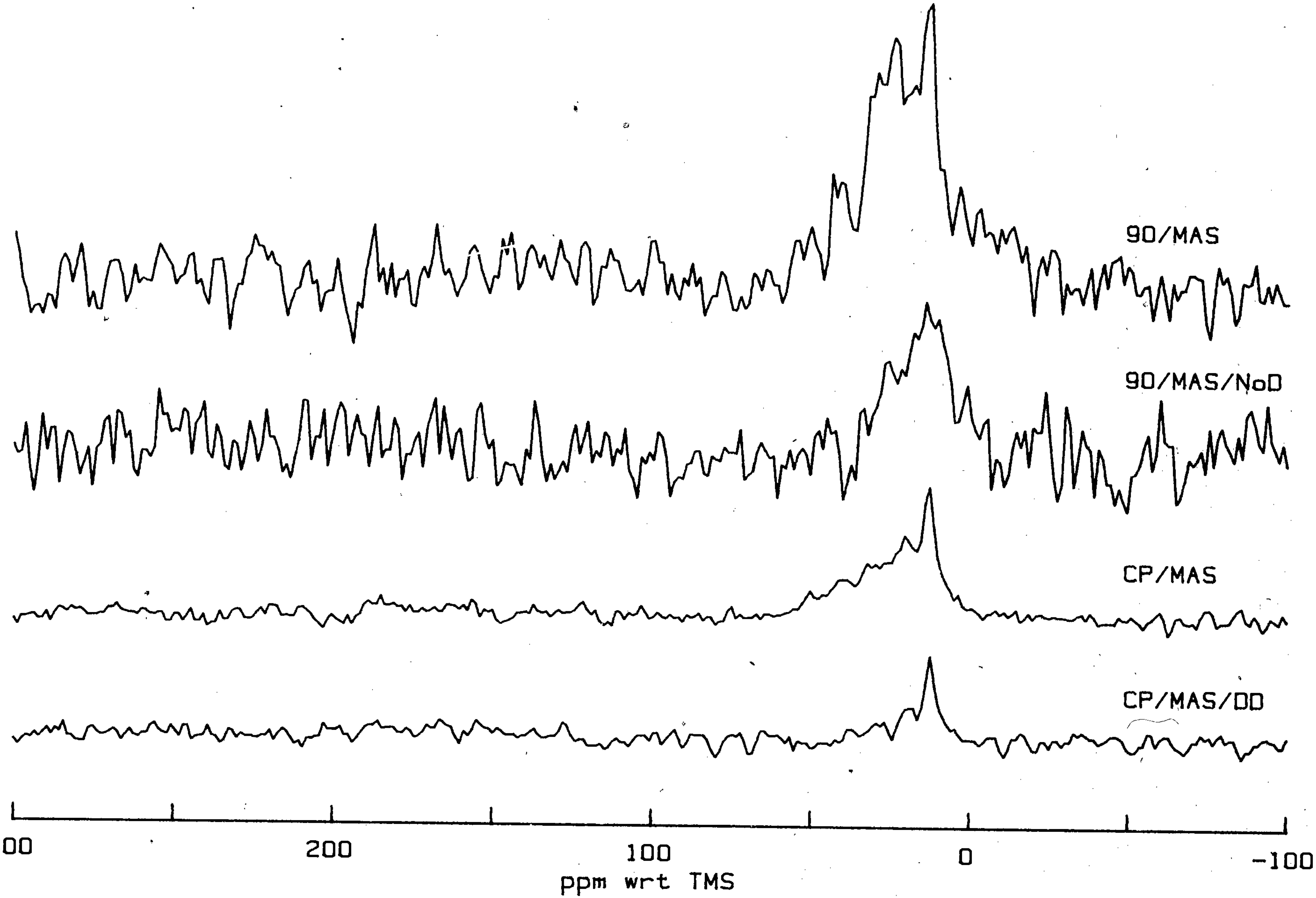
90/MAS
90/MAS/NoD
CP/MAS
CP/MAS/DD
300
200
100
0
-100
ppm wrt TMS

ratio of these cross-polarization experiments.

Excitation of ^{13}C with 90° pulses was done at 250°C(Fig.46) and 350°C using the MAS #18 sample. A thermal decomposition series was done using a larger, static sample #23 at RT, 150°C, 250°C, 350°C and 450°C. Gaseous decomposition products are first found at 250°C where butane, propane and two unidentified peaks at 29 and 32ppm are seen. THF is no longer present at 250°C. Butane and propane are also seen at 350°C along with unidentified 2, 10 and 20ppm peaks. At 450°C the signal-to-noise has become poor but a single unidentified peak at 12 ppm is seen.

3.6.8 Summary of ^{13}C-NMR Results

Using ^{13}C-NMR measurements the decomposition of THF adsorbed on pre-treated Li_xMoS_2, where x=0,1 and 3, was observed. Elevated temperatures were used as no reactions occurred at room temperature.

In general the MoS_2 samples, where x=0, were more reactive at lower temperatures than the lithiated MoS_2 samples. Decomposition of THF first occurred in the MoS_2 samples at 150°C, while 250°C was the lowest temperature of decomposition for Li_1MoS_2. Minor decomposition of Li_3MoS_2 was found at 150°C.

The pre-treatment of MoS_2 with H_2 or H_2 and O_2 was found to affect the nature of the decomposition products of THF. The sample pre-treated with H_2 alone had a smaller relative amount of aldehyde and CO_2 than the

O_2 treated MoS_2 sample. The O_2 treated sample also shows a carboxylic acid decomposition product. The surface oxygen seems to be involved in the decomposition of THF and formation of oxygen containing species.

The gaseous products follow a trend in the thermal decomposition of the MoS_2 samples. Larger molecules such as butane and unsaturated molecules such as ethylene are initially formed but as the temperature of decomposition increases the trend is to form propane → ethane → methane and CO_2. At the highest temperature, 500°C, methane and CO_2 were the only gases present.

The large aromatic peak which is formed at higher temperatures in the MoS_2 samples could not be further identified. Efforts to extract this compound were unsuccessful and described in section 3.7.3.

The least reactive of all Li_xMoS_2 samples was x=1. This sample did react at 250°C, however to form an aldehyde, possibly butanal and/or ethanal, butane and propane similar to the MoS_2 samples. At 500°C methane, ethane, propane and butane were all present while CO_2 was absent. The absence of CO_2 may be explained by the presence of the oxygen scavenger lithium, forming lithium oxide or carbonate. Obviously Li_1MoS_2 is less reactive than MoS_2 as the gases have not completely decomposed to methane. This decrease in reactivity in comparison to MoS_2 may be due to a change in Mo coordination induced by lithium intercalation.

Different decomposition products were observed as the lithium content of Li_xMoS_2 was increased to x=3. n-Butanol was observed as the major non-gaseous product while no aldehydes were seen. Li_3MoS_2 is a stronger reducing agent than Li_1MoS_2 or MoS_2 and therefore the reduction of THF to n-butanol and not an aldehyde is expected.

The decomposition products of the lithiated MoS_2 samples were more difficult to interpret with a number of unidentified peaks. This is believed to be due to the presence of lithium in the reaction scheme.

In a paper describing the reactions of THF with lithium, Koch found using preparative GLC, infrared analysis and proton NMR, the major decomposition product to be n-butanol.(1) Koch also implicated the formation of lithium n-butoxide, the enolate anion of acetaldehyde and ethylene as intermediates in the decomposition of THF with lithium. These products and the mechanisms of their formation, although simplistic considering the number of decomposition products observed in these NMR experiments, are in general agreement with our results.

3.7 **Miscellaneous Experiments**

3.7.1 Thermal Decomposition of Tetrahydrofuran.

The thermal decomposition of tetrahydrofuran was first studied by Klute and Walters in 1946.(51) THF was decomposed at pressures of 50-300torr and temperatures of 529-569°C. At the lower percentage of decomposition they found the chief products were ethylene, CO, methane, with smaller amounts of higher unsaturated compounds, H_2 and ethane. Near completion of decomposition, they found the percentage of unsaturated compounds to decrease and the percentage of saturated hydrocarbons and CO to increase. They also indicated the following decomposition mechanism:

$$\begin{array}{llll} C_4H_8O & \longrightarrow & CH_3CHO & + \ C_2H_4 \\ & & \llcorner\!\!\longrightarrow & CH_4 + CO \end{array} \qquad \text{Eq.24}$$

In our NMR experiments decomposition products of adsorbed THF were found as low as 150°C. THF was completely decomposed in all Li_xMoS_2 NMR samples at 250°C. The temperature of 250°C was therefore chosen for the following experiment.

This experiment was used to determine if THF decomposition was catalytically controlled by Li_xMoS_2. Five mls of THF was heated to 250°C for 3 hours in an evacuated 40ml stainless steel reaction vessel. No gaseous decomposition products were found using GC/MS. No liquid decomposition products were detected using 400.13MHz ^{1}H-NMR on the liquid THF after heating. Thus, any decomposition reaction of THF occurring at or below 250°C must be catalyzed to proceed.

3.7.2 $MoS_2/H_2/^{13}CO$ NMR Sample

A MAS NMR sample (#17) was prepared with high surface area MoS_2, pretreated with H_2, followed by adsorption of ^{13}CO(MSD Isotopes). Excitation of ^{13}C with 90° pulses with ^{1}H decoupling was performed on this sample with a spinning rate of 2520±50Hz and a repetition rate of $1s^{-1}$. A peak at 203 ppm with a peak width at half-height of 440Hz and two spinning side bands with 10 and 18% intensity of the main peak at ±2520Hz were observed.

This sample proves that if CO was present as a decomposition product of THF, as suggested by Equation 24, we would observe a peak at ≈200 ppm. Gaseous CO has a resonance at 182ppm(50), however this shift may change after chemisorption and is dependent on the nature of the surface. The resonances observed at 173-175ppm are therefore not due to chemisorbed CO as CO adsorbed on MoS_2 has a shift of ≈200ppm.

3.7.3 Solvent Extraction of Aromatic Species

Removal of the decomposition products from the MoS_2 surfaces of two thermal decomposition samples using solvent extraction was attempted. The powders from MoS_2/H_2/THF (MAS #5) and $MoS_2/H_2/O_2$/THF

(MAS #6) were used. Solvents and powders were exposed only to dry room air with a relative humidity of <1%. Two mls of D6-acetone(MSD Isotopes) was used to extract the aromatic rings and H_2O from ≈0.3g of each powder. After 48 hours, including 30 min. of ultrasonic vibration, the powders were filtered and the filtrates were saved. A blank sample was also prepared. The powders were air dried and a second extraction using carbon tetrachloride(Fisher Spec. Grade) was done.

The filtrates were then run on a 400.13MHz ^1H-NMR spectrometer. The ^1H-NMR runs were also repeated with D_2O added to confirm the presence of H_2O peaks.

A doublet H_2O peak was seen in the blank D6-acetone ^1H-NMR spectrum whereas singlet H_2O peaks were seen in the sample ^1H-NMR spectra. The ratios of H_2O:acetone were greater for the blank (0.87:1) than for $MoS_2/H_2/THF$ (0.32:1) or $MoS_2/H_2/O_2/THF$ (0.54:1). The doublet peaks in the blank suggest recent introduction of H_2O, possibly from the NMR tube. The singlet peaks suggest mixing of acetone deuterium atoms with H_2O protons for some time. Thus H_2O may have been extracted from the powder.

No peaks originating from the samples were seen in the 7-8 ppm region, where one would expect to see aromatic protons from benzene or other aromatic multi-ring compounds. A sample was prepared using 0.343g of MoS_2, pretreated at 200°C with H_2, followed by room temperature adsorption of 22μmoles of benzene. D6-Acetone was used to extract benzene molecules adhered to the surface of the powder. The ^{1}H-NMR spectrum of this sample had a strong proton resonance at 7.23ppm characteristic of benzene. The species in the CP-MAS ^{13}C-NMR spectra of the 500°C thermally decomposed samples appear to be aromatic but may be fused or chemisorbed to the MoS_2 surface and therefore not extractable.

3.7.4 CP MAS ^{13}C-NMR Spectrum of Cathode Material

A MAS NMR sample (#21) was prepared using high surface area Li_xMoS_2 cathode material from experimental cells. Cross-polarization ^{13}C-NMR was performed on this NMR sample.

Three experimental cells, using MoS_2 and lithium as electrodes in a 1M $LiAsF_6$/THF electrolyte solution, were discharged to x values of 3.0, 3.8 and 2.8 for Li_xMoS_2. These cells were dissassembled in a helium glove box, the lithiated cathode material was scraped off and put into a MAS sample tube. The MAS NMR tube was sealed under vacuum without exposure to the atmosphere.

The observed CP ^{13}C-NMR spectrum had two peaks at 26.7 and 69.6ppm consistent with THF. No impurities or decomposition products were seen in this spectrum.

3.7.5 THF Solvent Decomposition in an Li/Li_xMoS_2 Cell

An experimental cell using MoS_2(held in place with nickel exmet screen) and lithium electrodes(area=$1.54cm^2$) separated by ≈0.8cm and a larger electrolyte volume(≈1.5ml) than in previous cells was assembled. 1M $LiAsF_6$/THF was used for an electrolyte. The initial potential of this cell was 3.66V with respect to a lithium reference electrode.

This cell was potentiostated at 2.0V overnight and later at 0.1V for 9 days. After the potential of 0.1V was achieved, a residual current of ≈0.013mA was observed for 9 days.

Ideally the total number of coulombs should have been datalogged to determine if the number of coulombs necessary for lithium intercalation to Li_3MoS_2 was surpassed, thus assuming the extra coulombs are involved in solvent decomposition. Prior to the residual current of ≈0.013mA, the currents were approx. two orders of magnitude higher during the initial intercalation. These initial currents are assumed to be equivalent to or greater than the calculated value of 112.2 coulombs needed to intercalate 0.062g of MoS_2 to x=3. The charge of ≈10.1 coulombs from the residual current over 9 days is therefore assumed to be due to solvent decomposition.

The electrolyte was removed from the cell, put through a 1.0μm filter and analyzed using a 400.13MHz ^{1}H-NMR spectrometer. A blank containing repurified, filtered THF was run for comparison. Both spectra have very strong THF proton signals. No other peaks due to decomposition products were seen in these experiments, which have a lower detection limit of approx. 1 part in 1000.

This experiment was performed in an attempt to correlate the thermal decomposition products of the ^{13}C-NMR study with Li/Li_xMoS_2 electrochemical cells. The results from this experiment are not conclusive as the total coulombs passed was not datalogged and one has to assume that solvent decomposition did occur within the time frame of the experiment. The lower detection limit must also be considered when reviewing this negative result for THF solvent decomposition in a Li/Li_xMoS_2 cell.

4.0 Conclusions

Initially the goal of this research was to find a new technique for observing cathodic solvent decomposition in lithium batteries, primarily the Molicel®. Solid State MAS-^{13}C NMR, was chosen due to its strengths which have been observed in the study of surface catalysis reactions. With this technique one could observe solvent decomposition on the surface of Li_xMoS_2 at varying degrees of lithiation, thus simulating the discharge of a lithium battery.

Tetrahydrofuran, a solvent with high vapor pressure, was ideal as monolayer adsorptions were easily carried out in the gas phase. Its excellent low temperature properties make tetrahydrofuran an important lithium battery solvent.

Typical molybdenum disulfide unfortunately did not meet the necessary requirements due to its low surface area. Great effort therefore, went into the syntheses of lithiated and non-lithiated high surface area MoS_2. Poorly crystalline Li_xMoS_2 materials, which maximized THF adsorption for this NMR study, were prepared.

Striking observations were revealed by electrochemical cells made with both types of MoS_2 cathode powder. The low surface area MoS_2 underwent sharp phase transitions to new crystal structures during the intercalation of lithium. High surface area or poorly crystalline MoS_2 has very little long-range ordering as seen by the absence of sharp voltage plateaus during discharge. Poorly crystalline MoS_2, however reversibly intercalates a greater fraction of lithium than its crystalline counterpart, resulting in higher capacity during cycling.

No decomposition products were found for any sample at room temperature, therefore the variation of x in Li_xMoS_2 samples could not be used to determine a solvent reduction potential for THF. Decomposition was observed at elevated temperatures.

MoS_2 was found to be more reactive with regard to THF decomposition than Li_1MoS_2, due possibly to structural differences induced by lithiation. MoS_2 is obviously catalytically active prior to lithiation. A trend of greater catalytic activity with increasing lithiation values was not observed. The nature of the THF decomposition products however, depended on x in Li_xMoS_2.

APPENDIX 1 - Li_xMoS_2 Synthesis

Sample #	Sample Type	Preparation Method	Surf. area m^2/g	Dens. g/ml	S/Mo	Notes
IP8	MoS_2	$MoCl_4 + Li_2S$				Yield=44%;Xray→Li_2S
IP10	MoS_2	$MoCl_4 + CH_3CSNH_2 + NH_4OH$				V. fine particles
IP11	MoS_2	"				"
IIP68	MoS_2	$MoCl_5 + [(CH_3)_3C]_2S$	<5			"
IIP82	MoS_2	$MoCl_5$ +LiHS(author	<5			31% Yield
IP18A	MoS_2	Li_xMoS_2 Exfoliation				DI H_2O Stirring
IP18B	MoS_2	"				DI H_2O Ultrasonic
IP26	MoS_2	"				.06M HCl(2xH^+ excess
IP28	MoS_2	"	<1			.06M HNO_3(")
IP36	MoS_2	"				"
IP39	MoS_2	"	1.5			.5M HNO_3 (2xH^+ excess
IP45	MoS_2	T.D.ofATTM(Aldrich	20.3		1.96	450°;1hAr;1h5%H_2/Ar
IP50	MoS_3	"	32.5		3.0	300°;1hAr
IP51	MoS_2	"	49.2		2.06	300°;1hAr;1h5%H_2/Ar
IP58	MoS_2	"	12.5		1.98	500°;1h5%H_2Ar
IP62	MoS_2	"			2.19	300°1hAr;350°1h5%H_2
IP62	"	"			2.16	above + 2h5%H_2/Ar
IP62	"	"			2.15	above + 2h5%H_2/Ar
IP62	"	"			2.14	above + 2h5%H_2/Ar
IP62	"	"			2.12	above + 2h5%H_2/Ar
IP66	MoS_2				2.78	300°1hAr;350°1hNH_3
IP67	MoS_2	"			2.08	350°22h5%H_2/Ar
IP68	MoS_2	"	7.2		2.01	350°48h5%H_2/Ar
IP73	MoS_2	"	44.7		2.18	350°2h5%H_2/Ar
IP84	MoS_2	"	44.4		2.34	350°1hAr;1h5%H_2/Ar
IP92	MoS_2	"	30.6		2.30	"
IP120	MoS_2	"	7.1		2.56	"
IP136	MoS_2	"	40.6			"
IP148	MoS_2	"	25.9			"
IP161	MoS_2	"	10.4			200°.25h,350°.75hAr 350°1h5%H_2/Ar
IP166	MoS_2	"	21.1			350°1hAr;1h5%H_2/Ar
IIP34	MoS_2	"	13.2		2.03	"
IP168	ATTM	Brauer(17)				Dried 100° under Ar
IP176	ATTM	"				Dried 100° vacuum
IIP33	ATTM	"				"
IIP93	ATTM	"				"
IP169	MoS_3	C.D.of ATTM(Author	61.6			H_2SO_4 pH<3.5
IP173	MoS_3	"	<10			H_2SO_4 pH=1
IP177	MoS_3	"	74.4			1.3% H_2SO_4/DI H_2O
IP184	MoS_3	"	13.3			3.3% H_2SO_4/DI H_2O
IIP16	MoS_3	"	43.4			5% H_2SO_4/DI H_2O
IIP29	MoS_3	"	47.5			10% HNO_3/DI H_2O
IIP35	MoS_3	"	41.9			"
IIP36	MoS_3	"	42.6			2.7% HNO_3/DI H_2O

APPENDIX 1 - Li_xMoS_2 Synthesis (cont'd)

Sample #	Sample Type	Preparation Method	Surf. area m^2/g	Dens. g/ml	S/Mo	Notes
IIP46	MoS_3	"	23.2			20% HNO_3/DI H_2O
IIP51	MoS_3	"	4.4			3% HNO_3/DI H_2O
IIP59	MoS_3	"	<5			10% HNO_3/DI H_2O
IIP81	MoS_3	"	18.0			1% H_2SO_4/DI H_2O
IIP83	MoS_3	"	28.7			"
IIP94A	MoS_3	"	128.9	1.57		1%FormicAcid/DI H_2O
IIP94B	MoS_3	"	107.9	1.05		1%Formic/DI H_2O/24h
IIP100	MoS_3	"	186.8	1.53		5%Formic/DI H_2O/24h
IIP101	MoS_3	"	192.8	1.38		"
IIP105	MoS_3	"	161.9	1.50		"
IIP109	MoS_3	"	228.5	1.29		5%Formic/DI H_2O/48h
IIP175	MoS_3	C.D.ofATTM(Aldrich	243.7			5%Formic/DI H_2O
IIP192	MoS_3	"	190.2	0.62		5%Formic/DI H_2O/48h
IIIP1	MoS_3	"	206.0	0.79		"
IIIP2	MoS_3	"		0.80		5%Formic/DI H_2O/5d
IIIP3	MoS_3	"		0.61		5%Formic/DI H_2O/4d
IIIP47	MoS_3	"		0.72		5%Formic/DI H_2O/3d
IIIP5	MoS_3	"		1.33		5%Formic/DI H_2O/5d
IIIP62	MoS_3	C.D.of ATTM(Author				5%Formic/DI H_2O/24h
IIIP93	MoS_3	"	178.6			"
IIP111	MoS_2	T.R.of MoS_3(IIP94)	128.7	1.43	2.04	350°10minAr;20minH_2
IIP114	MoS_2	" (IP100)	41.6	1.88	2.00	425°;15minH_2
IIP123	MoS_2	" (IIP100)	59.5	1.90	2.10	425°;3minH_2;1minAr
IIP131	MoS_2	" (IIP100)	44.4	2.08	2.00	500°;3minH_2;1minAr
IIP134	MoS_2	" (IIP100)	72.9	1.99	2.07	"
IIP139	MoS_2	" (IIP101)	84.1	2.13	2.00	200°6h15%H_2/He; 10minAr
IIP143	MoS_2	" (IIP105)	75.0			"
IIP161	MoS_2	" (IIP105)	61.9			"
IIP176	MoS_2	" (IIP109)	108.5			"
IIP183	MoS_2	" (IIP109)				"
IIP191	MoS_2	" (IIP175)				"
IIIP28	MoS_2	" (IIP175)			2.17	"
IIIP30	MoS_2	" (IIIP1)				"
IIIP33	MoS_2	" (IIIP1)		1.19		"
IIIP42	MoS_2	" (IIP192)	77.3	0.90		250°; "
IIIP63	MoS_2	" (IIP62)	94.5	2.10	2.03	"
IIIP69	MoS_2	" (IIIP4)		1.33		"
IIIP70	MoS_2	" (IIIP4)		1.33		"
IIIP76	MoS_2	" (IIIP62)	72.2	2.21		"
IIIP97	MoS_2	" (IIIP93)				"
IIIP100	MoS_2	" (IIIP93)			2.26	"

APPENDIX 1 - Li_xMoS_2 Synthesis (cont'd)

Sample #	Sample Type	Preparation Method	Surf. area m^2/g	Dens. g/ml	S/Mo	Notes
IP112	Li_xMoS_2	Li_2(BZPH)/THF	9.5			Lith. not complete
IP125	Li_1MoS_2	2.5M nBuLi/nhexane	6.6			Heat evolved
IP131	Li_1MoS_2	.25M nBuLi/nhexane	2.0			V.little heat
IP137A	Li_1MoS_2	2.5M nBuLi/nhexane	10.0			Init.S.A.=40.6m^2/g
IP137B	Li_1MoS_2	.25M nBuLi/nhexane	8.0			"
IIP58	Li_1MoS_2	"	32.5			UsedcMoS_2,not tMoS_2
IIP64	Li_1MoS_2	"	37.1			"
IIP157	Li_1MoS_2	"	<1			"
IIP170	Li_1MoS_2	Li/NH_3	26.0			Sample exposed:Air
IIP174	Li_1MoS_2	"	41.1	1.18		x=1.05(Dionex)
IIIP11	Li_1MoS_2	"	75.0	1.08		x=1.02±.03(Dionex)
IIIP73	Li_3MoS_2	"	41.6	0.87		x=3.19(2X by Dionex

APPENDIX 2 - X-ray Diffraction Results for $(NH_4)_2MoS_4$

Miller Indices	Calculated Angle (2θ)	Experimental Angle (2θ)
0 0 2	14.413	
0 1 1	14.562	14.50
1 1 1	17.258	17.30
2 0 0	18.484	18.50
2 0 2	23.517	23.60
0 1 3	25.187	
0 2 0	25.448	25.30
1 2 1	28.090	28.20
3 0 1	28.829	28.90
0 0 4	29.062	
0 2 2	29.366	29.15
1 0 4	30.548	30.65
3 1 1	31.591	
2 2 0	31.637	31.70
2 2 1	32.486	32.55
2 2 2	34.924	
1 2 3	34.989	35.00
3 0 3	35.599	35.65
4 0 0	37.472	37.50
0 1 5	38.829	38.90
1 2 4	40.166	40.15
1 3 1	40.454	
3 0 4	40.709	40.55
2 1 5	43.328	43.40
0 3 3	44.694	44.80
4 2 0	45.843	45.90
3 2 4	48.623	48.60
3 3 1	48.871	48.85
5 1 1	49.800	49.90
0 2 6	51.706	51.80
0 4 0	52.273	52.35
1 2 6	52.641	52.80
3 0 6	53.083	53.20
1 1 7	54.741	54.90
2 2 6	55.381	
1 4 2	55.422	55.50
2 4 0	55.922	56.00
5 2 2	56.696	56.70
2 4 2	58.073	58.05

APPENDIX 2 - X-ray Diffraction Results for $(NH_4)_2MoS_4$ (cont'd)

Miller Indices	Calculated Angle (2θ)	Experimental Angle (2θ)
3 2 6	59.760	59.80
0 4 4	60.922	61.00
1 4 4	61.764	61.90
5 3 1	63.166	63.10
6 2 0	63.979	64.00
1 3 7	67.466	
4 3 5	67.751	67.65
1 5 1	68.109	68.20
6 2 3	68.415	68.40

REFERENCES

1. V.R. KOCH. J. Electrochem. Soc. **126**, 181 (1979).

2. R.R. HAERING, J.A.R. STILES and K. BRANDT. U.S. Patent No. 4,224,390. 1980.

3. W.R. McKINNON. Ph.D. thesis. University of British Columbia, Vancouver, B.C. 1980.

4. M.A. PY and R.R. HAERING. Can J. Phys. **61**, 76 (1983).

5. K. BRANDT and J.A.R. STILES. Proc. 1984 Goddard Space Flight Center Battery Workshop. 1984. p.79.

6. P. MULHERN. Ph.D. thesis. University of British Columbia, Vancouver, B.C. 1986.

7. C.J. JOHNSON and F. LAMAN. Proc. Symp. Lithium Batteries. Vol. **87-1**. The Electrochemical Society, Pennington, NJ. 1986. p.310.

8. R.R. CHIANELLI, E.B. PRESTBRIDGE, T.A. PECORARO and J.P. DENEUFVILLE. Science. **203**, 1105 (1979).

9. G.C. STEVENS and T. EDMONDS. Studies in Surface Science and Catalysis. Vol. **3**, Preparation of Catalysts II. *Edited by* B. Delmon, P. Grange, P. Jacobs and G. Poncelot. Elsevier Scientific Publishing Company. 1979.

10. D.C. JOHNSON, B.G. SILBERGANEL, M. DAAGE and R.R. CHIANELLI. Div. of Petroleum Chemistry, Inc. American Chemical Society, Miami Beach Meeting. March 28-May 3, 1985.

11. M.A. GEE, R.F. FRINDT, P. JOENSEN and S.R. MORRISON. Mat. Res. Bull. **21**, 543 (1986).

12. M.A. SEGURA, *et al*. U.S. Patent No. 339,406. 1976.

13. I.T. ALI and I.D. GAY. J. Phys. Chem. **85**, 1251 (1981).

14. S.H.C. LIANG and I.D. GAY, Langmuir. **1**, 593 (1985).

15. S.H.C. LIANG and I.D. GAY, J. Catal. **101**, 293 (1986).

16. I.D. GAY, J. Catal. **108**, 15 (1987).

17. G. BRAUER(*Editor*). Handbook of Preparative Inorganic Chemistry. Vol. I. Academic Press, Inc., New York, NY. 1963. p.1416.

18. J.J. AUBORN, Y.L. BARBERIO, K.J. HANSON, D.M. SCHLEICH and M.J. MARTIN. J. Electrochem. Soc. **134**, 580 (1987).

19. D.W. MURPHY and P.A. CHRISTIAN. Science. **205**, 651 (1979).

20. I.D. GAY, J. Magn. Reson. **58**, 413 (1984).

21. A. ABRAGAM. The Principles of Nuclear Magnetism. Oxford University Press, London, England. 1962.

22. C.P. SLICHTER. The Principles of Magnetic Resonance. Harper & Row, New York, NY. 1963.

23. A. PINES, M.G. GIBBY and J.S. WAUGH. J. Chem.Phys. **59**, 569 (1973).

24. S.J. OPELLA and M.H. FREY. J. Am. Chem. Soc. **101**, 5854 (1979).

25. T.M. DUNCAN, J.T. YATES, JR. and R.W. VAUGHAN. J. Chem. Phys. **73**, 975 (1980).

26. S.R. HARTMANN and E.L. HAHN. Phys. Rev. **128**, 2042 (1962).

27. E.O. STEJSKAL and J. SCHAEFER. J. Magn. Reson. **18**, 560 (1975).

28. R. FONG, M.C. REID, R.S. McMILLAN and J.R. DAHN. J. Electrochem. Soc. **134**, 516 (1987).

29. B.D. CULLITY. Elements of X-ray Diffraction, Second Edition. Addison-Wesley Publishing Company, Inc. (1978).

30. J.R. DAHN, M.A. PY and R.R. HAERING. Can. J. Phys. **60**, 307 (1982).

31. K.M. COLBOW. M.Sc. thesis. University of British Columbia, Vancouver, B.C. 1988.

32. R. MARSOLAIS. Spectrum Computer Program. University of British Columbia, Physics Department, Vancouver, B.C. 1980.

33. R.W.G. WYCKOFF. Crystal Structures, Vol. **3**, Second Edition. R.E. Krieger Publishing Company, Malabar, Florida. 1982. p.95,100-101.

34. S. BRUNAUER, P.H. EMMETT and E. TELLER. J. Am. Chem. Soc. **60**, 309 (1938).

35. H.L. PICKERING and H.C. ECKSTROM. J. Am. Chem. Soc. **74**, 4775 (1952).

36. D.M. SCHLEICH and M.J. MARTIN. J. Solid State Chem. **64**, 359 (1986).

37. P. JOENSEN, R.F. FRINDT and S.R. MORRISON. Mat. Res. Bull. 21, 457 (1986).

38. R.R. CHIANELLI and M.B. DINES. Inorg. Chem. **17**, 2758 (1978).

39. F.T. EGGERTSEN and R.M. ROBERTS. J. Phys. Chem. **63**, 1981 (1959).

40. S. KOLBOE and C.H. AMBERG. Can. J. Chem. **44**, 2623 (1966).

41. P. RATNASAMY and A.J. LEONARD. J. Catal. **26**, 352 (1972).

42. E. FURIMSKY and C.H. AMBERG. Can. J. Chem. **53**, 3567 (1975).

43. D.G. KALTHOD and S.W. WELLER. J. Catal. **95**, 455 (1985).

44. R.W.G. WYCKOFF. Crystal Structures, Vol. 1, Second Edition. R.E. Krieger Publishing Company, Malabar, Florida. 1982. p.280.

45. K.S. LIANG, R.R. CHIANELLI, F.Z. CHIEN and S.C. MOSS. J. Non-Cryst. Solids. **79**, 251 (1986).

46. L.S. SELWYN, W.R. McKINNON, U. von SACKEN and C.A. JONES. Solid State Ionics. **22**, 337 (1987).

47. A.J. JACOBSON, R.R. CHIANELLI and M.S. WHITTINGHAM. J. Electrochem. Soc. **126**, 2277 (1979).

48. M.B. DINES and R.R. CHIANELLI. U.S. Patent No. 4,299,892. 1981.

49. Sadtler Research Laboratories, Inc. NMR Spectra.

50. J.B. SMOTHERS. Organic Chemistry, A Series of Monographs, Vol. 24, Carbon-13 NMR Spectroscopy, Academic Press, Inc., New York, N.Y. 1972.

51. C.H. KLUTE and W.D. WALTERS. J. Am. Chem. Soc. **68**, 506 (1946).

52. B.K. MIREMADI and S.R. MORRISON. Surface Science. **173**, 605 (1986).